SECURITY CLASSIFICATION OF THIS PAGE (When Data Entered)

REPORT DOCUMENTATION PAGE

READ INSTRUCTIONS BEFORE COMPLETING FORM

1. REPORT NUMBER: SIO REFERENCE 85-33	2. GOVT ACCESSION NO.
3. RECIPIENT'S CATALOG NUMBER	
4. TITLE (and Subtitle): DEEP SEAFLOOR ACOUSTIC BACKSCATTERING MEASUREMENTS USING SEA BEAM	5. TYPE OF REPORT & PERIOD COVERED: Summary
6. PERFORMING ORG. REPORT NUMBER: MPL-U-54/85	
7. AUTHOR(s): Christian de Moustier	8. CONTRACT OR GRANT NUMBER(s): N00014-79-C-0472
9. PERFORMING ORGANIZATION NAME AND ADDRESS: University of California, San Diego, Marine Physical Laboratory, Scripps Institution of Oceanography, San Diego, CA 92152	10. PROGRAM ELEMENT, PROJECT, TASK AREA & WORK UNIT NUMBERS
11. CONTROLLING OFFICE NAME AND ADDRESS: Office of Naval Research, Department of the Navy, 800 North Quincy Street, Arlington Virginia 22217	12. REPORT DATE: December 1985
	13. NUMBER OF PAGES: 142
14. MONITORING AGENCY NAME & ADDRESS (if different from Controlling Office)	15. SECURITY CLASS. (of this report): UNCLASSIFIED
	15a. DECLASSIFICATION/DOWNGRADING SCHEDULE

16. DISTRIBUTION STATEMENT (of this Report)

Document cleared for public release; distribution unlimited.

17. DISTRIBUTION STATEMENT (of the abstract entered in Block 20, if different from Report)

18. SUPPLEMENTARY NOTES

19. KEY WORDS (Continue on reverse side if necessary and identify by block number)

multibeam echo sounders, sea beam, bathymetric surveys, acoustic boundary mapping, acoustic backscatter

20. ABSTRACT (Continue on reverse side if necessary and identify by block number)

Multibeam echo-sounders such as Sea Beam allow investigators to carry out detailed bathymetric surveys of large areas of the seafloor. However, bathymetry only reveals the shape of seafloor features to the resolution of the sounding system, and in order to make geological interpretations one needs to characterize the nature of the seafloor surveyed.

Because bottom roughness and/or variations in bottom substrate cause fluctuations in the backscattered acoustic signal received by an echo-sounder

DD FORM 1 JAN 73 1473 EDITION OF 1 NOV 65 IS OBSOLETE

S/N 0102-LF-014-6601

SECURITY CLASSIFICATION OF THIS PAGE (When Data Entered)

such characteristics can be inferred in part by analyzing the structure and the variations of this signal over several transmission cycles.

The approach taken has been to record digitally the detected echo envelopes of Sea Beam's 16 narrow beams over a variety of seafloor environments, and process these data to determine whether the acoustics held enough information to differentiate between bottom types.

Significant results derived from these acoustic data concern (1) the Sea Beam system's performance (2) its potential for mapping acoustic boundaries and (3) the display of the echoes received in a side looking sonar-like picture.

The system was found to work well under most circumstances as a contour mapping tool, but it occasionally suffers echo processing malfunctions producing artifacts in the contoured bathymetric output which can induce the unwary investigator to make geological interpretation errors [de Moustier and Kleinroce (1985) J.G.R. in press].

Acoustic boundary mapping has been successfully carried out over a manganese nodule mining site in the Northeastern Tropical Pacific where a first order assessment of nodule coverage validated with bottom photographs proved the techniques feasible [de Moustier (1985) Geophysics, V. 50, p. 989-1001]. Comparison of results from environments as diverse as a lava sheet flow on the crest of the East Pacific Rise, a sedimentary basin offshore Southern California, and a manganese nodule field show marked differences in the overall backscattered acoustic energy level as well as in the inferred roughness character between these areas, [de Moustier J.A.S.A., submitted]. Although these simple characteristics are insufficient to determine the nature of the seafloor surveyed, they represent additional clues to help understand the geological processes under investigation.

Further insight into these processes is afforded by the qualitative measure of acoustic backscatter inherent to a gray scale side looking sonar display. Such displays have been created with Sea Beam acoustic data. They contain a wealth of information not available in the bathymetric contours and are expected to become a very valuable addition to the Sea Beam system.

This research has been sponsored by the Office of Naval Research Contract No. N00014-79-C-0472.

DEEP SEAFLOOR ACOUSTIC BACKSCATTERING MEASUREMENTS USING SEA BEAM

Christian de Moustier

Sponsored by the
Office of Naval Research
Contract N00014-79-C-0472

SIO REFERENCE 85-33

December 1985

MPL-U-54/85

MARINE PHYSICAL LABORATORY
of the Scripps Institution of Oceanography
San Diego, California 92152

UNIVERSITY OF CALIFORNIA, SAN DIEGO
MARINE PHYSICAL LABORATORY OF THE
SCRIPPS INSTITUTION OF OCEANOGRAPHY
SAN DIEGO, CA 92152

DEEP SEAFLOOR ACOUSTIC BACKSCATTERING MEASUREMENTS USING SEA BEAM

Christian de Moustier

Sponsored by the
Office of Naval Research
Contract N00014-79-C-0472

SIO REFERENCE 85-33

December 1985

K. M. Watson, Director
Marine Physical Laboratory

MPL-U-54/85

Table of Contents

Page

List of Figures and Tables

Figure Page

Chapter IV

Appendix

Table

ACKNOWLEGMENTS

I wish to thank the members of my committee for their time spent reviewing the work presented in this dissertation, and for their constructive criticisms. I am particularly indebted to Fred Spiess for accepting to supervise my work for the past two and a half years, and for helping me survive successfully three funding reviews from the Office of Naval Research. I also thank Bob Tyce for involving me in the Sea Beam acoustic backscattering experiment that he initiated at the Marine Physical Laboratory, and for letting me continue the work when he took a position with the University of Rhode Island Graduate School of Oceanography in 1983.

Much of the development for the Sea Beam acoustic data acquisition system is due to Vince Pavlicek who deserves a special mention for his generosity with his time and his electronics expertise. His encouragement at critical moments has been invaluable.

I am deeply indebted to Jack Capell of General Instrument Corporation for his infinite patience in answering my questions about the Sea Beam system. His willingness to disclose some of the design parameters of the system has been a key element in understanding and interpreting the acoustic data that have been recorded from Sea Beam.

The first chapter of this dissertation would probably never have been written were it not for Marty Kleinrock's enthusiasm and keen sense of observation. I thank him for the long hours spent reviewing and correcting the corresponding paper.

Most of the work presented here relies on data collected at sea, and it would not have been possible without the cooperation of the officers, crew and scientific parties of the Research Vessels *Thomas Washington* and *Melville* during eleven cruises. This includes the engineers from the Deep Tow group: Tony Boegeman, Bob Elder, John Jain and Tyrone Clary; and members of the Shipboard Support group:

Lynn Abbott, Tom Hylas, Pat Downes, Ron Moe, Mike Moore and Gene Pillard who have been extremely helpful both at sea and ashore.

I am grateful to Carl Lowenstein and Bob Lawhead for numerous helpful tips in the realm of DEC computers, to Bill Hodgkiss for his advice on signal processing matters, and to Peter Lonsdale for his generous help on survey work and map making. I also wish to express my sincere gratitude to Eleanor Ford for bearing with too many 'nasty equations' and countless revisions of the papers which constitute this dissertation; and to Jo Griffith for expertly drafting all the figures (regardless of Padres results).

This research has been funded by the Office of Naval Research, (Contract No. N00014-79-C-0472), and I wish to thank Gerry Morris for his continued support. Also, a very important element in my stay at Scripps has been the availability of a grant from the Scripps Industrial Associates; I could not have done without it.

Among my friends and colleagues who have helped me on countless occasions I want to give special credit to Dimitri Alexandrou, Rick Brienzo, Kathy Crane, John Hildebrand, Al Plueddemann and Allan Sauter. I also thank Robin Williams and Barbara Sotirin for supplying me with many very helpful references.

Finally, I would like to thank my parents as well as Louis de Rochebouët , James Stewart and Dave Kahl, all of whom gave me a chance to try.

VITA

July 4, 1956 — Born — Neuilly-sur-Seine, France

1979 —	Diplome d'Ingénieur, Ecole Supérieure d'Ingénieurs de Marseille (France)
1978-1979 —	6 months of Research and Development, Sperry Marine Systems, Great Neck, New York and Charlottesville, Virginia
1979-1980 —	French Navy
1980 —	Certificat d'Etudes Approfondies, C.N.R.S. Marseille
1980-1985 —	Research Assistant, Marine Physical Laboratory, University of California, San Diego
1981 —	M.S., University of California, San Diego
1985 —	Doctor of Philosophy University of California, San Diego

PUBLICATIONS

C. de Moustier, "Inference of manganese nodule coverage from Sea Beam acoustic backscattering data." Geophysics, Vol. 50, pp. 989-1001, 1985.

C. de Moustier, "Beyond bathymetry: mapping acoustic backscattering from the deep seafloor with Sea Beam", J. Acoust. Soc. Am. (submitted).

C. de Moustier and M. C. Kleinrock, "Bathymetric artifacts in Sea Beam data: how to recognize them, what causes them", J. Geophys. Res. (in press).

C. de Moustier, "Approaches to acoustic backscattering measurements from the deep seafloor", Trans. Am. Soc. Mech. Eng. Ocean engineering Symposium (submitted).

C. de Moustier, "A Sea Beam acoustic data acquisition system", MPL TM-379 Marine Physical Laboratory, Scripps Institution of Oceanography, San Diego, Ca. .

ABSTRACTS

M. C. Kleinrock, R. N. Hey and C. de Moustier, "The 'Omega' deception in Sea Beam data", Trans. Am. Geophys. Union, 65, 1104, 1984.

C. de Moustier, "Beyond bathymetry: Sea Beam can also contour variations in sea floor reflectivity", Trans. Am. Geophys. Union, 64, No 52, 1031, 1983.

C. de Moustier, "Seafloor acoustic backscatter measurements using Sea Beam: II", J. Acoust. Soc. Am., Vol 74, S44, 1983.

C. de Moustier and R. C. Tyce, "Sea floor acoustic backscatter measurements using Sea Beam", Trans. Am. Geophys. Union, 63, No 45, 1107, 1982.

FIELDS OF STUDY

Major Field: Oceanography

Studies in Underwater Acoustics.
Professors Victor C. Anderson and Fred N. Spiess

Studies in Signal Processing and Data Analysis.
Professors William S. Hodgkiss and Richard A. Haubrich

ABSTRACT OF THE DISSERTATION

Deep seafloor acoustic backscattering

measurements using Sea Beam

by

Christian de Moustier

Doctor of Philosophy in Oceanography

University of California, San Diego, 1985

Professor Fred N. Spiess, Co-Chairperson

Associate Professor Robert C. Tyce, Co-Chairperson

Multibeam echo-sounders such as Sea Beam allow investigators to carry out detailed bathymetric surveys of large areas of the seafloor. However, bathymetry only reveals the shape of seafloor features to the resolution of the sounding system, and in order to make geological interpretations one needs to characterize the nature of the seafloor surveyed.

Because bottom roughness and/or variations in bottom substrate cause fluctuations in the backscattered acoustic signal received by an echo-sounder, such characteristics can be inferred in part by analyzing the structure and the variations of this signal over several transmission cycles.

The approach taken has been to record digitally the detected echo envelopes of Sea Beam's 16 narrow beams over a variety of seafloor environments, and process these data to determine whether the acoustics held enough information to differentiate between bottom types.

Significant results derived from these acoustic data concern (1) the Sea Beam system's performance (2) its potential for mapping acoustic boundaries and (3) the

INTRODUCTION

This dissertation presents the results of an experiment to measure seafloor acoustic backscatter with the multibeam echo-sounder Sea Beam. With this system, sound transmission and reception are achieved by two adjacent acoustic arrays so that the echo signals received correspond to the portion of the acoustic energy which is scattered back towards the sound source in a direction opposite that of the incident sound. Interest in such measurements stems from the fact that changes in the composition or the roughness structure of the seafloor cause variations in the acoustic signals scattered by the seafloor.

Sea Beam processes the bottom echo signals it receives to determine the bathymetric data necessary for contour mapping and then discards these signals. A parallel acoustic data acquisition system is therefore required to preserve them for further processing and analysis. The approach taken here consists in recording digitally the bottom echo signals received by Sea Beam over a variety of seafloor environments. As a first step in the processing and analysis of these data, the recorded acoustic signals are used to assess the performance of the Sea Beam system. The next step concerns use of the amplitude variations in the recorded signals to produce sidescan images of the seafloor. Further analysis of the structure and variations of these echo signals over several transmission cycles is used to relate information contained in the acoustics to seafloor properties. In the scope of this dissertation, this analysis is limited to areas of the seafloor which are nearly flat. However, acoustics alone do not give a unique answer about the nature of the seafloor, and independent measurements (e.g. bottom photographs, core samples, etc.) provide the necessary ground truth.

Following the analysis sequence outlined above, this dissertation is divided into four chapters and an appendix. Each chapter is self-contained and corresponds to

a paper that has been published by, or submitted to a refereed scientific journal. As a result, some redundancy exits between chapters whenever the Sea Beam system is described.

The first chapter reviews the operational characteristics of the Sea Beam system and uses the recorded acoustic data to take an in-depth look at the system's performance as a mapping tool. Although the system works well under most circumstances, several bathymetric artifacts have been observed in the contoured outputs. These artifacts are analyzed and their causes are identified by examining the character of the bottom echoes received and processed by the system. This analysis leads to recommendations for improving bathymetric data quality. This chapter represents a paper co-authored by Martin C. Kleinrock who contributed examples of bathymetric artifacts found in the data contoured by Sea Beam, and who assessed their geological implications. This paper has been accepted by the Journal of Geophysical Research.

In the second chapter, the variations in amplitude of the echo signals received by Sea Beam are used to produce a sidescan image of the seafloor surveyed. This is a new application of the Sea Beam system which is expected to enhance its usefulness during geological investigations of the seafloor, by complementing the standard bathymetric contouring with a qualitative measure of bottom acoustic backscatter which is related to the texture of the seafloor. This chapter corresponds to a short invited paper submitted to the American Society of Mechanical Engineers for its symposium on Ocean Engineering. As such, it also reviews the approaches currently taken by the oceanographic community to measure acoustic backscattering from the deep seafloor.

The third chapter is a first attempt at relating the character of the acoustic backscatter to the geological processes that cause it. The variations of the peak

amplitude of Sea Beam's near-specular return along the ship's track are compared with the density of coverage of manganese nodules at a mining site in the Northeastern Tropical Pacific. A 98% qualitative agreement is found between manganese nodule coverage inferences obtained with Sea Beam's acoustics and with bottom photographs taken by the Deep Tow instrument package in the same area. The paper corresponding to this chapter is published in Geophysics [V.50, 989-1001, 1985].

The fourth chapter expands the analysis of Sea Beam's acoustics to nonspecular beams. Measurements from three geologically different areas are compared. Acoustic backscattering boundaries are mapped both along and across the ship's track by following trend changes in the total energy of the acoustic returns over many transmission cycles. A partial angular-dependence function of backscattering shows marked differences in the overall acoustic energy level recorded at each site. Application of Rician statistics to the distribution of peak amplitude in the near-specular direction gives clues to the roughness character of each area, and provides a means to differentiate them. This chapter represents a paper which has been submitted for publication to the Journal of the Acoustical Society of America.

Because of editorial constraints imposed by publishers, the method used to record Sea Beam's acoustic data is mentioned only briefly in these chapters. For this reason, a brief technical description of the Sea Beam system and a detailed description of the method used to record the acoustic signals it receives are included in the appendix.

Possible extensions of this work include application of the Sea Beam results to other multibeam echo-sounders and refinement of the acoustic data processing techniques to account for bottom slopes effects in areas of large relief.

Chapter I

BATHYMETRIC ARTIFACTS IN SEA BEAM DATA: HOW TO RECOGNIZE THEM, WHAT CAUSES THEM.

I.1. ABSTRACT

Sea Beam multibeam bathymetric data have greatly advanced understanding of the deep seafloor. However, several types of bathymetric artifacts have been identified in Sea Beam's contoured output. Surveys with many overlapping swaths and digital recording on magnetic tape of Sea Beam's sixteen acoustic returns made it possible to evaluate actual system performance. The artifacts are not due to the contouring algorithm used. Rather, they result from errors in echo detection and processing. These errors are due to internal factors such as sidelobe interference, bottom-tracking gate malfunctions, or external interference from other sound sources (e.g. 3.5 kHz echo-sounders or seismic sound sources). Although many artifacts are obviously spurious and would be disregarded, some (particularly the 'omega' effects described in this paper) are more subtle and could mislead the unwary observer. Artifacts observed could be mistaken for volcanic constructs, abyssal hill trends, hydrothermal mounds, slump blocks or channels, and could seriously affect volcanic, tectonic or sedimentological interpretations. Misinterpretation of these artifacts may result in positioning errors when seafloor bathymetry is used to navigate the ship. Considering these possible geological misinterpretations, a clear understanding of the Sea Beam system's capabilities and limitations is deemed essential.

I.2. INTRODUCTION

The Sea Beam bathymetric survey system is a multibeam echo-sounder developed by the General Instrument Corporation to produce near-real-time high resolution contoured swath charts of the seafloor down to maximum ocean depth (11 km). Since 1977 when the first system became operational aboard the French R/V *Jean Charcot*, nine other systems have been installed aboard research vessels from the United States, Germany, Japan and Australia.

Sea Beam systems have proven extremely useful in the study of the geomorphology of the ocean floor, and have made possible striking discoveries of features which would not have been detected with conventional single point depth sounders [e.g. Macdonald and Fox, 1983; Lonsdale, 1983]. However, after three years of experience with the system installed aboard the R/V *Thomas Washington* of the Scripps Institution of Oceanography (SIO), we have discovered a number of artifacts in Sea Beam's contoured output. Their artificial nature has been demonstrated by comparing overlapping Sea Beam swaths and by analyzing digitized raw acoustic data. During four cruises aboard the R/V *Thomas Washington* we used a data acquisition system developed by SIO's Marine Physical Laboratory (MPL) to record digitally the acoustic returns from Sea Beams' sixteen preformed beams on magnetic tape. This data set has enabled us to determine the causes of these artifacts. They do not stem from the vagaries of the contouring algorithm used, rather they are the result of errors in echo detection and processing. In our experience, such detection errors are mostly related to some characteristics of the ocean bottom (e.g. type of substrate or sudden change in slope) or to interference from other sound sources running in parallel with Sea Beam (mostly subbottom profilers: 3.5 kHz echo-sounder and seismic sources).

This paper describes several artifacts discovered in Sea Beam data and

discusses the associated possible geological misinterpretations. We suggest a number of solutions to improve data quality. We also consider the existence of related artifacts in similar multibeam echo-sounders (e.g. the Sonar Array Sounding System (SASS) [Glenn, 1970]).

I.3. BACKGROUND: THE SEA BEAM SYSTEM

Before going into a detailed explanation of the problems found in the SIO system, we briefly review Sea Beam's general framework for the reader unfamiliar with the system. Further discussion of the system are found in Renard and Allenou [1979] and in Farr [1980]. Because a clear understanding of Sea Beam's acoustic geometry and echo processing methods is a prerequisite to analyze its bathymetric output, we have included in the appendices relevant technical information not available in the literature.

As illustrated by the simplified block diagram in Figure 1.1, the Sea Beam system uses a multibeam narrow beam echo-sounder and an echo processor (EP) to generate in near-real time, contour maps of the ocean floor. A 20-element projector array mounted along the ship's keel sends out a 7 millisecond pulse of 12.158 kHz at intervals that are integral multiples of one second. The transmission period is usually determined by an analog graphic recorder. The receiving unit lies athwartships and consists of 40 line hydrophone arrays whose long axes are oriented fore-aft. The resulting transmit/receive geometry is illustrated in Figure 1.2 In this figure, vertical cross sections of theoretical beam patterns are shown for both the projector (Fig. 1.2a) and the receiver (Fig. 1.2b) arrays. The transmit beam pattern spans 54 degrees athwartships by 2 2/3 degrees in the fore-aft direction. It is pitch stabilized within a range of $\pm$ 10 degrees of pitch. There is no pitch compensation for the receive beam pattern, instead it spans 20 degrees in the fore-aft direction to accommodate pitch

discusses the associated possible geological misinterpretations. We suggest a number of solutions to improve data quality. We also consider the existence of related artifacts in similar multibeam echo-sounders (e.g. the Sonar Array Sounding System (SASS) [Glenn, 1970]).

I.3. BACKGROUND: THE SEA BEAM SYSTEM

Before going into a detailed explanation of the problems found in the SIO system, we briefly review Sea Beam's general framework for the reader unfamiliar with the system. Further discussion of the system are found in Renard and Allenou [1979] and in Farr [1980]. Because a clear understanding of Sea Beam's acoustic geometry and echo processing methods is a prerequisite to analyze its bathymetric output, we have included in the appendices relevant technical information not available in the literature.

As illustrated by the simplified block diagram in Figure 1.1, the Sea Beam system uses a multibeam narrow beam echo-sounder and an echo processor (EP) to generate in near-real time, contour maps of the ocean floor. A 20-element projector array mounted along the ship's keel sends out a 7 millisecond pulse of 12.158 kHz at intervals that are integral multiples of one second. The transmission period is usually determined by an analog graphic recorder. The receiving unit lies athwartships and consists of 40 line hydrophone arrays whose long axes are oriented fore-aft. The resulting transmit/receive geometry is illustrated in Figure 1.2 In this figure, vertical cross sections of theoretical beam patterns are shown for both the projector (Fig. 1.2a) and the receiver (Fig. 1.2b) arrays. The transmit beam pattern spans 54 degrees athwartships by 2 2/3 degrees in the fore-aft direction. It is pitch stabilized within a range of $\pm$ 10 degrees of pitch. There is no pitch compensation for the receive beam pattern, instead it spans 20 degrees in the fore-aft direction to accommodate pitch

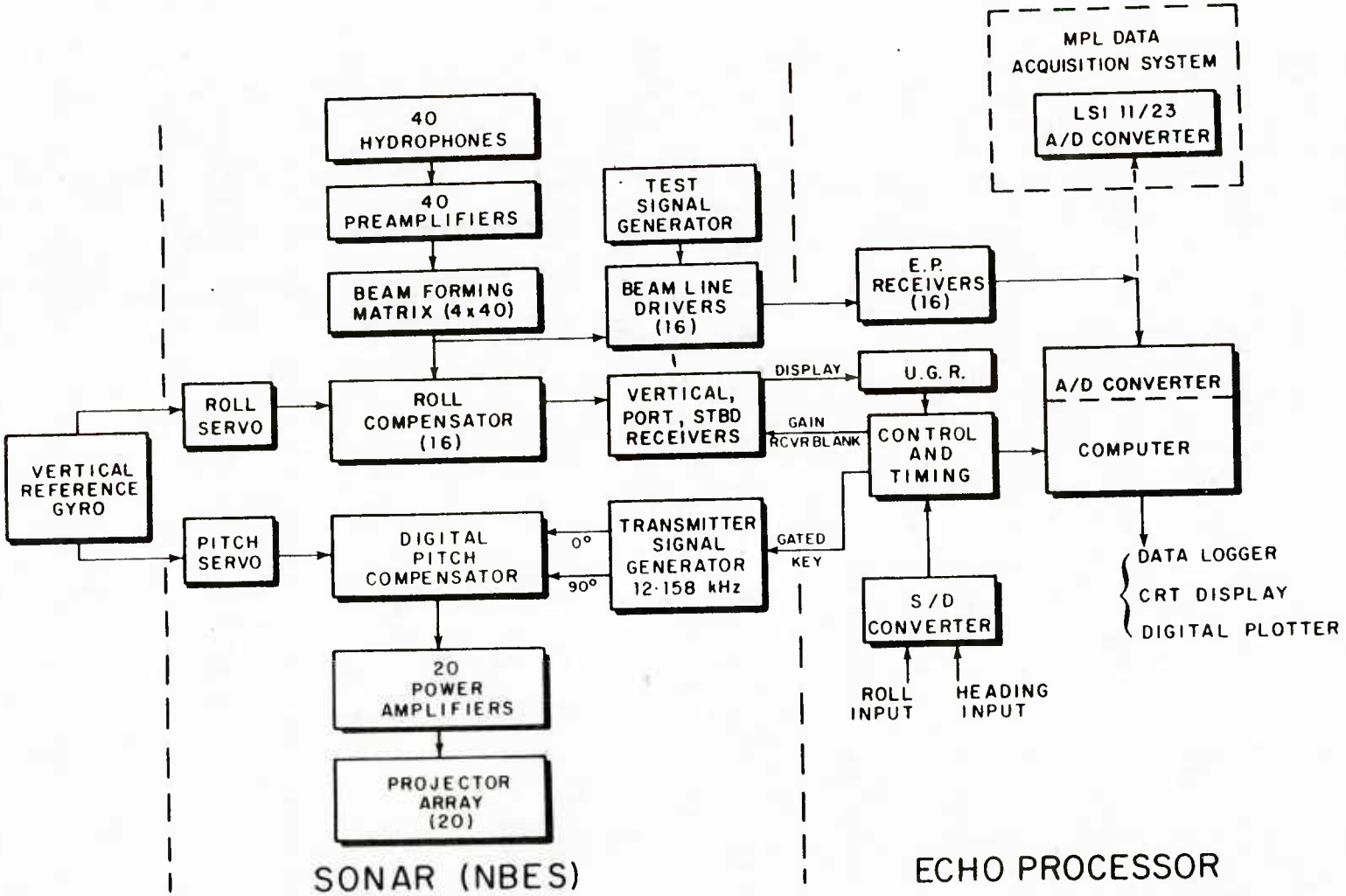

Figure 1.1 *Block diagram of the Sea Beam system showing the Narrow Beam Echo Sounder and the Echo Processor.* The position of the MPL data acquisition system is shown for reference.

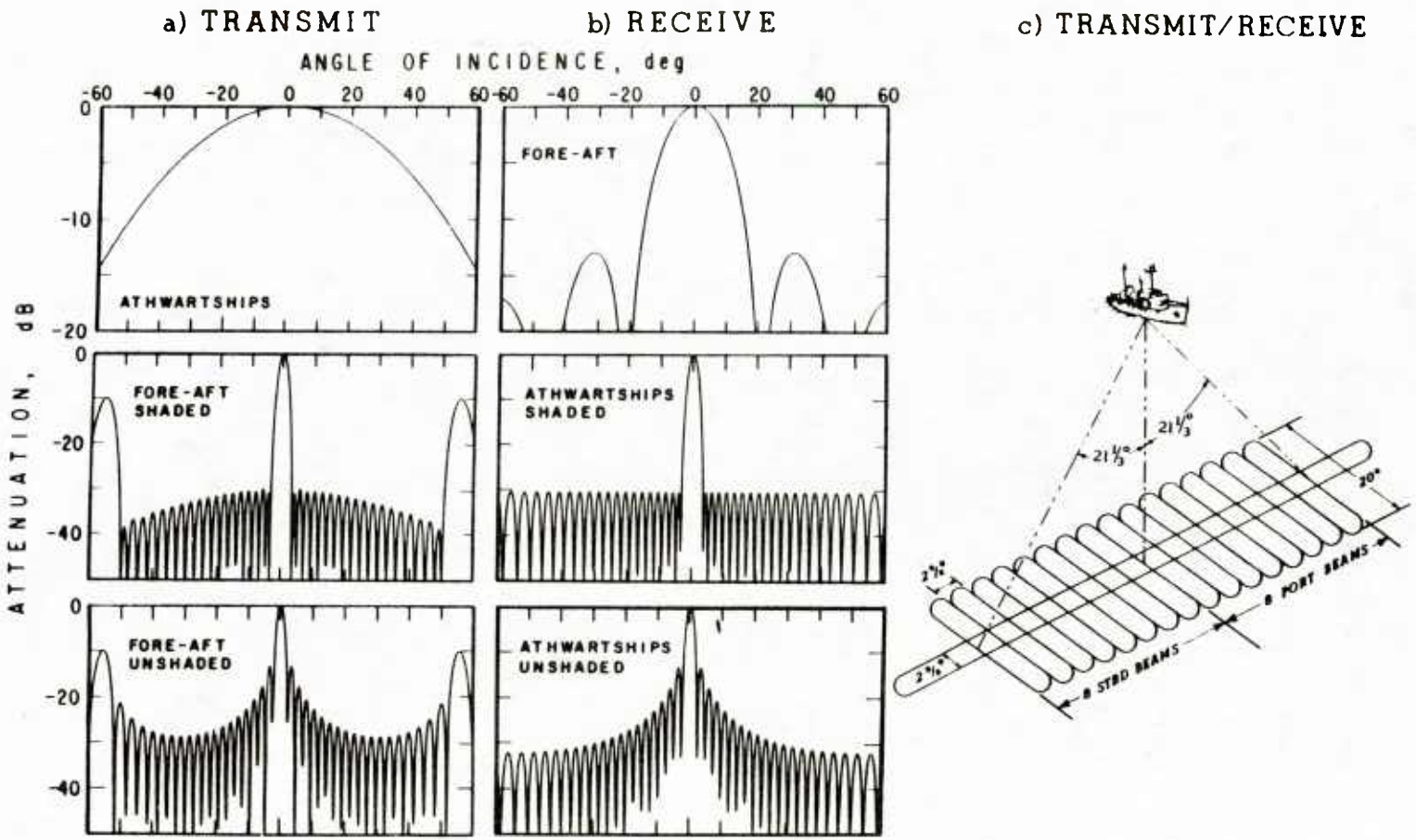

Figure 1.2 *Sea beam transmit/receive geometry.* Computed beam pattern cross-sections in the athwartships vertical plane centered on the array and in the vertical plane passing through the ship's fore-aft axis are shown for (a) the projector array, (b) the receiver array. The effect of Dolph-Chebyshev amplitude shading is also illustrated. (c) is a summary cartoon showing the angular relationship between the mainlobe of the transmitted beam pattern and those of the sixteen preformed beams.

angles of ± 10 degrees. The athwartships beam width is 2 2/3 degrees. Sea Beam receives with sixteen fixed preformed beams obtained by electronically steering this 20 x 2 2/3 degrees beam at athwartships intervals of 2 2/3 degrees between ± 20 degrees of incidence. In this configuration there is no beam along the ship's vertical axis, rather two of the beams point at 1 1/3 degrees on either side of this axis.

The acoustic energy received at the ship comes from the intersection of the transmit and receive beam patterns. This appears in Figure 1.2c as sixteen squares 2 2/3 degrees on a side. This figure is only meant to illustrate the angular relationship between the mainlobe of the transmitted beam pattern and the mainlobes of the sixteen preformed beams. Actual footprints are not rectangles or squares; they are ellipses whose areas increase away from vertical incidence. Since depths are ideally determined at the center of each of the preformed beams, the maximum swath width corresponds to 73% of the water depth.

The beam forming operation described above generates sixteen acoustic signals. These are sent to the EP receivers where they are filtered, rectified, amplified and transferred to the Sea Beam computer (Fig. 1.1). Figure 1.3 shows a typical output of the sixteen EP receivers. Each waveform corresponds to a preformed beam and is accordingly numbered from the center out (1-8) on port and starboard. In this figure the ridge of synchronous returns (see arrow labelled "sidelobe"), corresponds to energy from the near-specular direction (tallest return) entering the sidelobes of the other beams. The sixteen bottom return signals form a parabola, indicating a flat portion of seafloor. These data have been digitized and recorded on magnetic tape with a separate data acquisition system (Fig. 1.1) built around an LSI 11/23 minicomputer, in an experiment conducted by MPL to measure acoustic backscatter from the deep seafloor. They have proven invaluable to evaluate the performance of the EP because Sea Beam only retains depths and cross-track horizontal distances.

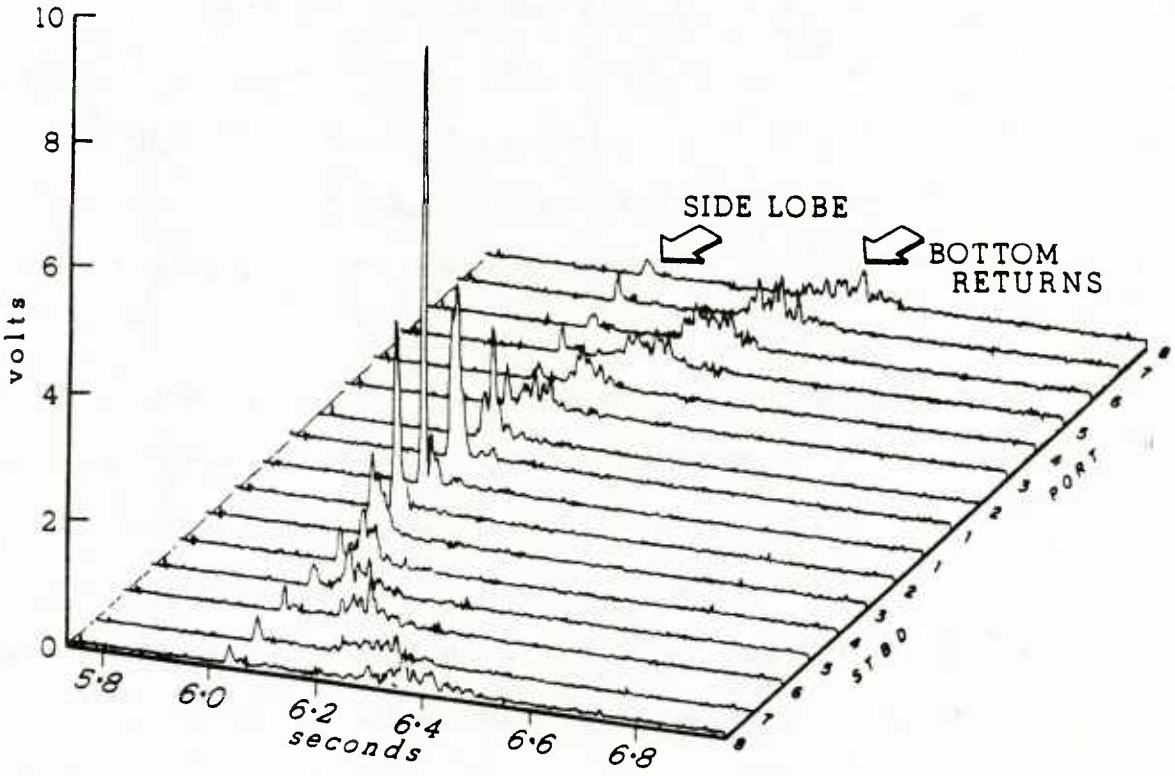

Figure 1.3 *Acoustic signal envelopes of the sixteen preformed beams at the output of the Sea Beam Echo Processor receivers.* The time-axis represents seconds after transmission. The vertical-axis in volts represents the voltage equivalent of the sound pressure level at the receiver array, corrected for acoustic transmission losses in the water column by a time-varied gain (TVG). No roll compensation, recording gain or receiver gain corrections have been applied to the data at this stage. Such data are recorded digitally on magnetic tape every transmission cycle, along with time, TVG and ship's roll.

In the Sea Beam computer, sixteen such waveforms are simultaneously digitized at a frequency of 300 Hz per waveform. This corresponds to one digitization cycle every 3.33 ms or 2.5 m of slant range assuming a sound velocity of 1500 m/s. Consequently, slant range and therefore depth determination resolution is limited to 2.5 m. While it digitizes the acoustic data, the computer also performs several echo processing tasks. For each digitization cycle these tasks are: receiver gain correction, refraction correction, roll compensation, detection threshold level computation and echo detection. Automatic bottom-tracking gates (one for each beam) determine a time window during which a return is expected on any one beam based on previous sounding history. A return is detected if it falls within the gates and lies above the threshold.

In general, the threshold level is computed to ride above the noise, above the sidelobe response to a strong specular return and above potential noise bursts interfering with bottom echo detection. A manual threshold can also be entered by the Sea Beam operator. As we shall see in the following sections, thresholding and gating are two critical operations in the echo processing. A more detailed description of Sea Beam's echo processing may be found in Appendix B.

For each roll compensated beam having sufficient signal to noise ratio, a slant range R is calculated by computing the center of mass of all the detected signal samples for that beam, and by multiplying the corresponding arrival time by 750 m/s. Knowing the slant range R and the stabilized beam angle Ψ, a simple calculation yields the depth Z and the cross-track horizontal distance Y:

$$Z = R \cos \Psi \text{ and } Y = \frac{C_a}{C_n} R \sin \Psi,$$

where C_a is the mean sound velocity obtained by averaging the values of the sound velocity profile from the surface to the average bottom depth (in uncorrected meters) and C_n is the nominal sound velocity in water (1500 m/s). The depth Z is given in

uncorrected meters referenced to a sound velocity of 1500 m/s. The cross-track horizontal distance Y is a true distance because it is corrected for both refraction and travel time.

Finally, the (Z,Y) coordinates for each validated beam are output as a cross-track bottom profile on the EP cathode ray tube (CRT) display. The depths are also used to update the bottom-tracking gates on each beam for the next transmission cycle.

The depths and cross-track horizontal distances for each transmission cycle are logged on a magnetic storage medium (disk or tape) along with time and ship's heading, as well as output in near-real time ($\sim$ 1 minute delay) on paper as a contour chart by an 11" digital swath plotter. In the following, we will refer to the (Z,Y) data as the raw Sea Beam data.

The Sea Beam echo processing sequence outlined here will vary depending on the EP mode chosen by the operator. Three modes are available. Mode 1 is essentially a start-up mode during which no data logging or contour plotting are performed. The EP displays the vertical beam depth and the CRT shows unprocessed echoes on the sixteen preformed beams. The detection threshold used in mode 1 is the highest of the noise threshold, the sidelobe threshold or the threshold entered by the operator. Mode 2 is a semi-automatic EP operation with data logging and contour plotting. The CRT displays processed data in the form of a cross-track bottom depth profile, but the operator controls the tracking gates' width and center. Mode 3 is a completely automatic version of mode 2. It is the mode in which the EP usually operates during bathymetric survey work. A very important and poorly documented difference exists between the detection threshold level determination of mode 1 and that of modes 2 and 3. In modes 2 and 3, a non-zero threshold level input by the operator supercedes any other threshold computation. It is therefore imperative that

the manual threshold be set to zero when in mode 2 or 3. Failure to do so results in the EP tracking the sidelobe response any time a specular return is present on one of the sixteen preformed beams, or if the manual threshold is set high enough, in loss of data.

On most ships equipped with Sea Beam the bathymetry data are merged with ship navigation (transit satellite navigation and dead reckoning, or NAVSTAR Global Positioning System navigation when available) by another computer aboard the ship and recontoured along the ship's track on a 30" digital plotter with a delay time of about two minutes. This gives surveyor the ability to effectively control ship navigation and track spacing by looking at the contours plotted. A second stage of data post-processing, done on ship or ashore, consists of adjusting the navigation to fit corresponding contour lines on adjacent tracks, and of regridding the entire data set to produce a map. When navigation comes from the Global Positioning System there is virtually no need for adjustments. These operations usually smooth the raw Sea Beam soundings by averaging along track over a certain number of transmission cycles (often 5) to produce more even grid spacing along versus across the ship's track, thus removing most of the jitter apparent on near-real time swath plots. However when system errors cause bad soundings, the resulting fictitious bathymetry will often not average out as we shall show in the following sections. Therefore in order to assess the validity of suspicious Sea Beam bathymetry, an investigator needs to refer to the raw data and use any corroborating information available. When only the raw data are available, as is often the case, such assessment requires a clear understanding of the processing performed by the Sea Beam computer on the digitized acoustic signals.

I.4. SEA BEAM BATHYMETRIC ARTIFACTS: Examples, Explanations and Geological implications

Sea Beam has been used extensively in the past several years to study the morphology, tectonics, volcanology and sedimentology of the seafloor. So many Sea Beam surveys have been run that a complete list is too large for inclusion here, therefore we only reference some of the more recent works. Bathymetric charts produced from Sea Beam data have been used as base maps for more detailed studies using deeply towed instrument packages such as MPL's *Deep-Tow* [Spiess and Lonsdale, 1982; Spiess et al., 1984; Hey et al., 1985a] and manned submersibles such as Woods Hole Oceanographic Institute's (WHOI's)*DSRV Alvin* and *DSRV Cyana* of the Institut Français de Recherche pour l'Exploitation de la Mer (*IFREMER*)* [e.g. Ballard and Francheteau, 1983; Francheteau and Ballard, 1983]. Many surveys covering fairly large areas (hundreds of square km) with nearly total coverage have lead to valuable insights into the processes at spreading centers [e.g. Hey et al., 1985a; Crane et al., 1985; Macdonald et al., 1984; Mammerickx, 1984; Lonsdale, 1983], transform faults [e.g. Gallo et al., 1984; Detrick et al., 1984] trenches [e.g. Shipley and Moore, 1985; Lewis et al., 1984], microplates [e.g. Hey et al 1985b, Naar and Hey, 1985], seamounts [e.g. Fornari et al., 1984], and submarine canyon systems [e.g. Lewis et al., 1984]. Sea Beam's regional depiction of the seafloor in these areas has been extremely useful.

In most cases, the finer scale Sea Beam bathymetry is dependable and is reproducible on overlapping swaths. However, given the existence of the bathymetric artifacts discussed in this paper, investigators should be cautious when studying bathymetric details on the scale of hundreds to thousands of meters. This is particularly important for surveys of large areas where bathymetric and structural

*formerly Centre National pour l'Exploitation des Océans (*CNEXO*)

data are interpolated between widely separated Sea Beam swaths. Misinterpreting any of these artifacts as true bathymetric features could also result in positioning errors when the vessel is navigated by comparison of real-time bathymetry with compiled charts.

In the following we discuss three types of bathymetric artifacts resulting from echo processing errors. These errors are due to internal factors such as sidelobe interference or malfunction of the bottom-tracking gates or to external interference from other sound sources. In each case we present evidence of artifacts through Sea Beam data samples, explain their cause, and indicate their geological implications.

I.4.1 Sidelobe interference

Renard and Allenou [1979] recognized sidelobe interference as a potential problem in Sea Beam (e.g. Fig. 21 in their paper). The interference is characterized by small apparent slope fluctuations on seafloor dipping perpendicular to the ship's track and it typically affects only a few beams. A more serious problem occurs when the seafloor surveyed is relatively flat and Sea Beam renders it as a trough (the 'tunnel' effect [Smith, 1983]). This is seen as a concave-up arc on the cross-track CRT bottom profile in Figure 1.4. To understand this artifact, consider the Sea Beam acoustic data shown in Figure 1.5 which is identical in format to Figure 1.3. Note that the sidelobe level is much higher in this figure than in Figure 1.3. If the EP is in mode 3 and a non-zero manual threshold level has been entered by the Sea Beam operator, the system does not calculate a noise or a sidelobe threshold. It therefore tracks the sidelobe response when present and when above the manual threshold level. Arrival times are then synchronous on all beams as if coming from a concave-up horizontal half cylinder. Figure 1.6 shows an example of the resulting bathymetry.

The apparent relief of the 'tunnel' walls in this example ranges from 40 m to 100 m, although theoretically it may be as much as 6% of the water depth.

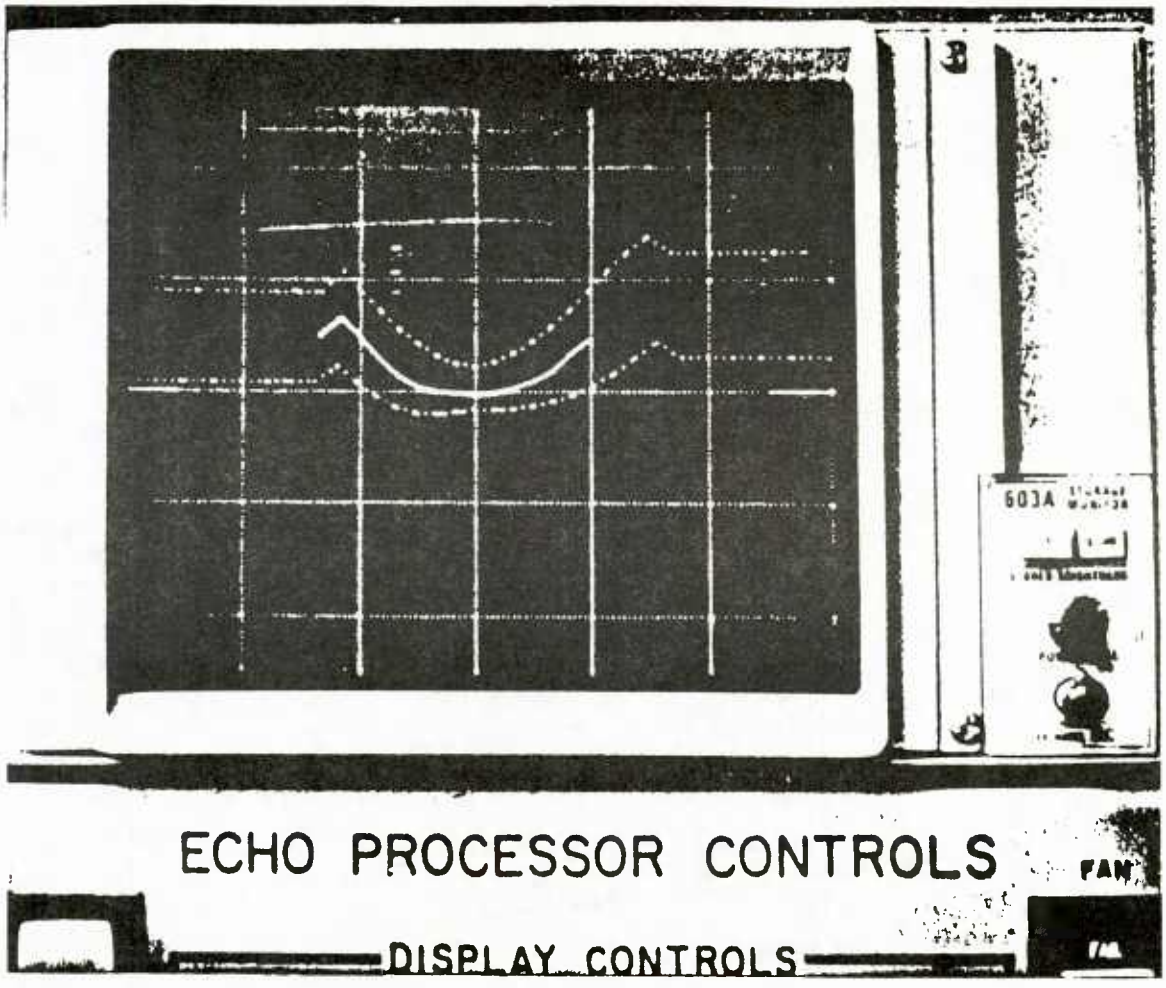

Figure 1.4 *Echo Processor CRT display showing a cross-track bottom profile (solid trace) characteristic of a 'tunnel' effect.* The dashed traces represent the upper and lower positions of the automatic bottom-tracking gates. The vertical scale is 200 m per division. The horizontal scale is compressed to accommodate a reception beam width spanning 80° (40° actual beam width with ± 20° for roll).

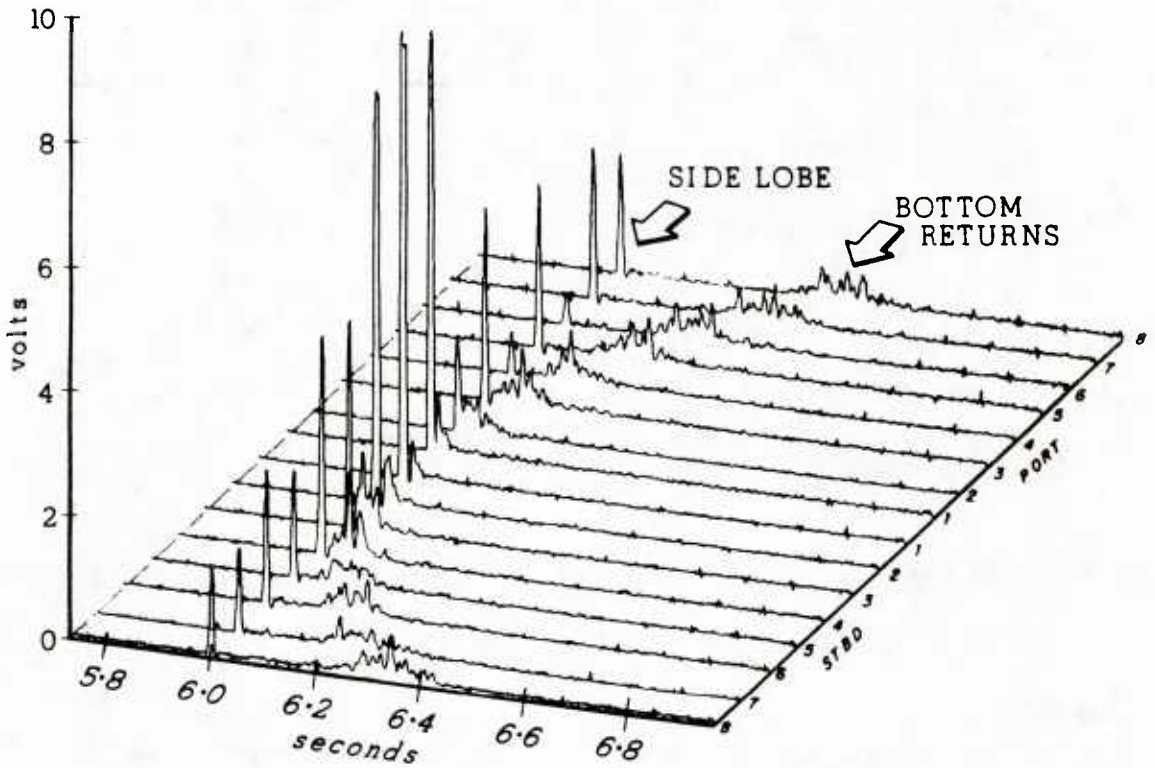

Figure 1.5 *Acoustic signal envelopes of the sixteen preformed beams at the output of the Sea Beam EP receivers.* The format is identical to that of Figure 1.3. The ridge of synchronous returns due to sidelobe response is much more pronounced in this figure than in Figure 1.3 because it is due to a stronger near-specular return (starboard beam #1, which is clipped in this figure)

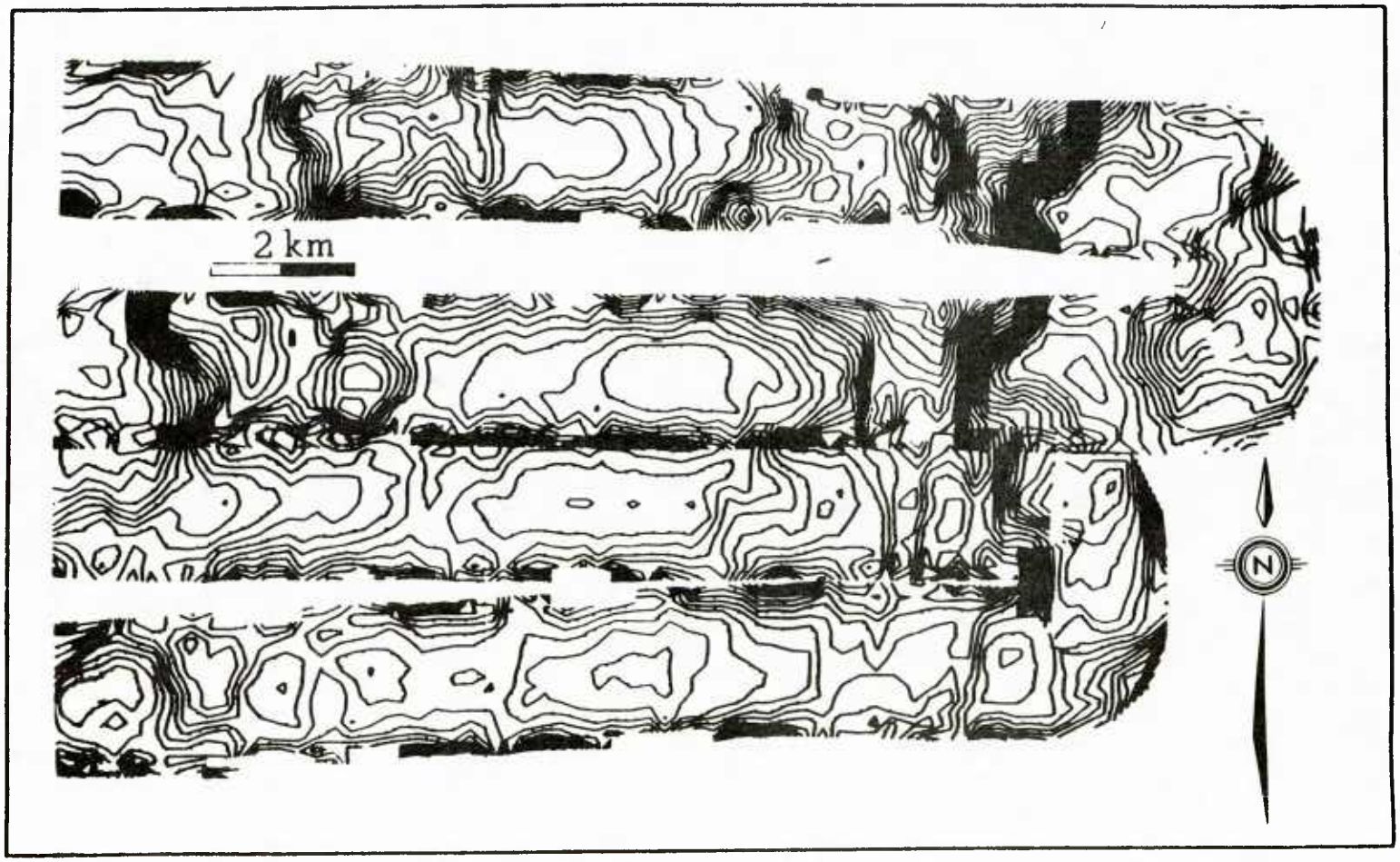

Figure 1.6 *The 'tunnel' effect.* Four portions of Sea Beam swaths adjusted for navigation are shown here to illustrate the effects of a non-zero manual threshold when the Echo Processor runs in mode 2 or 3. Sea Beam's rendition of the bathymetry is seen as a trough approximately centered on the ship's track. This trough persists through changes in the ship's course, thereby indicating its artificial nature. Fictitious gullies also appear on slopes updip as well as downdip (best seen in the upper right section of this figure). Contour interval is 10 m and tick marks point downhill.

The actual seafloor morphology in this area is not precisely known because the MPL acoustic data acquisition system was not available during this survey. This area is believed to be generally flat with indications of roughly North-South abyssal hill trends. Such 'tunnels' might be mistaken for troughs between abyssal hills or submarine channels, but investigators would recognize them as artificial because the trough axes follow the ship track, independent of course changes.

The tunnel effect can also occur when a zero manual threshold has been entered, even though the system computes a noise and a sidelobe threshold. In the example given in Figure 1.5, we identify two processes which combine to defeat the sidelobe rejection scheme outlined in the appendices. First a very strong specular return was received at the hydrophones, indicating a highly reflective seafloor. Second the EP receiver outputs were found to saturate at 8.5 volts rather than the specified maximum output of 10 volts [de Moustier, 1985a]. As a result the peak amplitude on the specular return is clipped (starboard beam #1 in Fig. 1.5). The sidelobe threshold level computed on a clipped peak only partially removes the sidelobe response, and the remaining portions of sidelobe response bias the center of mass calculation in their direction given the comparatively low signal to noise ratio of the real backscattered bottom returns. Eventually, the system tracks the sidelobe response instead of the bottom, creating a trough-like feature. The limiting case is that of a mirror-like hard surface from which there is no backscatter. In this case, one would see only a strong specular return and a synchronous ridge of sidelobe returns. However, most of the time the bottom offers some roughness on the scale of Sea Beam's 12 cm acoustic wavelength, and the signal to noise ratio of the backscattered returns is sufficient to track the bottom correctly.

It is important to note that the prerequisite for sidelobe interference is a strong near-specular return on any one of the preformed beams. The bottom does not

necessarily have to be flat [e.g. Renard and Allenou's example]. In cases where the sidelobe response is well separated from the bottom return (e.g. port beam #8 in Fig. 1.5), it usually falls outside the tracking gates. When the sidelobe and the actual bottom returns are close together or overlapping, as is usually the case on returns adjacent to the near-specular return (e.g. port beam #1 in Fig. 1.5), the system has no way of differentiating between sidelobe response and bottom return. Rejecting the sidelobe response will most likely cancel some of the bottom return, resulting in a slightly erroneous depth determination. Likewise the computed depth is in error if the sidelobe response is not rejected. The errors are small ($\sim$ 5 m) for beams oriented in the near-specular directions, and increase away from specular incidence due to the lengthening of the backscattered return signal duration (pulse stretching) with both beam angle and depth.

I.4.2 Interference from external sound sources

External sound sources interfere with the Sea Beam system when they transmit while Sea Beam is receiving echoes from the seafloor. Figure 1.7 shows an example of a 3.5 kHz echo-sounder interference as seen in the acoustic data. It appears as a synchronous ridge across the sixteen preformed beams. This is a classical example of a noise burst. As for the sidelobe interference, the dynamic thresholding used to reject such noise bursts has side effects which produce fictitious bathymetry, examples of which can be seen in Figure 1.8. The portion of the noise burst which is well separated from the actual bottom returns are effectively rejected by dynamic thresholding or by gating. However where signal and noise burst overlap, canceling the noise burst also cancels part of the signal and skews the center of mass calculation for that return. As the noise burst slowly progresses through the reception cycle over a number of pings, bathymetric peaks appear on the contoured output in the direction of the beams which point away from specular incidence. The near-specular directions

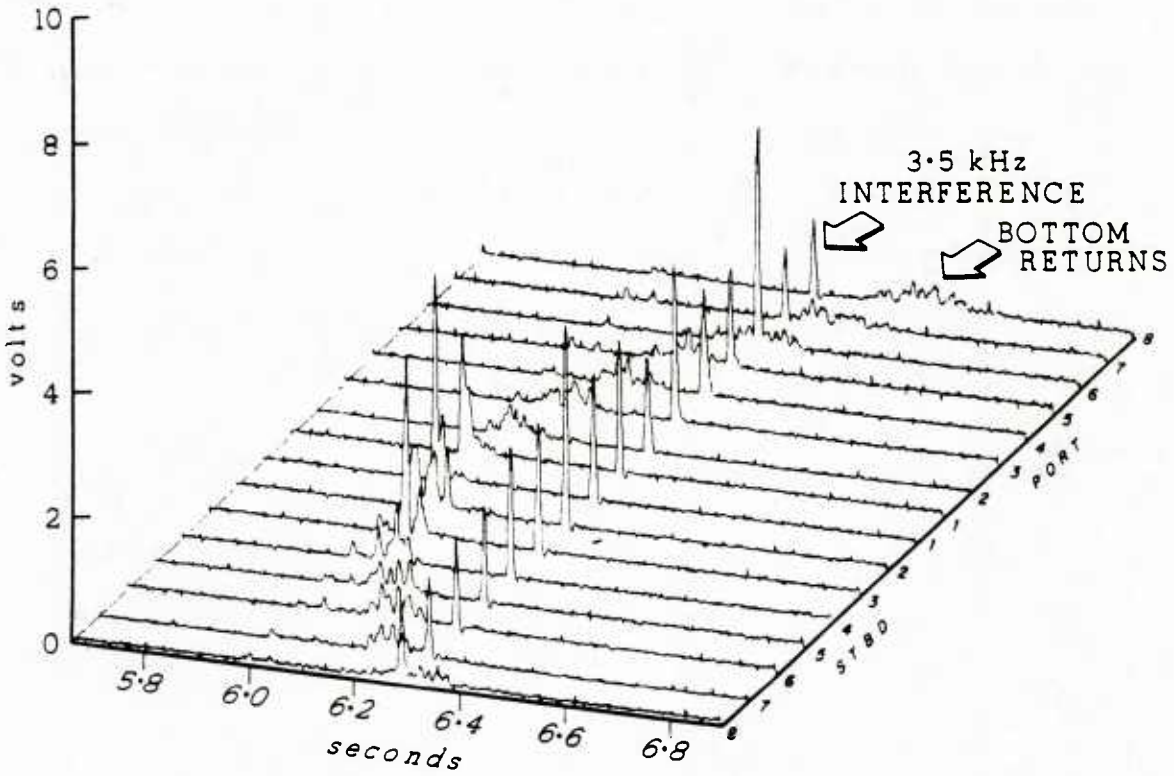

Figure 1.7 *Evidence of a 3.5 kHz echo-sounder transmitting during a Sea Beam reception cycle.* The corresponding noise burst appears as a synchronous ridge across all sixteen preformed beams. The format is the same as that of Figure 1.3. A noise burst ridge differs from a sidelobe response ridge in that the levels of the peaks are more or less constant for the former while a marked difference in level exists between the specular return and its corresponding sidelobe response (Figures 1.3 and 1.5). The differences in level seen in this figure are due to differences in receiver gains which were not corrected.

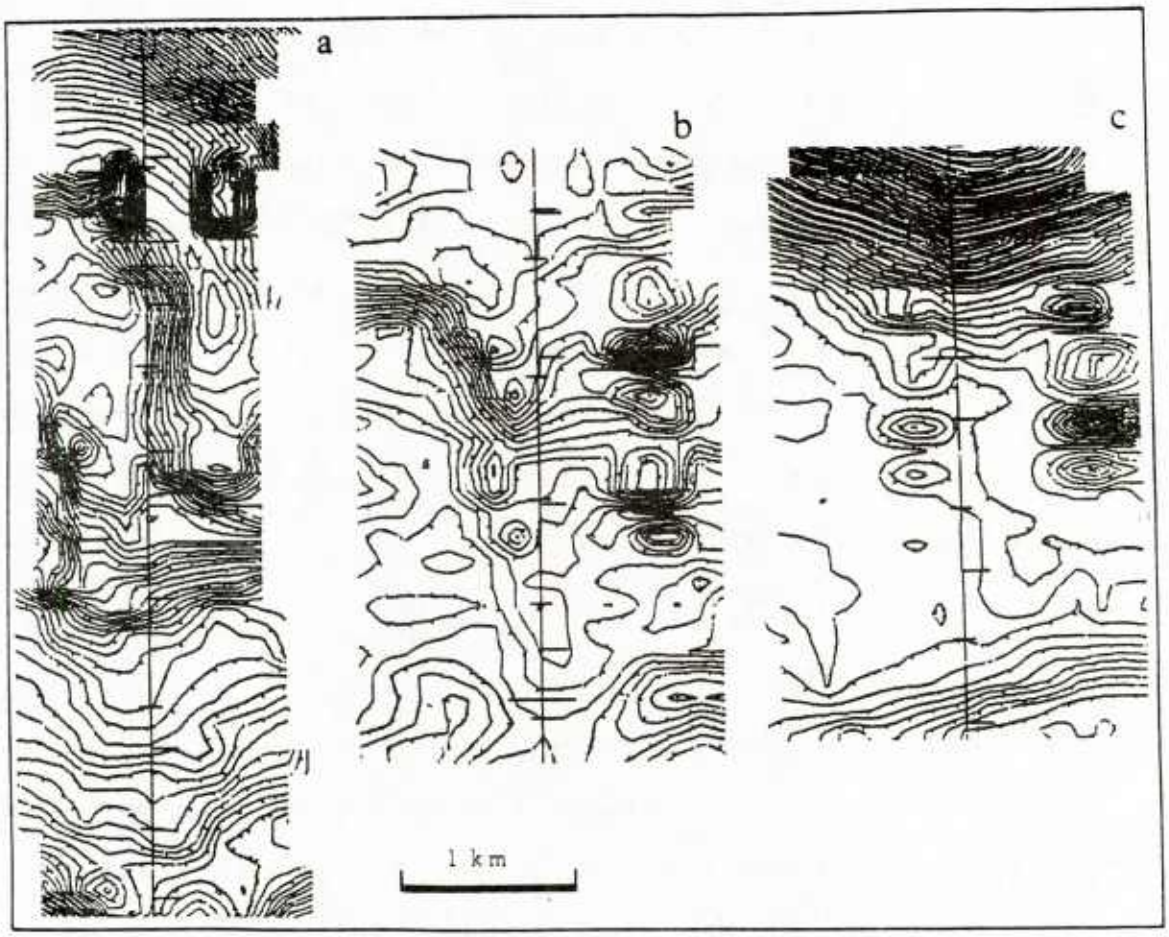

Figure 1.8 *Examples of contoured swath plots showing the results of external sound source interference.* Artifacts can be recognized as individual peaks on one or both sides of the ship's track (center line in all 3 plots). Contour interval is 10 m and tick marks point downhill.

are not affected as much since pulse stretching is minimal, thereby reducing the margin for error.

The bathymetric peaks are typically short wavelength (hundreds of meters) and may vary in amplitude from tens to hundreds of meters. The more pronounced of these peaks are often clearly spurious and extremely steep and sharp; such features are geologically unlikely and investigators will readily disregard them. Smaller amplitude artifacts are less obvious, and might be mistaken for small volcanic cones or large hydrothermal mounds. One common, although not ubiquitous characteristic of these artifacts is the simultaneous occurrence of more than one in different parts of the swath. Investigators aware of the potential for these phenomena are unlikely to misinterpret them. Seismic sound sources such as waterguns produce similar effects, but no observable interferences have been reported with airguns, probably because they do not output enough acoustic energy in the 12 kHz frequency band [Smith, 1983].

A special case of interference from external sound sources exists for 12 kHz bottom transponders. Figure 1.9 shows an example of such interference with evidence of a transponder trace on the corresponding analog center beam depth profile. The flat sedimentary bottom over which this data was taken illustrates the progression of the interference. The interference enters the outer beams' tracking gates while falling outside those of the near-specular beams. This is evidenced in Figure 1.9a by a central ridge followed by two small mounds on either side of the ship's track. The small mounds would be difficult to identify as artificial, were it not for evidence from the analog record (Fig. 1.9b) which shows the transponder trace intersecting the center beam depth profile at the corresponding time. Due to their small size, these artifacts would probably not be considered very significant, although some might mistake them for satellite cones or hydrothermal mounds.

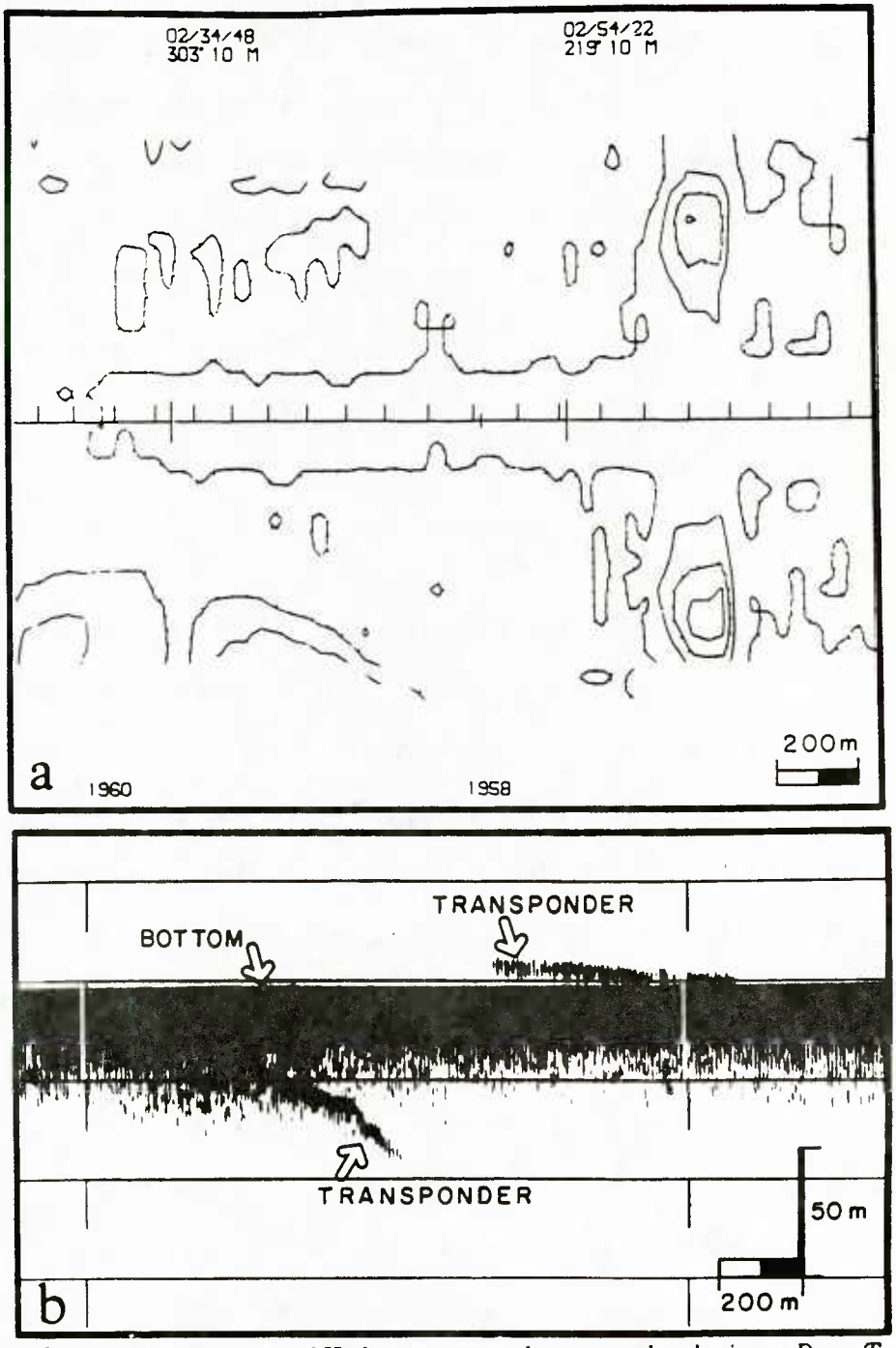

Figure 1.9 *Interference from a 12 kHz bottom-moored transponder during a Deep Tow survey.* (a) Sea Beam near-real time contoured output. Contour interval is 10 m and tick marks point downhill. The center line represents the ship's track. On this line, short ticks above the ship's track are spaced 2 minutes apart, long ticks refer to information at the top of the plot [time (hour/min/sec), ship's heading, contour interval in meters] and short ticks centered on the track refer to center beam depth in meters indicated at the bottom. (b) analog graphic recorder output displaying Sea Beam's center beam depth profile and the trace of the 12 kHz transponder. The horizontal scale is matched in time to that of Figure (a) The artifact can be seen in (a) as the two small mounds on either side of the ship's track.

The situation of this example is uncommon because the ship was maneuvering at about 1.5 knots over a bottom transponder network while towing *Deep Tow* instrument package. However, it may become more common with the Sea Beam system installed on WHOI's R/V *Atlantis II,* the mother ship for the manned *DSRV Alvin* which is often navigated using 12 kHz transponders. At normal survey speeds ($\sim$ 10 knots) this artifact would be greatly reduced. Similar artifacts due to interference from the direct or the bottom bounced signal of a 12 kHz pinger have also been noted during dredging or coring operations.

I.4.3 'Omega' effects and data gaps

Most Sea Beam users are aware of the possibility of sidelobe or external sound source interference in the system. A lesser known and more insidious artifact has been found to occur on sloping bottoms producing contours resembling the capital Greek letter omega (Ω) [Kleinrock et al, 1984] or data gaps. They are generally characterized by an arcuate plateau followed by a steep, curvilinear scarp. They occur within a single Sea Beam swath, commonly near the center, and have lateral dimensions of hundreds to thousands of meters. The plateaus may be peaked (Fig. 1.10e) or flat (Fig. 1.10d). The scarp may be semicircular (Fig. 1.10d -- the classic Ω shape) or irregular (Fig. 1.10f). 'Omegas' sometimes evolve into, or are associated with data gaps (Figs. 1.10b and 1.10g), and can be created on sides of seamounts (Fig. 1.10c) as well as relatively straight scarps.

Figure 1.10a shows the problem clearly. In this case, the same portion of seafloor has been surveyed in 3 different directions. The arrows indicate the direction of ship travel. In Figures 1.10a.1 and 10a.2 Sea Beam's rendition of the bathymetry is nearly identical for opposite ship courses in the along slope direction. The bathymetry is markedly different when the ship track runs downdip (across a slope in the down hill direction) (Fig. 1.10a.3). In all the colored contour plots shown, contour lines have

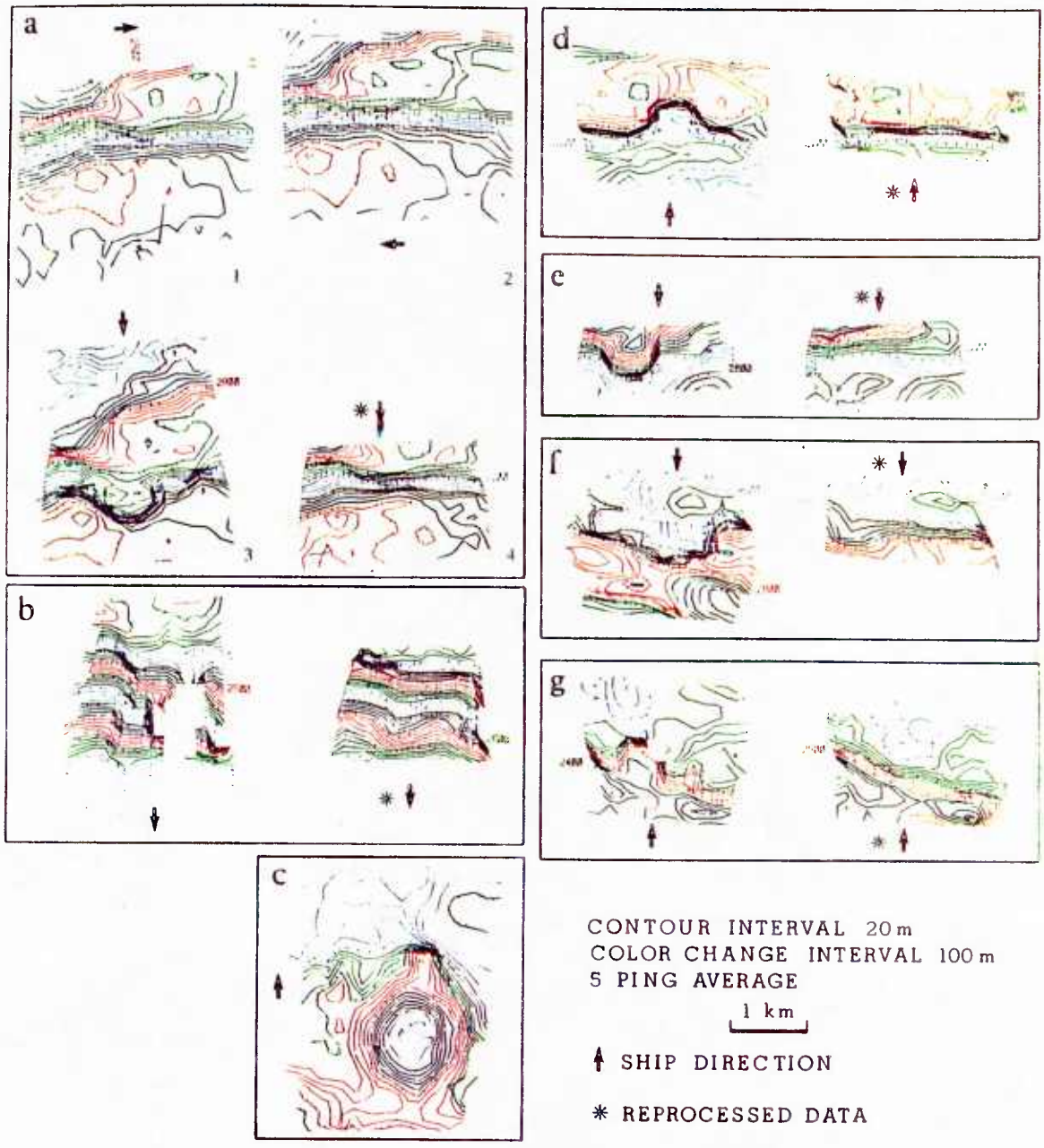

Figure 1.10 *'Omegas' and gaps.* Tick marks point downhill. Contoured sections not starred are original Sea Beam data. Contoured sections marked with a star are the result of reprocessing the acoustic data recorded digitally with the MPL system. Our simplified echo processing technique does not include ray-bending corrections and arrival times are determined by the first arrival above a preset threshold. The threshold level is selected after visual inspection of the roll-compensated acoustic data. Recomputed depths and cross-track distances are therefore in uncorrected meters referenced to a sound velocity of 1500 m/s. Although crude, this processing method suffices to prove the fictitious character of Sea Beam's contoured bathymetry shown in (a.3), (b), (d), (e), (f), and (g). We do not show a recomputed version of (c) because the corresponding acoustic data was only recorded every five pings. This was enough to confirm the 'omega' effect but contour resolution was seriously degraded by the five ping decimation.

been smoothed by averaging over five transmission cycles. While inspecting the raw Sea Beam data, we noticed unrealistic variations in depth from one ping to the next as well as missing soundings in the data of Figure 1.10a.3. No evidence of external interference was found in the acoustic data. After computing depths and cross-track distances from this acoustic data, we contoured them using the same post-processing software used throughout Figure 1.10. The resulting bathymetry shown in Figure 1.10a.4 matches that seen in Figures 1.10a.1 and 1.10a.2. Sea Beam was clearly in error when the ship track ran downdip.

A combination of three factors may be responsible for this artifact. First of all, the automatic bottom-tracking gates do not open fast enough upon a sudden change of bottom slope. As a result, data are lost for points falling outside the gates. Secondly, when going downdip across a slope the fore-aft transmit beam pattern geometry (Fig. 1.2.a) is such that acoustic energy from the sidelobes may ensonify the slope in the specular direction. Although this transmitted energy is about 25 dB lower than that transmitted in the mainlobe in the true vertical direction, it becomes significant due to the angular dependence of backscattering. Measurements have shown that one can expect a drop of 10 to 15 dB in the acoustic backscatter between normal (specular) incidence and 20 degrees incidence [Patterson 1969, Urick 1983]. For a flat bottom the acoustic backscatter due to sidelobe transmitted energy is negligible compared to the returns due to the main beam in the specular direction. This is no longer true when the bottom slope is such that the sidelobes of the transmit beam pattern point in the specular direction as in this case. Because the receiving beam pattern is 20 degrees wide in the fore-aft direction (Fig. 1.2b), early returns are received as seen in Figure 1.11. Given the proper threshold and sufficiently narrow tracking gates (which is the case when the bottom has remained relatively flat for some time), the system tends to track these early returns, creating a plateau-like feature. At some point the signal to noise ratio of these returns becomes too low and

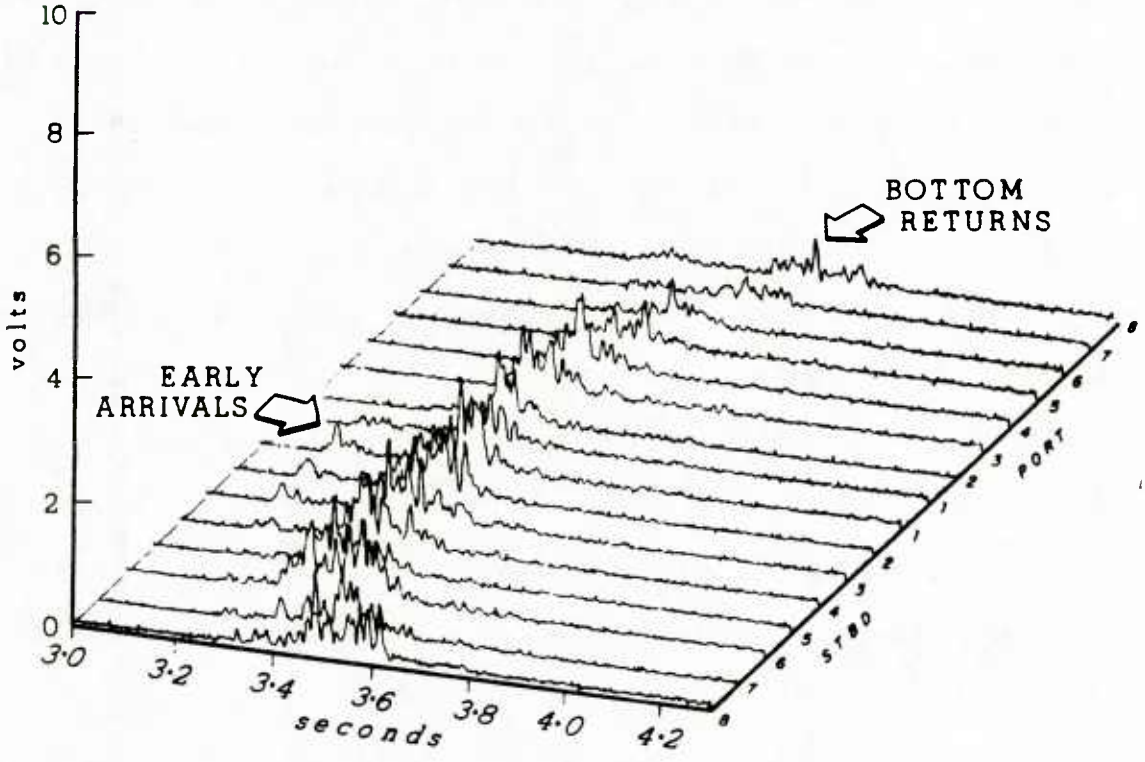

Figure 1.11 *Evidence of transmit beam pattern sidelobe interference in the digitized acoustic data.* Early arrivals corresponding to near-specular returns from transmited sidelobe energy are best seen on starboard beams 1-3. These data correspond to the 'omega' effect shown in Figure 1.10e. The format is the same as that of Figure 1.3.

the system fails to detect an echo until the tracking gates open wide enough to recover the real bottom. Hence a sharp drop in depth results at the end of the plateau as shown in the cartoon of Figure 1.12a.

Consider two possible tracking gate conditions: a normal condition where the instantaneous bottom profile is contained within the gates (Fig. 1.12b), and a condition where part of the profile falls outside the gates (Fig. 1.12c). The latter produces a data gap as seen in Figures 1.10b and 1.10g where the onset of an 'omega' effect immediately precedes the gap. Apparently, the dip of the bottom increased too rapidly for the 'omega' effect to fully develop, and a gap appeared because the gates simply could not open fast enough. Such gaps exist in Sea Beam data on updip as well as downdip ship tracks, however in our data we have seen 'omega' effects only for downdip ship tracks. This was confirmed at sea when an observed 'omega' effect on a downdip track was immediately resurveyed updip, and no 'omega' was detected. The most likely explanation for this asymmetry comes from the fact that the gates are always lagging upon a sudden change in bottom slope. Downdip, the gates track from the left in Figure 1.11 and they are therefore likely to track early returns. Updip the gates track from the right in Figure 1.11 so they have a better chance to track bottom returns instead of early arrivals. Also the gates have more time to adjust at the base of rising slopes due to the accumulation of talus. We cannot specify a slope range for which an 'omega' effect occurs because this effect varies with ship's speed and depends on the sidelobe level on the transmit beam pattern of the Sea Beam system considered. As ship speed is reduced, the tracking gates have more transmission cycles to adjust to a sudden drop in slope and the 'omega' effect is less likely. Our data shows 'omega' effects on slopes between 30 and 45 degrees for ship speeds of about 10 knots, but similar though subtler artifacts seem to appear on gentler slopes, perhaps as low as 15 degrees.

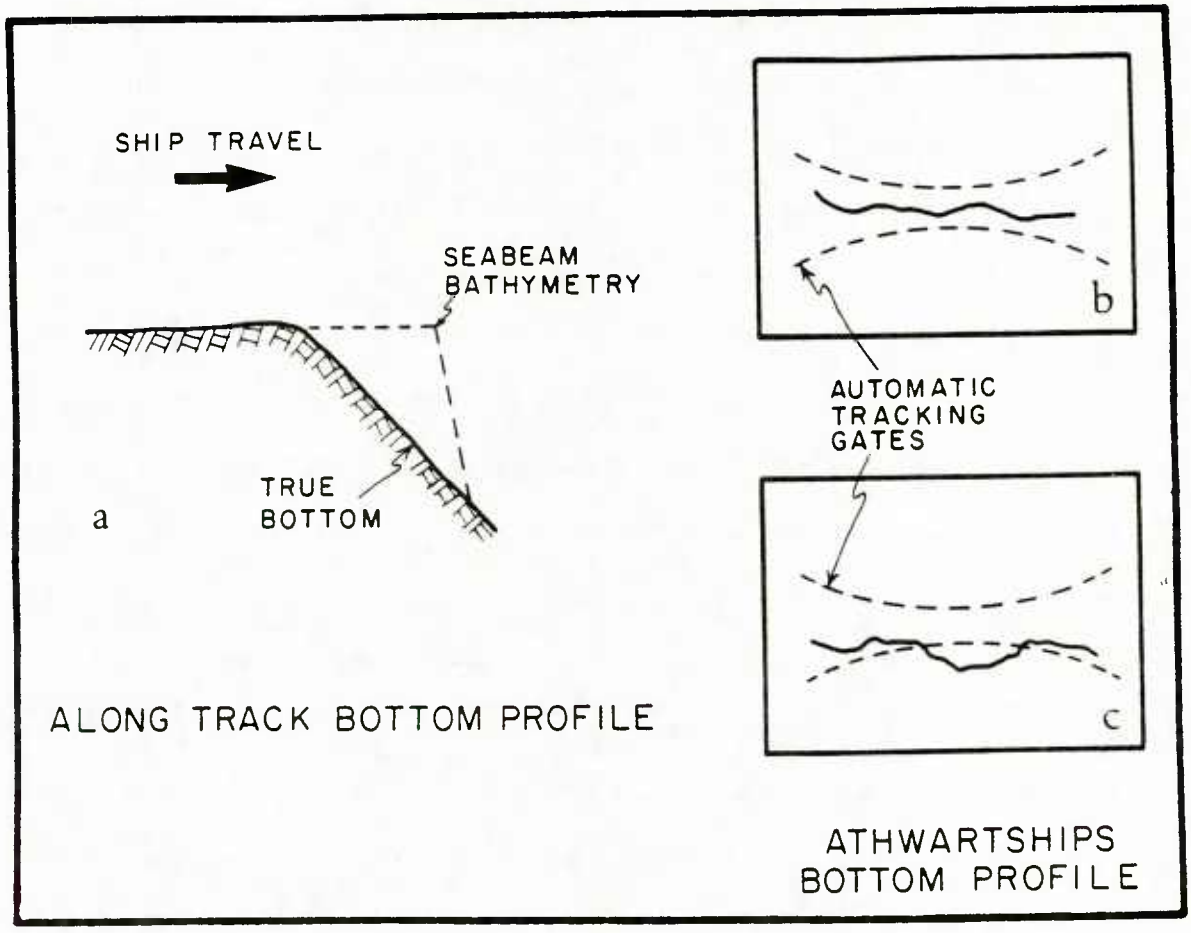

Figure 1.12 *Cartoons of bottom profiles associated with 'omegas' and gaps.* (a) Along track bottom profile of an 'omega' artifact. Sea Beam's rendition of the bathymetry, shown by the dashed line, is a plateau followed by a steep scarp. (b,c) Bottom-tracking gates conditions as would be seen on the Echo Processor's CRT. In (b) the athwartships bottom profile (solid line) lies inside the tracking gates (dashed lines). This is the normal mode of operation when the Echo Processor is in mode 3. It is also what one would see were an 'omega' effect present. In (c) the athwartships bottom profile lies partially outside the tracking gates and the corresponding data points are lost. This situation is characteristic of data gaps.

The tracking gates and the transmit/receive acoustic geometry are the two main factors contributing to the 'omega' effect. A third factor is related to the half-hour calibration of the EP receivers. In several instances, we found that this calibration occurred immediately prior to an 'omega' effect. Figure 1.13 shows the onset of a receiver gain calibration sequence just at the end of a reception cycle. The following transmission cycle showed only the calibration signals. Inspection of the raw Sea Beam data showed that no data had been logged for these two cycles even though one would have expected the first (Fig. 1.13) to have been processed by the EP. As a consequence, data are lost for two transmission cycles every half hour. Moreover the tracking gates are not updated during this time. A coincidental increase in bottom slope puts the EP in a difficult bottom-tracking situation which, given the appropriate slope angle, ship direction and signal-to-noise ratio in the acoustic returns, generates an 'omega' effect.

Of all the artifacts discussed here, 'omega' effects are the most likely to mislead investigators because they often appear as geologically plausible volcanic, tectonic or even depositional (mass-wasting) features. An 'omega' on the side of a seamount as in Figure 1.10c, could possibly be mistaken for a flank or satellite construct. Irregular 'omega'-type artifacts (Fig. 1.10f) appearing on what are actually relatively straight scarps might be misinterpreted as changes or variations in structural trend. This could result in errors in determining the tectonic character and evolution of an area. Other 'omegas' (Fig. 1.10e) might be mistaken for volcanic constructional features and incorrect conclusions could be reached regarding post- or syn-tectonic volcanism on scarps such as fracture zone walls, rift valley walls, pseudofault walls, abyssal hill scarps, caldera walls, etc. In addition, some 'omegas' might be mistaken for serpentinite diapirs, while others (for example at trenches or submarine canyons) could be erroneously identified as slump blocks or other mass-wasting deposits. When dealing on scales of hundreds of meters to several kilometers,

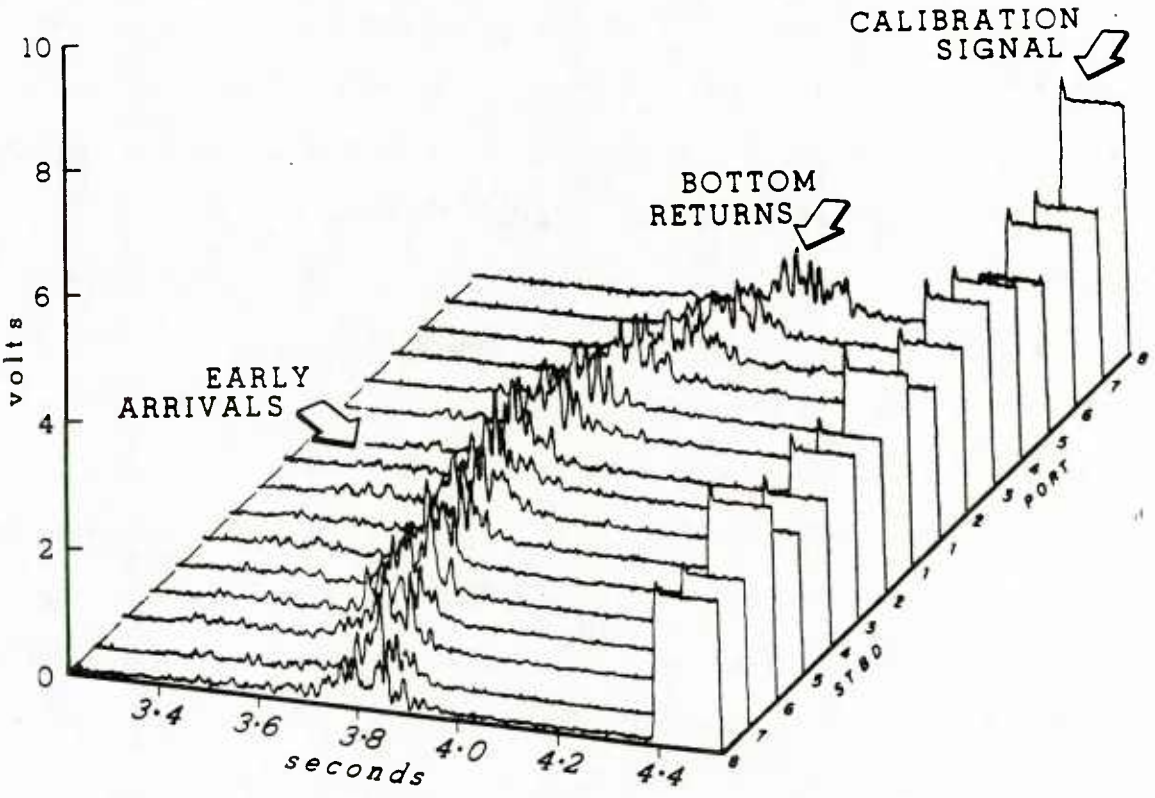

Figure 1.13 *Receivers' gain calibration.* The raised signals seen at the end of each of the sixteen preformed beam returns represent calibration signals injected into each receiver to determine its gain setting. Here one can appreciate the usefulness of the Echo Processor gain correction which brings all receivers to a common gain level. The format of this figure is identical to that of Figure 1.3.

failing to recognize 'omegas' as artifacts could lead to errors in geologic understanding, because they might suggest unexpected volcanism or tectonism in supposedly inactive areas. The implications of these possible misinterpretations are very important.

Suspicious features which have the characteristic shape of 'omegas' have been observed in data from every Sea Beam survey we have investigated thus far. Many geophysical surveys are run orthogonal to the tectonic fabric because important variations in magnetic, seismic, gravity and bathymetric data often are found in cross-strike profiles. Unfortunately, because 'omegas' are found on downdip tracks, this type of survey pattern increases the probability of occurrence of these artifacts. In an effort to quantify this probability, we have analyzed data from such a survey (Fig. 1.14). Figure 1.14 shows Sea Beam data from the propagating rift at 95.5° W on the Cocos-Nazca spreading center [Hey et al., 1985a]. In this figure, all areas where the gradient of the bathymetry, as detected by Sea Beam, exceeds a specified slope are darkened. Figure 1.14a is included mainly to show the data density and the overall tectonic structure. The 'omega' effect was discovered while analyzing this dense data set with several overlapping swaths and the 'omegas' shown in Figure 1.10 are examples of artifacts that Hey and coworkers removed from their data. In eight cases for which we initially suspected the 'omega' bathymetry to be false, and then studied the acoustic data, our suspicions were confirmed. By checking the raw Sea Beam data, we have identified eight others. We then estimated the probability of encountering 'omegas' on downdip tracks over fairly steep slopes. We have visually examined the computer-generated Sea Beam 20 m contour plots and identified all the 'omegas' which we feel confident are artifacts (many questionable examples were also found, but not included in the exercise). Triangles in Figure 1.14b mark the locations where features on this plot are associated with 'omegas' seen in the contour plots. Knowing the direction of ship's travel, we were able to distinguish on this figure those downdip

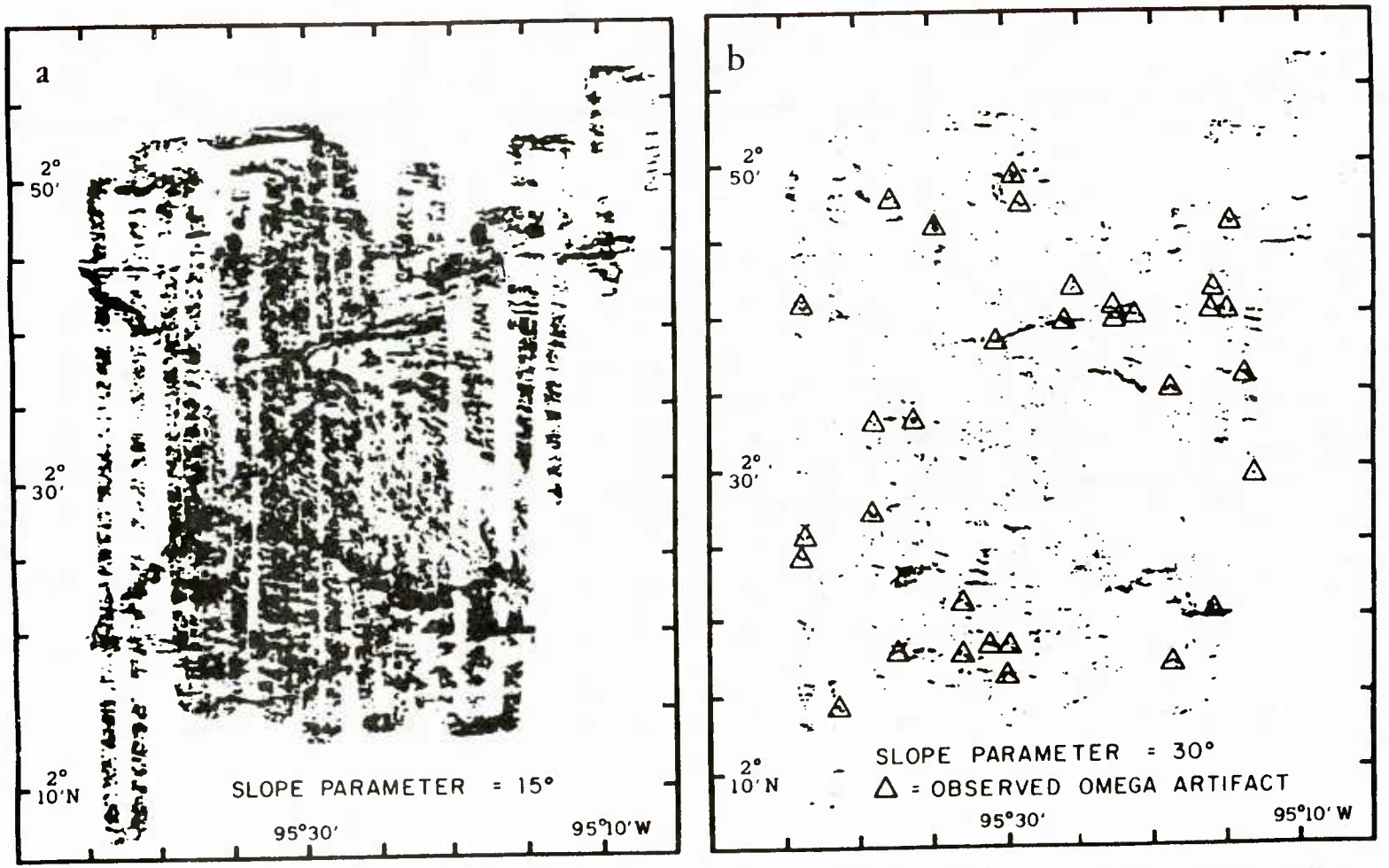

Figure 1.14 *Bathymetric gradient charts of Sea Beam data from Galapagos 95.5°W propagating rift survey [modified from Hey et al., 1985a].* All areas where five-ping averaged Sea Beam data exhibit slopes greater than the slope parameter (specified in the lower right of each plot in degrees from the horizontal) are darkened. (a) slope parameter = 15°. Data coverage and tectonic fabric [mostly E-W, see Hey et al., 1985a for discussion] of this rugged terrain are visible in this plot. (b) Slope parameter = 30°. Triangles show locations of features appearing on this plot that are associated with 'omega' artifacts seen in 20 m contour plots.

slope crossings which have 'omega' artifacts and those which do not. For approximately 50% of all occurrences where the ship steamed downdip across slopes which Sea Beam detected as being greater than 30 degrees, 'omega' artifacts are present. Though we realize these estimates are rough, the salient point is clear: 'omega' artifacts can be very common in conventional surveys which run perpendicular to the tectonic fabric. As mentioned above, the frequency of occurrence of these artifacts may vary with each Sea Beam system depending on the sidelobe level of its transmit beam pattern, as well as with ship's speed.

Our detailed analysis of these artifacts has concentrated on the SIO Sea Beam system because of the availability of its acoustic data. But we have observed 'omega'-like features in bathymetric data collected with systems aboard the R/V's *Conrad* (Lamont-Doherty Geological Observatory), *Surveyor* (National Oceanographic and Atmospheric Administration), and *Jean Charcot* (IFREMER). Sea Beam investigators who see suspicious features with characteristics similar to the 'omegas' shown here would be prudent to survey the sites with crossing Sea Beam swaths for confirmation before attributing them great significance or planning higher resolution studies. If such features are not recognized as potentially important until after the survey, the raw Sea Beam data, should be checked looking for unrealistic depth changes from one ping to the next, and for missing data points which indicate that the system lost tracking of the bottom during that time.

Although we have only analyzed data from the Sea Beam system, we believe similar multibeam echo-sounders might output the same artifacts. The U.S. Navy SASS system has been in operation since 1965, and some of its data has been declassified for use on the Mid-Atlantic Ridge Rift Valley [Phillips and Fleming, 1978; Ballard and van Andel, 1977] and on the Galapagos Rift at 86°W [van Andel and Ballard, 1979; Crane and Ballard, 1980]. Comparison of SASS bathymetry with *Deep*

Tow bathymetry [Crane, 1978; van Andel and Ballard, 1979] seems to indicate that 'omega'-like artifacts exist in SASS data. Data gaps and onsets of 'omegas' similar to those of Figure 1.10b are also apparent in Phillips and Fleming [1978] (e.g. Figure 3D in their paper).

I.5. POSSIBLE CORRECTIONS

Depths and cross-track horizontal distances cannot be recomputed as a post-processing operation unless the acoustic data is digitized and recorded on tape as was done for our data. Therefore, investigators discovering fictitious bathymetry in their data have no alternative but to disregard the portion of data affected. Also, these artifacts occur too infrequently to warrant recording of the acoustic data on a routine basis. Rather than relying on data reprocessing, it seems more sensible to deal with the problems at their source. In the following we suggest a number of solutions to the problems discussed in the previous section.

I.5.1 Possible Corrections for Sidelobe interference

When a 'tunnel' effect develops during a survey, it is common practice to switch the EP from mode 3 to mode 2 [Smith, 1983]. As a result the automatic tracking gates open to their maximum (upper and lower limits of the CRT display) according to parameters set by the Sea Beam operator. A subsequent return to mode 3 resumes automatic tracking. This method has proven effective in dealing with the 'tunnel' effect which is essentially sidelobe response related. However it relies on the vigilance of an operator and it will not correct the effect pointed out by Renard and Allenou [1979]. In general the current sidelobe response suppression technique suffers from the saturation in the EP receivers. A simple modification of the detection amplifiers may solve the saturation problem, but use of logarithmic detection amplifiers to increase the EP receivers' dynamic range seems desirable [de Moustier,

1985a]. At present there is no way to control the performance of the amplitude shading in the receiver array. As an example, we changed the shading coefficient by 30% on four array elements in the computed beam pattern of Figure 1.2b. It brought the sidelobe level from 30 to 23 dB below the mainlobe. This may not appear as significant since the sidelobe threshold computation is based on a value of 12 dB below a peak amplitude, which is approximately the sidelobe level of an unshaded array (Fig. 1.2b). However, we believe that ensuring optimum performance of the array amplitude shading can only benefit any subsequent sidelobe response rejection scheme.

As the EP works on the rectified envelope of the return signals, it has no way of differentiating between sidelobe response and actual bottom return when the two overlap. To tell them apart requires phase information which is not available to the EP in the current mode of operation. One way to deal with this problem would be to heterodyne (multiply by an external oscillator frequency and filter in the desired frequency band [Clay and Medwin, 1977]) each of the sixteen preformed beam channels to obtain 16 channels of complex data (32 channels of real data). These could be digitized and processed as currently done in the EP. It would then be possible to apply advanced adaptive filtering techniques [McCool and Widrow, 1977] to effectively cancel sidelobe response as well as noise bursts while retaining the real bottom return signal. Of course, such a scheme might be hampered by the processing time required and it needs to be tested.

I.5.2 Possible Corrections for Interference from external sound sources

Whenever the 3.5 kHz echo-sounder is run in conjunction with Sea Beam aboard the *R/V Thomas Washington*, the analog graphic recorder is used to display both the Sea Beam center beam profile and the 3.5 kHz echo-sounder outgoing pulse. Interference occurs when the corresponding signal traces intersect. To prevent this, it is necessary to phase delay the 3.5 kHz outgoing pulse enough to keep the two traces

separated [Smith, 1983]. This method is not entirely reliable since it requires an operator. A more reliable method consists of using a simple electronic circuit which gates out 3.5 kHz transmission whenever a Sea Beam reception cycle is in progress. Such a device reportedly works well on the *R/V Conrad* [Tyce, 1984]. Unfortunately, this device will not prevent interference from 12 kHz transponders, pingers or seismic sound sources. The latter usually cannot be phase delayed for mechanical reasons (constant pulse energy requirement) as well as data post-processing reasons (constant firing rate requirement). A solution which takes into account the transmission rate requirements of all possible underwater sound sources available aboard a ship can be implemented on the shipboard computer. With a knowledge of the water depth, the computer would decide the best firing sequence necessary to keep the sound sources from interfering with each other (J.L. Abbott, SIO: personal communication).

I.5.3 Possible Corrections for'Omega' effects and data gaps

'Omegas' and data gaps are dealt with in the same way the 'tunnel' effect is, by switching the EP from mode 3 to 2 and back again. However, there is no way to detect an 'omega' effect in real-time since the cross-track bottom profiles on the CRT appear to be within the gates, and by the time evidence of it is seen on the swath plot it is usually too late to correct anything. The automatic tracking gate software was modified by the manufacturer in October 1984 on the system installed aboard the German *R/V Polarstern* (W. Capell, General Instrument Corp: personnel communication). The changes consisted of increasing the minimum allowable width for each gate and enabling a faster rate of change of the gates from ping to ping. Sea Beam systems installed since October 1984 benefit from this modification which has proven effective in substantially reducing the problems of data gaps and 'omega' effects. However, the widening of the bottom-tracking gates tends to decrease the depth determination accuracy on the outer beams because the remaining sidelobe

response is no longer gated out on those beams.

Because of the side effects of the EP receivers' calibration, mentioned in Section I.4.3, we recommend that an additional change be made to allow the gates to widen during a calibration cycle. This way a coincidental increase of bottom slope will easily be accommodated by the EP upon return to a normal reception cycle. Also, it would be useful to have the half hour calibration, which is triggered upon interrupt from the Sea Beam computer clock, wait for the completion of the transmission cycle in progress and avoid situations such as that of Figure 1.13. Data would then be lost for only one transmission cycle and the updating of the tracking gates would be more reliable.

Finally, as for the receiver array, some measure of the performance of the projector array amplitude shading seems necessary. At present the system tests the performance of the power amplifiers on an all or nothing (blown fuse) basis. Tyce [1984] reported deviations from the manufacturer's specifications by as much as 40% on the outputs of four projector elements for the system installed aboard the *R/V Conrad*. For comparison a change of 40% in the shading coefficients of four elements in the computed beam pattern (Fig. 1.2a) moved the sidelobe level from 30 dB to 22 dB below the mainlobe. Such levels will definitely enhance the signal to noise ratio of early specular returns discussed in Section I.4.3 (Fig. 1.11), increasing the probability of 'omegas'.

I.6. CONCLUSIONS

In conclusion, we would like to stress the importance of a clear understanding of the capabilities and limitations of the Sea Beam system when analyzing its output. We fully recognize the value of Sea Beam bathymetry in conducting a survey and in describing abyssal morphology. This paper attempts to make the scientific community aware of a number of bathymetric artifacts observed in Sea Beam data which, if

unrecognized, might lead to geological misinterpretations. We have shown that artifacts due to external sound sources (e.g. subbottom profilers) or internal sidelobe interference can usually be clearly identified as resulting from spurious data. In most of these cases, corrective action can be taken in real-time while surveying. We also discussed a more insidious artifact (the 'omega' effect) which is virtually impossible to detect in real-time for lack of warning. In addition, such artifacts commonly found when steaming downdip over slopes greater than 30 degrees may appear as geologically plausible volcanic, tectonic or sedimentary features. When navigation is based on seafloor morphology, failure to recognize bathymetric artifacts may lead to positioning errors.

In order to explain the causes of these artifacts, we have analyzed Sea Beam's echo detection and processing techniques. Errors have been found to relate to the methods of sidelobe rejection, automatic bottom-tracking and automatic receiver gain calibration. These errors result in incorrect depth determinations which cause the artifacts observed. Because Sea Beam only retains depths and cross-track horizontal distances from the received acoustic signals, investigators have no alternative but to disregard the bathymetric artifacts they identify. A number of corrections are proposed to prevent such data disposal: improved sidelobe control in the transmit/receive acoustic geometry, extension of the EP receivers' dynamic range, sidelobe and noise burst rejection through advanced adaptive filtering techniques, improved bottom-tracking gate operation, delayed receivers' gain calibration to allow for completion of the reception cycle in progress, and computer coordinated signal transmission for all active sound sources during a survey.

Recently, presentation formats for Sea Beam data have extended beyond contour maps to include gray-tone and color shaded relief maps [Edwards, et al., 1984], and bathymetric gradient charts [Hey et al., 1985a]. These formats are very

valuable in interpreting the data, however 'omegas' and other bathymetric artifacts will persist, because the errors are in the raw Sea Beam data, not in the contouring algorithm employed.

I.7. ACKNOWLEDGMENTS

The work reported here would not have been possible without the cooperative efforts of the captain and crew of the *R/V Thomas Washington.* We wish to thank W. Capell from GIC for his patience in answering our numerous questions, R. N. Hey, P. F. Lonsdale, J. L. Abbott, T. H. Shipley and P. C. Henkart for helpful comments and data samples; R. C. Tyce for initiating the Sea Beam acoustic backscattering experiment at MPL and F. V. Pavlicek for his support during the development of the Sea Beam acoustic data acquisition system. We are indebted to R. N. Hey, K. Crane, J. A. Hildebrand and S. P. Miller for their valuable suggestions and critical review of the manuscript. We are also grateful to J. Barron and E. Ford for typing and editing and J. Griffith for the art work. For their support, we thank the Office of Naval Research (Contract No. N00014-79-C-0472), and the National Science Foundation (Grant No. OCE-8109927).

I.8. APPENDIX A: Sea Beam Acoustic geometry

In the following, the beam widths are calculated at the half power point of the beam patterns. The transmitted beam pattern spans 54 degrees athwartships by 2 2/3 degrees in the fore-aft direction. It is pitch stabilized to ensure vertical projection by phasing the outputs of the twenty power amplifiers relative to a pitch angle supplied by the vertical reference gyroscope (Fig. 1.1) within the limits of $\pm$ 10 degrees of pitch. As shown in the computed beam pattern (Fig. 1.2a) the projector array is designed for sidelobe attenuation 30 dB down from the mainlobe and grating lobes appear at 55 degrees on the fore-aft axis. The sidelobe level is controlled by amplitude shading the output of the twenty power amplifiers (Fig. 1.1) using the Dolph-Chebyshev amplitude shading method for acoustic arrays [Dolph, 1946, Riblet and Dolph, 1947]. Since the array is contained in a housing, the actual sidelobe level is 25 to 26 dB down from the mainlobe [Dolph 1946; Renard and Allenou 1979]. Proper control of the sidelobes on the transmitted beam in the fore-aft direction is crucial for adequate performance of the system when the ship's track runs downdip (across a slope in the downhill direction). In this geometry, weakly attenuated sidelobes ensonify the slope at near-normal incidence in the fore-aft direction. The corresponding bottom returns are received earlier than those due to vertical projection in the mainlobe, and they disrupt the echo processing and bottom-tracking functions.

The design of the receiving array yields a beam pattern which is 2 2/3 degrees athwartships by 20 degrees in the fore-aft direction (Fig. 1.2b). The 20 degrees beam width in the fore-aft direction is meant to accommodate pitch angles of $\pm$ 10 degrees as no pitch stabilization is performed on the receiving beams. Sea Beam generates sixteen preformed beams fixed with respect to the ship's vertical by electronically steering such 2 2/3 degrees beams at intervals of 2 2/3 degrees

athwartships from 20 degrees incidence on port to 20 degrees on starboard. Dolph-Chebyshev amplitude shading of the output of the forty preamplifiers (Fig. 1.1) attenuates the side lobes 30 dB below the mainlobe (Fig. 1.2b). For the same reasons given for the projector array, the actual sidelobe level may be somewhat higher. Renard and Allenou [1979] measured a value of 28 dB on two preformed beams. The acoustic data we have recorded indicates a mean sidelobe level of 25 dB below the mainlobe on ten preformed beams for the SIO system [de Moustier, 1985b]. Proper sidelobe level control is important for the receiving array, because each of the preformed beams has sidelobes oriented in the direction of the mainlobe of all the other beams. A strong return coming into the mainlobe of a particular beam will therefore be received by all the sidelobes pointing in the same direction.

I.9. APPENDIX B: Sea Beam Echo processing

Information concerning Sea Beam's echo processing is contained in the Sea Beam software technical manual [General Instrument Corp., 1981]. In the following we give, with the manufacturer's permission, an overview of the main features of the echo processing software. We emphasize the features important to understand the causes of the bathymetric artifacts discussed in this paper.

During each transmission cycle, 16 bottom returns (e.g. Fig. 1.3) are digitized by Sea Beam's analog-to-digital converter at a frequency of 300 Hz for each beam. For each conversion cycle the Sea Beam computer performs the following operations: receiver gain correction, refraction correction, roll compensation, detection threshold level determination, and signal detection for each of the roll compensated beams.

The receiver gain correction consists of multiplying the digitized signal voltage for each beam by an amplitude multiplication factor to compensate for differences among receivers. Because the roll compensation involves interpolation between beams, it is important that all 16 signals have a common gain at any one

time. The gains of the individual receivers are automatically calibrated by the EP every half hour by inputting a common voltage through the beam line drivers (Fig. 1.1), and digitizing the output of the receivers.

The refraction correction uses values of a sound velocity versus water depth profile, entered at the beginning of a survey by the Sea Beam operator, and Snell's law to calculate the reception angle Θ for each beam with respect to the ship's vertical. The sound velocity profile is measured with an expendable bathythermograph cast for the first few hundred meters and extended to the maximum bottom depth in the survey area using values from Carter's tables of sound velocity in the ocean [Carter, 1980].

The roll compensation uses the ship's instantaneous roll angle β given by the vertical reference gyroscope to reference the reception angle Θ to the true vertical: $\Phi = \Theta + \beta$. A set of stabilized beam angles Ψ spaced 2 2/3 degrees apart are then created. The amplitudes of the stabilized beams are linearly interpolated between those of the two adjacent preformed beams with corrected reception angle Φ_i and Φ_{i+1}. This yields fifteen stabilized beams each 2 2/3 degrees wide, fixed in a vertical plane athwartships with one beam aligned with the true vertical. As provision has been made for $\pm$ 20 degrees of ship's roll, there are thirty one possible stabilized beam positions between $\pm$ 40 degrees. Occasionally, one of the preformed beam angles Φ will lie on the true vertical ($\Psi = 0$) and there may be sixteen stablized beams.

A set of bottom-tracking gates determines the detection time window during which a bottom echo is expected based on previous sounding history. The tracking gate is an essential feature of the EP because it conditions proper echo signal detection and therefore reliable depth determination. Each beam has its own tracking gate. It is centered on the average depth for that beam using depth history over the last five transmission cycles (pings) weighted decreasingly into the past. The gate

width is determined by the observed ping-to-ping depth fluctuations with allowance for variations in signal duration due to beam angle, bottom slope and beam width. As a result, the gates are narrower for the near-vertical beams than for the outer beams. A constant value (20 m) is added to the width of each gate as a safety margin to ensure that the echo signal does not fall outside the gate. Bottom echoes falling outside the tracking gates are not taken into account by the EP which usually will not compute a depth and a cross-track distance for the corresponding beams for lack of signal to noise ratio. This situation creates a data gap. Since only fifteen (occasionally sixteen) of the possible thirty one stabilized beams bear data, gate settings for null or unused beams are interpolated or extrapolated from those of adjacent beams. Finally the gate settings are smoothed across all thirty one possible beams. The analog-to-digital conversion starts at the onset of the gate with the shallowest setting (earliest time). The conversion stops when the deepest gate has been reached.

The detection threshold level determination is a very critical operation in the echo processing. It is adjusted every conversion cycle, and is therefore a dynamic process taking several parameters into consideration: 1) the manual threshold level input by the Sea Beam operator, 2) the background noise level of the receivers, 3) the receivers' sidelobe response and 4) potential noise bursts interfering with the bottom echo detection. In general, the threshold level is computed to ride above the noise and above the sidelobe response. For reference, the noise level measured on data similar to that of Figure 1.3 is usually around 20 mv. The sidelobe threshold is computed as $1/4^{th}$ the amplitude (12 dB down) of the highest of the sixteen signals at any one time (Fig. 1.3). A noise burst appears as a synchronous ridge similar to the sidelobe ridge of Figure 1.3, but the amplitudes of the individual peaks are more or less constant on all beams (e.g. Fig. 1.7). By comparing the maximum amplitude with the median amplitude across all beams at any one time, the software is able to recognize a noise

burst. When a noise burst is detected, and when the corresponding threshold level is higher than both the noise and the sidelobe thresholds, the sixteen amplitudes are rejected. Otherwise the higher of the noise or the sidelobe thresholds will be used as the detection threshold. With this method however, canceling sidelobe response or noise bursts when they overlap with a bottom return results in cancellation of the corresponding part of the bottom return. Also, because of saturation in the EP receivers' amplifiers, sidelobe rejection is only partially achieved in cases when the specular return is clipped. This results in both echo detection and depth computation errors. Finally for each conversion cycle, a signal sample is detected if it is above the detection threshold and within the bottom-tracking gates.

Once the analog-to-digital conversion sequence has been completed on all beams the next set of echo processing operations is done once per transmission cycle. The signal level of each detected beam is integrated over the duration of the detected return (within the gates and above the threshold). If the resulting energy in the return is below a prescribed minimum, the beam is deemed invalid due to poor signal to noise ratio, [Farr, 1980]. For a valid beam, a slant range is calculated by computing the center of mass of all the detected signal samples for that beam, and by multiplying the corresponding arrival time by 750 m/s. Depth and cross-track horizontal distances are then calculated as described in Section I.3 of the text.

I.10. REFERENCES

Ballard, R. D. and T. H. vanAndel, Morphology and tectonics of the inner rift valley at lat. 36°50N on the Mid-Atlantic Ridge, *88, 507-530, 1977.*

Ballard, R. D. and J. Francheteau, Geologic processes of the mid-ocean ridge and their relation to sulfide deposition, in *Hydrothermal processes at sea floor spreading centers,* pp. 17-26, Plenum Press, New York, 1983.

Carter, D. J. T., *Echo-sounding correction tables,* Hydrographic Department Ministry of Defense, Taunton, 1980.

Clay, C. S. and H. Medwin, *Acoustical oceanography: Principles and applications,* p. 128, John Wiley and Sons, 1977.

Crane, K., Structure and tectonics of the Galapagos Inner Rift, 86 ° 10'W, *J. Geology, 86,* 715-730, 1978.

Crane, K. and R. D. Ballard, The Galapagos Rift at 86 ° W', Morphological waveforms, 4, structure and morphology of hydrothermal fields, *J. Geophys. Res., 85,* 1443-1454, 1980.

Crane, K., F. Aikman, R. Embley, S. Hammond, A. Malahoff, and J. Lupton, The distribution of geothermal fields on the Juan de Fuca Ridge, *J. Geophys. Res., 90,* 727-744, 1985.

Detrick, R. S., P. J. Fox, K. Kastens, W. B. F. Ryan, L. Mayer, J. Karson, and A Sea Beam survey of the Kane Fracture Zone and the adjacent Mid-Atlantic Ridge Rift Valley, *Trans. Am. Geophys. Union, 65,* 1006, 1984.

Dolph, C. L., A current distribution of broadside arrays which optimizes the relationship between beam width and side-lobe level, *Proc. Inst. Radio Engrs., 34,* 335-348, 1946.

Edwards, M. H., R. E. Arvidson, and E. A. Guiness, Digital image processing of Sea Beam bathymetric data for structural studies of seamounts near the East Pacific Rise, *J. Geophys. Res., 89,* 11108-11116, 1984.

Farr, H. K., Multibeam bathymetric sonar: Sea Beam and Hydrochart, *Marine Geodesy, 4,* 77-93, 1980.

Fornari, D. J., W. B. F. Ryan, and P. J. Fox, The evolution of craters and calderas on young seamounts: Insights from Sea MARC I and Sea Beam sonar surveys of a small seamount group near the axis of the East Pacific Rise at 10 ° N, *J. Geophys. Res., 89,* 11069-11084, 1984.

Francheteau, J. and R. D. Ballard, The East Pacific Rise near 21 ° N, 13 ° N and 20 ° S; inferences for along strike variability of axial processes, *Earth and Planetary Science Letters, 64,* 93-116, 1983.

Gallo, D. J., P. J. Fox, and J. A. Madsen, The morphotectonic signature of fast-slipping ridge-transform-ridge systems: A synthesis of Sea Beam bathymetry, *Trans. Am. Geophys. Union, 65,* 1103, 1984.

General Instrument Corporation, Sea Beam bathymetric survey system technical manual, volume 2, 1981.

Glenn, M. F., Introducing an operational multi-beam array sonar, *International Hydrographic Review, XLVII(1),* 35-39, Monaco, 1970.

Hey, R. N., M. C. Kleinrock, S. P. Miller, T. M. Atwater, and R. C. Searle, Sea Beam/Deep-Tow investigation of an active oceanic propagating rift system, *J. Geophys. Res. (in press),* 1985a.

Hey, R. N., D. F. Naar, M. C. Kleinrock, W. J. Phipps Morgan, E. Morales, and J. G. Schilling, Microplate tectonics along a superfast seafloor spreading system near Easter Island, *Nature (in press),* 1985b.

Kleinrock, M. C., R. N. Hey, and C. de Moustier, The 'Omega' deception in Sea Beam data, *Trans. Am. Geophys. Union, 65,* 1103, 1984.

Lewis, S. D., J. W. Ladd, T. R. Bruns, D. E. Hayes, and R. VonHuene, Growth patterns of submarine canyons and slope basins, Eastern Aleutian Trench, Alaska, *Trans. Am. Geophys. Union, 65,* 1104, 1984.

Lonsdale, P. F., Overlapping Rift Zones at the 5.5 ° S offset of the East Pacific Rise, *J. Geophys. Res., 88,* 9393-9406, 1983.

Macdonald, K. C. and P. J. Fox, Overlapping spreading centers: A new kind of accretion geometry on the East Pacific Rise, *Nature, 301,* 55-58, 1983.

Macdonald, K. C., J. C. Sempere, and P. J. Fox, East Pacific Rise from Siqueiros to Orozco fracture zones: along-strike continuity of axial neo-volcanic zone and structure and evolution of overlapping spreading centers, *J. Geophys. Res., 89,* 6049-6069, 1984.

Mammerickx, J., Morphology of propagating spreading centers: new and old, *J. Geophys. Res., 89,* 1817-1828, 1984.

McCool, J. M. and B. Widrow, Principles and applications of adaptive filters: A tutorial review, *NOSC, NUC TP 530,* 1977.

de Moustier, C., Inference of manganese nodule coverage from Sea Beam acoustic backscattering data, *Geophysics , 50,* 989-1001, 1985a.

de Moustier, C., Beyond Bathymetry, mapping acoustic backscattering from the deep sea floor with Sea Beam, *J. Acoust. Soc. Amer., submitted,* 1985b.

Naar, D. F. and R. N. Hey, Fast rift propagation along the East Pacific Rise near Easter Island, J. Geophys. Res. (in press), 1985.

Patterson, R. B., Relationships between acoustic backscatter and geological characteristics of the deep ocean floor, *J. Acoust. Soc. Am., 46,* 756-761, 1969.

Phillips, J. D. and A. S. Fleming, Multibeam sonar study of the MAR Rift Valley 36-37 ° N, *Geol. Soc. of Amer.,* 1978. Map Series MC-19.

Renard, V. and J. P. Allenou, SEA BEAM multi-beam echo-sounding in "Jean Charcot". Description, evaluation and first results, *International Hydrographic Review, LVI(1),* 35-67, Monaco, 1979.

Riblet, H. L. and C. L. Dolph, Discussion on a current distribution of broadside arrays which optimizes the relationship between beam width and side-lobe level, *Proc. Inst. Radio Engrs., 35,* 489-492, 1947.

Shipley, T. H. and G. F. Moore, Sediment accretion and subduction in the Middle America Trench, *OJI International Seminar on the formation of ocean margins,* 1985.

Smith, S. M., Sea Beam Operator Manual, SIO Reference 83-7, 1983.

Spiess, F. N. and P. F. Lonsdale, Deep-Tow rise crest exploration techniques, *Marine Tech. J., 16,* 67-75, 1982.

Spiess, F. N., R. Hessler, G. Wilson, M. Weydert, and P. Rude, Echo I cruise report, SIO Reference 84-3, 1984.

Tyce, R. C., Sea floor mapping aboard R/V CONRAD - The first year of Sea Beam, *Trans. Am. Geophys. Union, 65,* 1103, 1984.

Urick, R. J., *Principles of Underwater Sound, third edition,* McGraw-Hill Book Co., 1983.

vanAndel, Tj. H. and R. D. Ballard, The Galapagos Rift at 86 ° W: 2, volcanism structure and evolution of the Rift valley, *J. Geophys. Res., 84,* 5390-5406, 1979.

Chapter II

APPROACHES TO ACOUSTIC BACKSCATTERING MEASUREMENTS FROM THE DEEP SEAFLOOR.

II.1. ABSTRACT

Because the average ocean depth is four kilometers, seafloor investigations are mostly remote sensing operations. The primary means to determine the morphology, the structure, and the texture of the seafloor are acoustic. This paper considers the current seafloor remote sensing approaches involving acoustic backscattering. The physical constraints imposed by the ocean as a propagation medium, by the seafloor as a backscattering boundary, and by the measuring instruments are briefly reviewed. The sonar systems currently used by the oceanographic community for deep seafloor acoustic backscattering measurements deal with these constraints differently depending on their specific application and on whether they are towed behind a ship or mounted on her hull.

Towed sidescan systems such as Gloria II (U.K.), the Sea Mapping and Remote Characterization (Sea MARC) I and II, the Deep Tow system of the Marine Physical Laboratory (MPL), and hull-mounted systems such as Swathmap all give a qualitative measure of backscattering by converting echo amplitudes to gray levels to produce a sidescan image of the seafloor. A new approach is presented which uses a Sea Beam multibeam echo-sounder to produce similar sidescan-like images.

Quantitative measurements of backscattering have been attempted in recent experiments using the Deep Tow system and Sea Beam. Such measurements provide some insight into the geological processes responsible for the acoustic backscatter, with useful applications for geologists as well as designers and operators of bottom-interacting sonars.

II.2. INTRODUCTION

With an average depth of four kilometers, the ocean floor is only accessible by special purpose submersibles from which observations are limited by the aperture of a view port. For this reason, most seafloor investigations are remote sensing operations which use underwater sound as their primary tool and core or grab sample as well as bottom photography as ground truth. Seafloor acoustic measurements are commonly divided in two broad categories: low frequency (<100 Hz) seismic measurements in reflection or refraction work, and high frequency (>3 kHz) reflectivity or backscattering measurements. This paper focuses on the high frequency seafloor acoustic backscatter which is on one hand a noise background against which active sonars must operate, and on the other hand a source of information for geologists because its variations are caused by changes in bottom type or bottom microroughness.

The systems currently used by the oceanographic community to measure acoustic backscatter from the deep seafloor are most often sidescan sonars or echo-sounders, and occasionally specially designed multifrequency arrays. Sidescan sonars give a qualitative measure of backscattering by converting echo amplitudes to gray levels in the process of forming an acoustic image of the seafloor, and their resolution depends on a combination of parameters such as frequency, pulse length, beamwidth ... [Somers and Stubbs, 1984]. The same parameters apply to echo-sounders whose primary output is numerical bathymetry. However, broad-beam ($\geq 30^\circ$) echo-sounders have been used to obtain quantitative normal-incidence measurements in an effort to classify bottom types [Breslau, 1967] or bottom microroughness [Stanton, 1984]. Based on the author's work, this paper shows that multi-narrowbeam echo-sounders such as Sea Beam [Farr, 1980; Renard and Allenou, 1979] provide a means to obtain both quantitative seafloor acoustic backscattering measurements at discrete angles of incidence and qualitative measures in an acoustic imaging mode which is new to such

systems.

In the following, the physical constraints which condition the performance of sonar systems are reviewed briefly. The approaches taken in the design of several operational systems are compared, and recent experiments involving multifrequency arrays are presented.

II.3. SONAR DESIGN CONSTRAINTS

This section briefly reviews the constraints imposed by the ocean as a propagating medium, by the seafloor as a backscattering boundary and by the physical characteristics of the sonar on the design of systems to measure seafloor acoustic backscatter. More exhaustive treatments on the subject may be found in Urick [1983] and in Clay and Medwin [1977].

As sound waves propagate through the water column, they are attenuated due to spherical spreading and absorption. The former increases as the square of range and the latter increases roughly as the square of frequency. This frequency dependence is usually imbedded in a logarithmic absorption coefficient α in decibels per meter (e.g. $\alpha \sim 10^{-3}$ dB/m at 10 kHz) which sets limits on the operating frequency of a sonar for a given range. The deep-water ambient-noise level is also frequency dependent and decreases 5 to 6 dB per octave in the interval 1-100 kHz. At long ranges, attenuation dominates and adversely counterbalances improvements in ambient-noise characteristics obtained by using higher frequencies. Expressed in decibels, the attenuation terms add into a transmission loss :

$$TL = 20 log_{10} r + \alpha r \qquad (1)$$

where the slant range r is in meters. The propagation medium also imposes horizontal range limitations on sound waves as they are refracted due to variations in the sound velocity with temperature and pressure. In practice, the range limitation due to ray-

bending depends on water depth and bottom relief. At oceanic depths ($\geq$4 km) the maximum horizontal range attainable with a sonar at the sea surface is between 30 and 40 km [Andrews and Humphrey, 1980].

Bottom relief enters as a geometrical parameter in the range limitation, but for a given relief, bottom type and bottom microroughness condition the backscattering process. Whether a body backscatters sound effectively depends on how its density and compressibility differ from those of the surrounding ocean, and how its roughness scale compares to the acoustic wavelength. There is no simple theory to predict the level of seafloor-backscattered sound waves, and one relies on reported measurements (mostly done in shallow water [e.g. Wong and Chesterman, 1968; McKinney and Anderson, 1964]) and geoacoustic models [Hamilton, 1980] to derive empirical expressions for bottom backscattering strength as a function of grazing angle and/or frequency for various types of substrates.

In practice, the bottom backscattering strength BS, in decibels, is expressed as the sum of a backscattering strength per unit area ($1m^2$) S_B and an effective scattering area A :

$$BS = S_B + A \quad \text{with} \quad S_B = S_0 + 10log_{10}\sin^K\alpha \quad \text{and} \quad A = 10log_{10}(\frac{r\theta c\tau}{2\cos\alpha}) \qquad (2)$$

where as indicated in Figure 2.1, r is the slant range, θ the horizontal beamwidth of the transducer, α the grazing angle. τ is the transmitted pulse length, c=1500 m/s the sound speed, and S_0 is a scattering coefficient independent of grazing angle. For most sidescan sonar or echo-sounder applications, a square law dependence on $\sin\alpha$ ($K = 2$) is a reasonable match to existing shallow-water measurements and by extrapolation to the few measurements existing for the deep seafloor. The dependence of backscattering on bottom type is taken into account in the scattering coefficient S_0 which increases by nearly 25 dB from clay, through silt and sand to rock; and bottom roughness can cause variations of several dB in S_0 for the same bottom type.

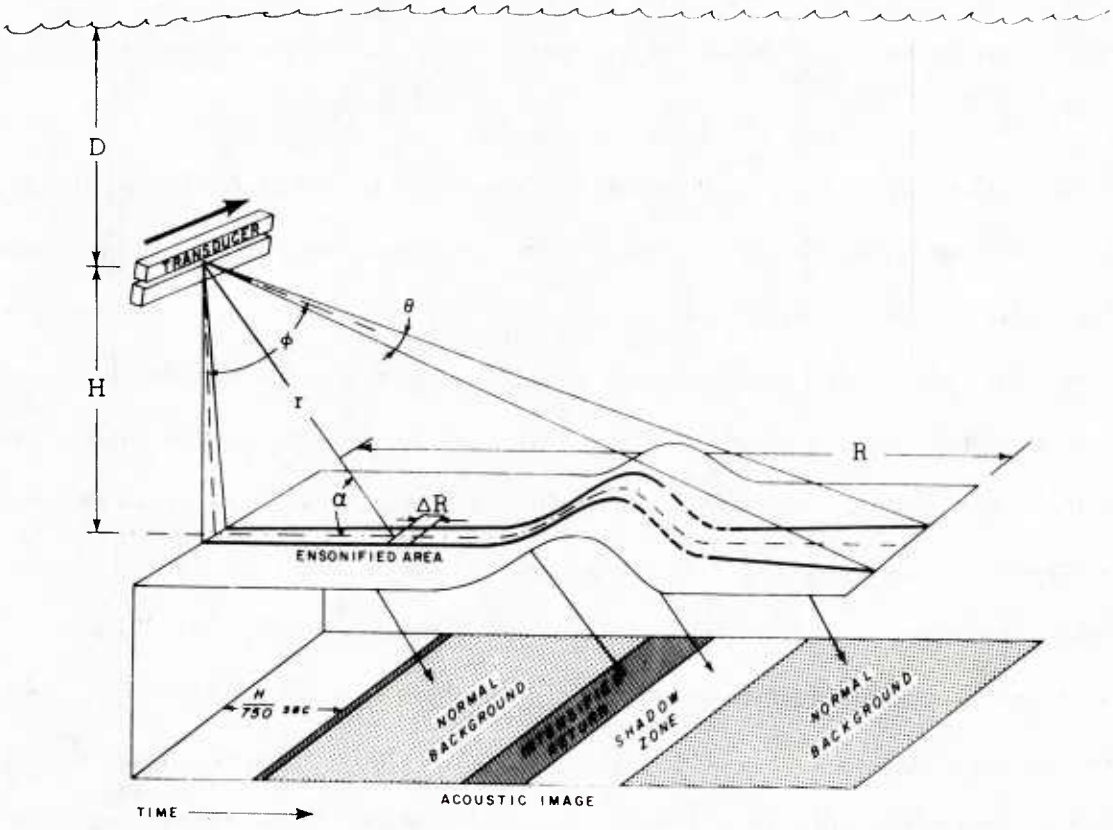

Figure 2.1 *Sidescan geometry.* A transducer array at depth D and elevation H above the seafloor has a beam pattern with angular dimensions θ (horizontal) and Φ (vertical). It ensonifies a strip of seafloor out to horizontal range R at right angle to the direction of travel (arrow). A portion of the strip (broken line) is not ensonified as it is shadowed by the hill. Backscattered acoustic intensities received at the transducer are converted to gray levels and mapped at increasing times of arrival (or slant range r). In this case, the first return is received H/750 sec. after transmission. On the acoustic image, specular returns appear darker than the normal background and shadow zones are white. ΔR is the cross-track resolution, and α is the grazing angle.

As mentioned above, the effects of bottom roughness depend on the operating characteristics of the sonar. To sample the small scale roughness rather than bottom slopes requires a system with narrow horizontal beamwidth and large bandwidth. These parameters are constrained by the physical characteristics of the transducer used.

The bandwidth capability of the transducer is usually limited to 10-15% of the center frequency [Kosalos, 1983]. Since the range resolution of a system with bandwidth w is $\Delta R = c/2w$, the incentive is to use high frequencies for greater bandwidth and higher range resolution, but attenuation imposes horizontal range limitations and it becomes necessary to operate close to the bottom. The most common and simplest way of achieving range resolution in sonars is to use short pulsed continuous wave signals (CW) but the shortest available pulse length τ is limited to $\tau = 1/w$. An alternative approach is to use long frequency-modulated (FM) pulses with $w\tau > 1$ and process the returns through matched filters. The advantages of this method are the possibility to use lower frequency and still maintain adequate range resolution, and a theoretical signal-to-noise power gain over short CW pulses with equal source level of $10log_{10}(w\tau)$ [Somers and Stubbs, 1984]. However implementation of the correlation processor adds complexity and cost to the overall sonar system design.

The beamwidth requirements are constrained by the size of the transducer array and by its operating frequency. Defining the beamwidth as the width of the mainlobe of the radiation pattern 3 dB down from its on-axis response, the beamwidth θ in radians is roughly the reciprocal of the number of wavelength across the effective aperture of the array i.e. $\theta = \lambda/L$ with $\lambda = c/f$. L is the length of the aperture in meters, λ is the acoustic wavelength in meters and f is the acoustic frequency in Hertz. Consequently, for a given frequency, the longer the array the narrower the beamwidth. However the optimum size of a transducer is a compromise between its directionality

and its acoustic-power output capability.

The maximum strain bearable by the transducer and cavitation limit the maximum power to which a transducer can be excited. These constraints set a lower limit on the size of the effective aperture necessary to keep the radiated power per unit area below the cavitation threshold. The power P per unit area necessary to produce cavitation increases as the square of the ambient pressure P_a: $P=P_a^2/2\rho c$ watts/cm^2 where ρc=1.5 $10^5 g\ cm^{-2}s^{-1}$ is the acoustic impedance of water [Albers, 1965]. A substantial gain in cavitation threshold is therefore achieved by operating an array a few decameters below the surface with the added advantage of reduced refraction effects as one goes below the thermocline. This technique is used in most shallow-towed sidescan arrays.

In the case of sidescan sonar arrays mounted on either side of a towed vehicle for port-starboard coverage, an additional constraint is imposed on the choice of operating frequency by the existence of mutual interference (cross-talk) between the arrays due to radiation of sound from the back of each array. As a result, a mirror image of returns on one side is mapped on the other side (for examples, see Belderson et al. [1972]). In general, this problem is alleviated by using slightly different operating frequencies on each side.

Finally, an estimate of the echo-to-noise ratio EN measurable with a given sonar system is obtained through the sonar equation which combines the various aforementioned design parameters. In decibel units, this equation has the form:

$$EN = SL - 2TL - (NL + 10log_{10}w) + BS + 20log_{10}b(\Phi) \qquad (3)$$

where SL is the source level, 2TL accounts for the round-trip transmission loss (Eq. 1) between the sonar and the bottom, $(NL+10log_{10}w)$ is the noise level in the bandwidth w, BS is the backscattering strength (Eq. 2) and $20\log_{10}b(\Phi)$ accounts for the transducer's vertical directivity.

For most sidescan systems the amplitude corresponding to the echo level is converted to a gray level and output on a linescan recorder to create an acoustic image of the seafloor surveyed. In the process, it is customary to multiply the amplitudes by a time varied gain to compensate for transmission losses and keep the returns within the dynamic range of the recording instrument.

II.4. CURRENT SYSTEMS

The design constraints outlined above are dealt with differently depending on the intended application of the sonar system. In this section, several systems currently used by the oceanographic community are compared on the basis of their design approach, and of the characteristics of the acoustic measurements obtained.

System		Gloria	Swathmap	Sea MARC II	Sea MARC I	Sea Beam	Deep Tow
Frequency (kHz)		P 6.5, S 6.7	3.5	P 11, S 12	P 27, S 30	12.158	110
		FM sweep	FM sweep	CW	CW	CW	CW
Pulse Length τ		2, 4 sec		.25-10 ms	.15-3.2 ms	7 ms	.2, .5 ms
Pulse rep. (sec)		20-40	40-48	1, 2, 4, 8, 16	.5, 1, 2 or 4	1-22	1
Bandwidth w		100 Hz		2 kHz→100 Hz	5 kHz→200 Hz	225 Hz	10 kHz
Beamwidth (deg.) θ, Φ		2.7 , 30		2 , 40	1.7 , 50	T 2.7 , 54 R 16(20 , 2.7)	.75 , 60
Cross-track resolution ΔR		20 m		5 m	.5 m		.15 m
Tow	depth D	30-60 m	hull mount	50-100 m	up to 6 km	hull mount	up to 7.5 km
	altitude H				12-1250 m		10-100 m
Horizontal range (km) R		15-30	up to 36	.5, 1, 2.5, 5	.25, .5, 1, 2.5	3/8 water depth	.5
Speed (knots)		up to 11	up to 20	up to 10	1-3	up to 15	1-2
Array	length (m)	5.33		3.8	1.5	T 2.8, R 2.8	1.25
	width (m)	.18		.2	.2	T .16, R .4	.08
Vehicle	length (m)	7.75		5.5	3		2
	width (m)	.8		1.3	1.2		.7

Table 2.1 Operational characteristics

Six systems covering a wide spectrum of ranges in deep-ocean work have been chosen for this comparison. They are the British system Gloria II [Somers et al, 1978; Laughton, 1981], Swathmap [Andrews and Humphrey, 1980a-b; Andrews et al, 1977], the Sea Mapping and Remote Characterization systems (Sea MARC I and II)

[Blackington et al, 1983; Hussong and Fryer, 1983; Kosalos and Chayes, 1983], Sea Beam and the Deep Tow instrument package [Spiess and Lonsdale, 1982; Spiess and Tyce, 1973]. The operating characteristics of these systems are listed in Table 2.1 where symbols appearing in Section II.3 and Figure 2.1 have been repeated for ease of correspondence.

Gloria II, Sea MARC I and II and Deep Tow are original sidescan sonar systems whereas Sea Beam is a multibeam echo-sounder and Swathmap is a sidescan application of the SQS-26 ASW sonar used aboard U.S. Navy frigates. The table is incomplete for Swathmap because some of the technical details of the system are classified. In the Swathmap design, a beam is steered to one side of the ship's track only with a maximum horizontal range of about 36 km and a cross-track resolution of several hundred meters. The high ship speed results in a poor along track resolution as transmit cycles are spaced 400 to 500 m apart at 20 knots ($\sim$10m/s). This system is primarily a reconnaissance tool designed to map at a rapid rate the large scale seafloor relief such as seamounts or fracture zones, and the intermediate relief (50-100m) typical of abyssal hills. Although the acoustic backscatter measured with Swathmap is modulated by bottom texture, it is dominated by slope effects, and the records are qualitative representations of bottom slopes and regional trends.

Similar measurements, with greater along and across-track resolution, are obtained with Gloria II which records acoustic backscattering from both sides of a shallow-towed vehicle. Different frequencies are used in the port and starboard arrays to avoid cross-talk between them. To enhance its signal to noise characteristics, this system uses a long transmit pulse and processes the echoes by match-filtering techniques. The records are automatically corrected from slant range to horizontal range by projecting slant range onto a horizontal plane at the mean depth below the vehicle [Searle, personal communication]. Measurements are qualitative and recorded acoustic

returns are usually dominated by bottom slopes with marginal indication of textural changes [Teleki et al., 1981]. The strength of this systems is its ability to map with sufficient detail large swaths of seafloor (30 km or more) at an average tow speed of 8 knots.

The Sea MARC II system is also a shallow-tow vehicle with port-starboard coverage and a tow-speed capability comparable to that of Gloria II. It operates at higher frequencies and uses short transmit pulses resulting in better cross-track resolution but reduced horizontal ranges (Table 2.1). In order to maintain even spacing between data points in the sidescan image, the bottom returns are sampled more rapidly at close ranges than at far ranges. As with Gloria II, the records are automatically corrected for slant range by assuming a flat plane at the mean depth below the vehicle. Due to its finer resolution, the qualitative bottom backscattering measurements obtained from Sea MARC II images are useful for bottom slope and texture determination on a scale of acoustic wavelengths ($\sim$12 cm), and for large scale regional trend determination. Sea MARC II uses a pair of transducer arrays (e.g. Fig. 2.1) on each side of the vehicle. By measuring the phase difference between the outputs of the two arrays, it is possible to determine the angle of arrival of a given return and therefore compute the corresponding depth and cross-track distance. In a post-processing operation, approximately one hundred such pairs of depths and cross-track distances are computed for every transmission cycle and used to produce a contour map of the swath of seafloor surveyed. This bathymetry is an important element in the interpretation of backscattering measurements made with the system, because it offers the potential to remove bottom slope effects from the data while in principle retaining the effects of bottom composition and microroughness.

The Sea MARC I system is a deep-towed version of Sea MARC II with a lesser swath width (5 km maximum). Its use of higher frequencies and short pulse

lengths yields sub-meter cross-track resolution; and its inherent slow speed over the bottom yields an along-track resolution between .5 and 5 m, depending on the pulse repetition rate (Table 2.1). Although this system uses the same transducer array pair configuration as Sea MARC II, the phase measurement technique is not implemented. Without numerical bathymetry, it is therefore not possible to correct the backscattering measurements for bottom slope. Nontheless, the fine resolution of the sonar allows detection of changes in bottom texture over areas of constant slope between 10 and 100 m in extent depending on the swath width chosen.

Through a combination of frequency, pulse length and tow speed, the sidescan sonars of the Deep Tow instrument package achieve the highest resolution of all the systems listed in Table 2.1. The lateral coverage to port and starboard is inherently limited to a swath about 1 km wide. This system is primarily intended for fine scale studies of the seafloor down to depths in excess of 7 km. The backscatter measurements are qualitative gray scale displays uncorrected for slant range. Changes in bottom texture are readily observable and micro-relief ($\leq$1 m) such as small fissures is resolvable on such displays. However, the limited coverage of the sonars make the system marginally useful for regional trend assessment as it requires long and costly surveys. The strength of the Deep Tow instrument package is its versatility as environmental (e.g. temperature, conductivity) and other geophysical (e.g. magnetics, subbottom profiles) data can be collected simultaneously with the sidescan data; and bottom photographs can be taken on the same lowering [Spiess and Lonsdale, 1982]. The phase measurement technique mentioned above is feasible but not implemented on the Deep Tow system.

II.5. NEW APPROACHES

The systems described in the previous section all operate as sidescan sonars. As such they provide qualitative acoustic backscattering measurements of the deep

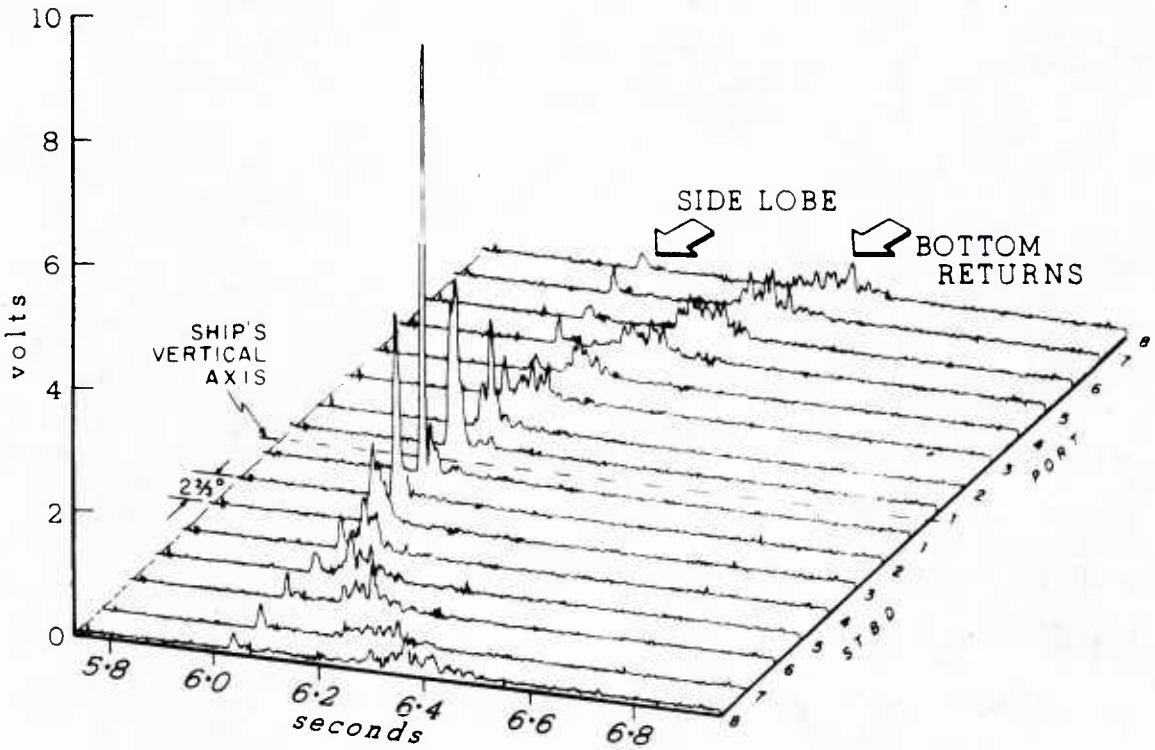

Figure 2.2 *Envelopes of echoes received by Sea Beam's 16 beams.*
Beams are equally spaced 2°2/3 apart within ±20° of the ship's vertical axis. In this display, returns are not compensated for ship's roll. Time is in seconds after transmission. Amplitudes have been corrected for transmission loss by a time-varied gain and are displayed in volts.

seafloor. This section looks at new measurement approaches using multibeam echo-sounders such as Sea Beam or experimental multifrequency acoustic arrays mounted on instrument packages such as Deep Tow [Spiess et al, 1984].

Sidescan sonars typically transmit and receive with the same fan-shaped beam which is narrow along track and broad across track (Figure 2.1). The Sea Beam system transmits with a similar geometry, but it receives with sixteen narrow beams spaced 2 2/3 degrees apart athwartships within ±20 degrees incidence. Each receive beam is 2 2/3 degree wide. With this geometry, the system is able to process back-scattered returns (Fig. 2.2) at discrete angles of incidence and calculate a set of depths and cross-track distances for each transmission cycle. This numerical bathymetry is then output in near real-time as a contoured chart of the swath of seafloor surveyed.

Sea Beam processes the acoustic signals to determine depths but has no internal provision for recording the actual waveform. To preserve these signals, requires a parallel acoustic data acquisition system which records digitally the echo envelopes on magnetic tape for later processing and analysis [de Moustier, 1985a]. A typical set of returns corresponding to one transmission cycle is illustrated in Figure 2.2. Such data make it possible to obtain quantitative backscattering measurements at discrete angles of incidence. Because variations in bottom characteristics cause fluctuations in the acoustic backscatter, and because numerical bathymetry allows corrections for slope effects to be made, the geological characteristics of the seafloor (e.g. microroughness or bottom type) can be inferred in part from these measurements [de Moustier, 1985b; Patterson, 1967].

In a new application of the Sea Beam system, the acoustic returns it receives are used in a sidescan-like mode by combining echoes on either side of vertical incidence. Working with digitally recorded Sea Beam acoustic data (Fig. 2.2), a peak detection process is used to obtain echo amplitudes at incremental slant ranges to

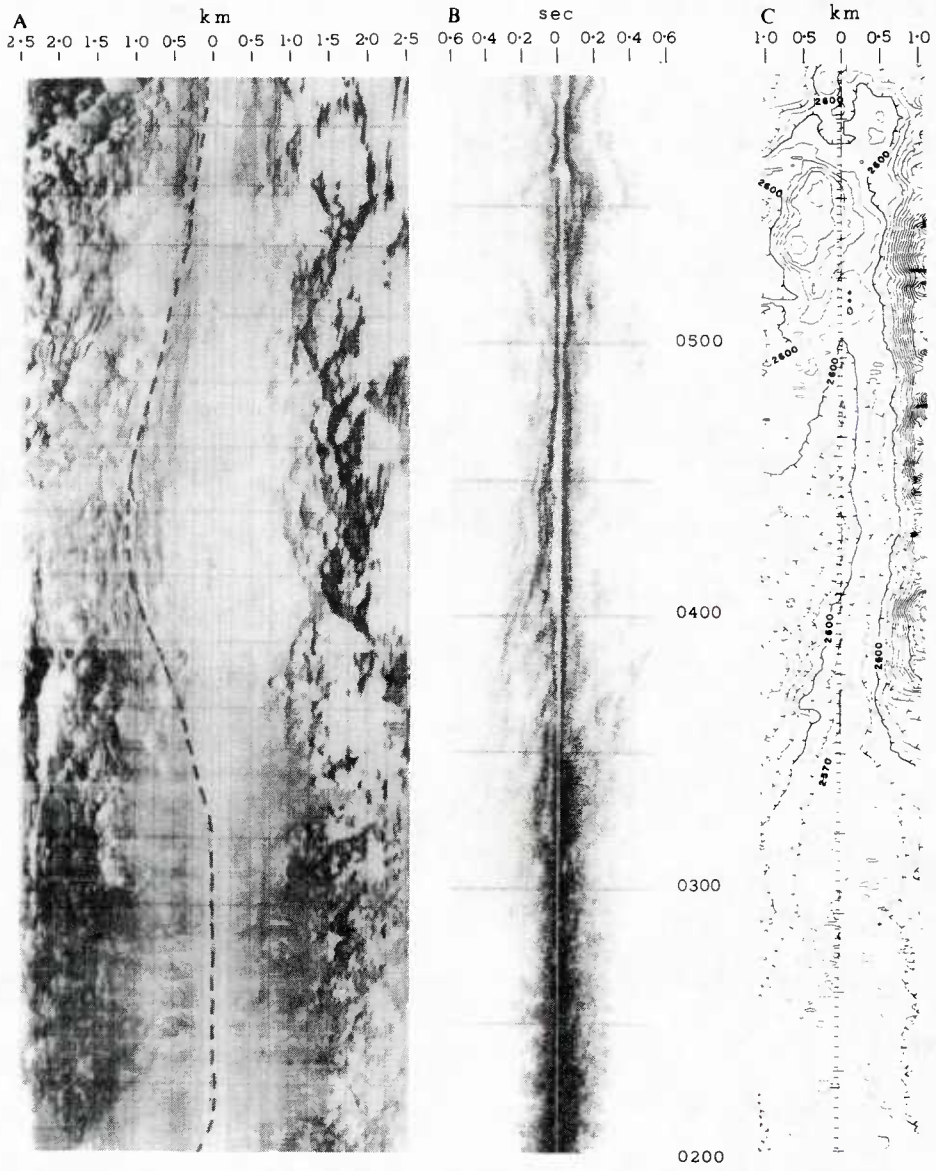

Figure 2.3 *Acoustic images and bathymetry.* (a) Slant-range corrected SeaMARC I image of the crest of the East Pacific rise at 10° N. Distances are true horizontal distances. (b) Uncorrected Sea Beam image of the same area; the dashed line in (a) represents the corresponding Sea Beam track. The cross-track dimension is in seconds from first arrival (differential slant range). (c) Corresponding swath of Sea Beam bathymetry at 10 m contour interval. Tick marks point downhill.

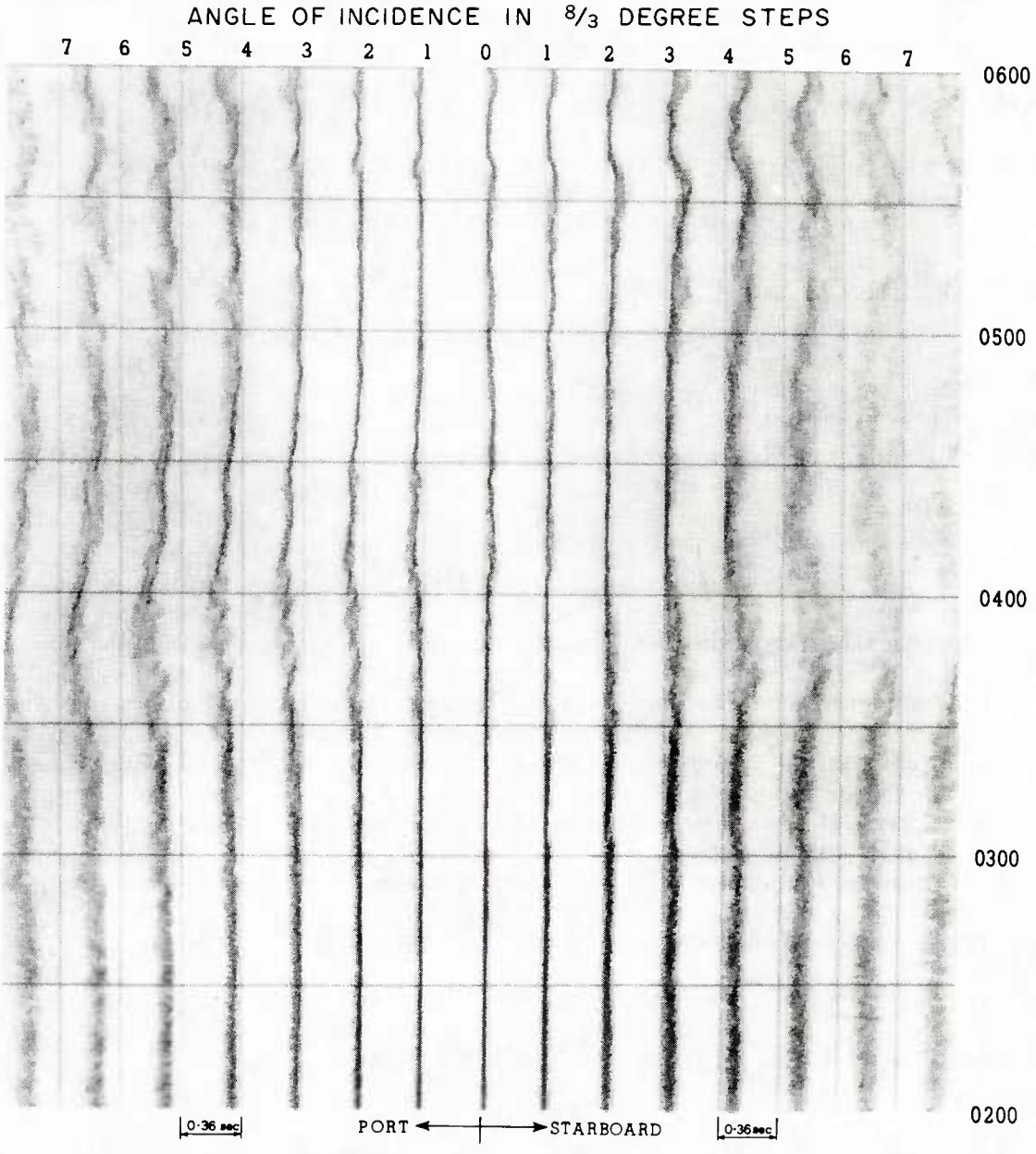

Figure 2.4 *Echo character of individual roll-compensated beams.* Same Sea Beam acoustic data as that of Figure 2.3. At each angle of incidence, vertical grid lines mark the time of first arrival for each transmission cycle, and echoes are displayed in bins .36 sec. wide. The gap between a grid line and the corresponding return is the differential slant range. Intensified returns (darker) observable beyond 10° incidence are indicative of slopping relief as sketched in Figure 2.1.

port and starboard. This process starts at the first arrival of each transmission cycle. An example of the resulting acoustic image is shown in Figure 2.3 along with the corresponding Sea Beam bathymetry, and a SeaMARC I image of the same region included for comparison. In this example, the Sea Beam acoustic image is not corrected for for slant range or for angle of incidence. However, as Sea Beam computes a cross-track bathymetric profile every transmission cycle, slant range corrections can be performed without the ambiguities inherent to the conventional horizontal plane method mentioned previously. The correction for angle of incidence entails applying a time-varying-gain to the signals displayed in order to compensate for the drop in backscatter as a function of angle. Such a correction is performed in most sidescan systems and yields an acoustic image having nearly uniform resolution out to the edges.

This new acoustic imaging application of Sea Beam gives textural information about the seafloor and brings out features not discernible in the contoured bathymetry. Unlike conventional sidescan images (Fig. 2.1), acoustic images obtained with Sea Beam do not contain shadows because angles of incidence are limited to the range $\pm$ 20 degrees, (note that most sidescan sonars do not record data in this angular sector). The qualitative measure of backscatter given by these images is therefore representative of seafloor microroughness and bottom slopes. The effect of bottom slopes can also be removed from the backscatter data given that quantitative slope information is available in Sea Beam's bathymetry.

The advantage of Sea Beam's discrete narrow beams can also be preserved by outputting the echo character on each beam in a gray level display such as that of Figure 2.4. Although this display is more difficult to interpret than conventional sidescan images, it gives bottom structural details which are smoothed out in the processing used to create the acoustic image of Figure 2.3b.

As mentioned in Section II.3, the effects of the seafloor as an acoustic backscattering boundary are difficult to predict, and one relies on measured data to derive empirical backscattering models usable by designers of sonar systems [Weinberg, 1981]. However, there is a definite need for deep seafloor measurements as the existing data base is very limited. Systems such as Sea Beam give access to quantitative measurements as a function of angle of incidence within the limits of the available beamwidth. Recent experiments to obtain quantitative measurements as a function of frequency have also been carried out using multifrequency arrays (4.5, 9, 15, 28, 60, 110, 160 kHz) mounted on the stern of the Deep Tow instrument package, and projecting fan beams pointing aft [Spiess et al.,1984].

In general single frequency measurements give non-unique answers about the nature of the seafloor because there is an infinite combination of roughness and bottom type influencing the backscattering process, and measurements need to be validated by direct bottom sampling or by bottom photographs or television. On the other hand, multiple frequency systems allow simultaneous sampling of several roughness scales thereby giving some indication of the respective contribution of roughness and bottom type in the backscattering process. Such measurements may eventually help geologists to acoustically differentiate between bottom types, or determine the size of bottom microrelief (e.g. furrows, manganese nodules, etc.). Similar multifrequency measurements have been obtained with conventional hull-mounted echo-sounders in an effort to determine the size of polymetallic nodules [Sumitomo Metal Mining Co., 1981].

II.6. CONCLUSIONS

In the remote sensing of the deep seafloor, acoustic backscattering can be measured with sidescan sonars or echo-sounders. Sidescan sonars usually provide qualitative measurements of backscattering which allow geologists to make regional

structural analysis and textural assessments of the seafloor, with a resolution depending on the operating characteristics of the sonar. A new application of the Sea Beam system in a sidescan mode has been shown to yield similar qualitative measurements whose usefulness is enhanced by the precision numerical bathymetry normally available with this system. The Sea Beam also offers the potential to obtain quantitative backscattering measurements as a function of angle of incidence. Because of the complicated nature of the seafloor backscattering process, these measurements do not give a unique answer about the nature of the seafloor, but they constitute a necessary step towards the understanding of the processes at work, and towards the construction of empirical formulas for sonar design purposes.

Further insight into the processes influencing the seafloor acoustic backscatter are obtainable with multifrequency arrays as they allow simultaneous sampling of several bottom roughness scales. However acoustic measurements alone may never be sufficient to give the exact nature of the seafloor, and ground truth from some other sensing technique (e.g. bottom sampling or photography) may still be necessary.

II.7. ACKNOWLEDGMENTS

For providing information and support material on the various systems described in this paper, I wish to thank R.C. Searle (Gloria II), J.G. Kosalos and J. Shaw (Sea MARC), J.E. Andrews (Swathmap) and W. Capell (Sea Beam). I am also grateful to R.M. Lawhead for providing a working system on which to plot the Sea Beam sidescan data, K. Crane and W.B.F. Ryan for SeaMARC I data samples, V.C. Anderson, F.V. Pavlicek and B. Sotirin for valuable suggestions, and J. Griffith for the art work. Support from the Office of Naval Research (Contract #N00014-79-C-0472) for the Sea Beam acoustic backscattering experiment is also gratefully acknowledged.

II.8. REFERENCES

Albers, V. M., *Underwater acoustics Handbook II,* The Pennsylvania State University Press, 1965.

Andrews, J. E., J. D. Graig, and W. A. Hardy, Investigations of the deep-sea floor by side-scan sonar techniques: central eastern Pacific, *Deep Sea Research, 24,* 975-985, 1977.

Andrews, J. E. and P. B. Humphrey, Swathmap: Long range sidescan sonar mapping of the deep seafloor, *Marine Geodesy, 4,* 141-159, 1980.

Andrews, J. E. and P. B. Humphrey, Circular structures observed in the deep sea by the Swathmap long-range side scan sonar, in *Bottom-Interacting Ocean Acoustics,* pp. 111-117, Plenum Publ. Co., New York, N.Y., 1980.

Belderson, R. H., N. H. Kenyon, A. H. Stride, and A. R. Stubbs, *Sonographs of the sea floor, A picture atlas,* Elsevier Publishing Co., 1972.

Blackinton, J. G., D. M. Hussong, and J. G. Kosalos, First results from a combination side-scan and seafloor mapping system (SEA MARC II), *Proc. Offshore Technology Conf. OTC 4478, 1,* 307-314, 1983.

Breslau, L., Classification of sea-floor sediments with a shipborne acoustical system, Woods Hole Ocean. Inst. Contribution No. 1678, 1967.

Clay, C. S. and H. Medwin, *Acoustical oceanography: principles and applications,* John Wiley and Sons, 1977.

Farr, H. K., Multibeam bathymetric sonar: Sea Beam and Hydrochart, *Marine Geodesy, 4,* 77-93, 1980.

Hamilton, E. L., Geoacoustic modeling of the sea floor, *J. Acoust. Soc. of Am., 68,* 1313-1340, 1980.

Hussong, D. M. and P. Fryer, Back-arc seamounts and the SEA MARC II seafloor mapping system, *Trans. Am. Geophys. Union, 64,* 627-632, 1983.

Kosalos, J. G. and D. N. Chayes, A portable system for ocean bottom imaging and charting, *Proc. Oceans '83,* 649-656, 1983.

Kosalos, J. G., Ocean bottom imaging, *OTC 4717, Proc. Offshore Technology Conf.,* 65-72, 1984.

Laughton, A. S., The first decade of Gloria, *Journ. Geol. Research, 86,* 11511-11534, 1981.

McKinney C. M. and C. D. Anderson, Measurements of backscattering of sound from the ocean bottom, *J. Acoust. Soc. Am., 36,* 158-163, 1964.

de Moustier, C., A Sea Beam acoustic data acquisition system, MPL TM-379, Scripps Inst. of Ocean. Ref. 85-, 1985a.

de Moustier, C., Inference of manganese nodule coverage from Sea Beam acoustic backscattering data, *Geophysics , 50,* 989-1001, 1985b.

Patterson, R. B., Relationships between acoustic backscatter and geological characteristics of the deep ocean floor, *J. Acoust. Soc. Am., 46,* 756-761, 1967.

Renard, V. and J. P. Allenou, Seabeam, multi-beam echo-sounding in "Jean Charcot". Description, evaluation and first results, *Internat'l Hydrogr. Rev. LVI(1),* 35-67, 1979.

Somers, M. L., R. M. Carson, J. A. Revie, R. H. Edge, B. J. Barrow, and A. G. Andrews, Gloria II, an improved long range sidescan sonar, *Oceanology International,* 16-24, BPS Exhibitions, Ltd., Technical Session J, London, 1978.

Somers, M. L. and A. R. Stubbs, Sidescan sonar, *IEE Proc, 131, Part F,* 243-256, 1984.

Spiess, F. N. and R. C. Tyce, Marine Physical Laboratory Deep Tow instrumentation system, Scripps Inst. of Ocean. Ref. 73-4, 1973.

Spiess, F. N., Ocean acoustic remote sensing of the sea floor, *Nat.Ocean. Atmos. Admin. Workshop on Ocean Acoustic Remote Sensing, II,* 11-1, 11-38, 1980.

Spiess, F. N. and P. F. Lonsdale, Deep Tow rise crest exploration techniques, *Marine Tech. Soc. Journal, 16,* 67-75, 1982.

Spiess, F. N., R. Hessler, G. Wilson, M. Weydert and P. Rude, Echo I Cruise Report, Scripps Inst. of Ocean. Ref. 84-3, pp. 22, 1984.

Sumitomo Metal Mining Co., Multi-frequency exploration system (MFES), *Techn. info. 24-8,* 4-Chome Shimbashi, Minato-ku, Tokyo, 1981.

Stanton, T. K., Sonar estimates of seafloor microroughness, *J. Acoust. Soc. Am., 75-3,* 809-818, 1984.

Rise Axis Tectonic Team, An along strike Sea Beam and Sea Marc I perspective of the axis of the East Pacific Rise: Implications for the accretion of oceanic lithosphere, *International Lithosphere Congress,* Texas A&M Univ., 1983.

Teleki, P. G., D. G. Roberts, P. S. Chavez, M. L. Somers, and D. C. Twichell, Sonar survey of the U.S. Atlantic Continental Slope; acoustic characteristics and image processing techniques, *Proc. Offshore Technology Conference, OTC 4017,* 93-102, 1981.

Urick, R. J., *Principles of underwater sound (3rd ed.),* McGraw-Hill, 1983.

Weinberg, H., Generic sonar model, Tech. document 5971-C, Naval Underwater Systems Center, 1981.

Wong H-K. and W. D. Chesterman, Bottom backscattering near grazing inicidence in shallow water, *J. Acoust. Soc. Am., 44,* 1713-1718, 1968.

Chapter III

GEOPHYSICS, VOL. 50, NO. 6 (JUNE 1985) P. 989–1001, 11 FIGS.

Inference of manganese nodule coverage from Sea Beam acoustic backscattering data

Christian de Moustier*

ABSTRACT

Normal incidence reflectivity from a manganese nodule field was measured with a 12 kHz Sea Beam multibeam echo-sounding system, aboard the R/V *Thomas Washington* and used to infer nodule coverage. A reflectivity map of the area was produced using the intensity of the specular return from each ping. The patchiness of the nodule coverage is evidenced by definite highs and lows in the reflectivity pattern. Ground truth was provided by near-bottom acoustic measurements and photographs taken with the Deep Tow instrument package of the Marine Physical Laboratory. Agreement between the simple nodule coverage predictions from Sea Beam acoustic data and the bottom photographs taken throughout the area is 98 percent. Although the Sea Beam system is limited in its dynamic range, this paper shows that it can be used very effectively to determine both topography and nodule coverage in potential mining areas.

INTRODUCTION

Economic considerations make the exploitation of ferromanganese nodules in the deep ocean strongly dependent upon extensive assessment of the density of nodule coverage at potential mining sites. Depending upon the method used to survey a site, the cost in ship time and manpower can become prohibitive. The approach described here derives its cost-effectiveness from the use of a Sea Beam echo-sounding system operating at optimum ship speed (10–12 knots). By taking advantage of the narrow-beam and multibeam capabilities of the Sea Beam, I was able to combine detailed topographic mapping with bottom backscattering characteristics to infer nodule coverage. The data presented here were gathered during two cruises in the northeastern tropical Pacific in May and June of 1983. The first cruise (PASCUA leg 5) was a rapid Sea Beam survey of an approximately 20 × 15 mile area southeast of Deep Ocean Mining Environmental Study (DOMES) site C (Figure 1), on an Ocean Mining Associates (OMA) trial mining site. This survey provided the topographic and acoustic reflectivity maps which served as the base of a month-long, fine-scale study of the same site, with the Deep Tow instrument package of the Marine Physical Laboratory of the Scripps Institution of Oceanography (Spiess and Tyce, 1973; Spiess and Lonsdale, 1982). The purpose of the Deep Tow survey (ECHO leg 1) was to assess, using a new multifrequency array, the near-bottom backscattering properties of a manganese nodule field. In addition, an environmental impact study of nodule mining was carried out through an extensive box coring program (Spiess et al., 1984). The choice of the site was motivated by the existence of a good DOMES and OMA data base in the general area.

This paper discusses the results of the Sea Beam acoustic study, and uses the Deep Tow data as ground truth.

BACKGROUND

Manganese nodules remote sensing

Most techniques used to prospect for manganese nodules on the deep ocean floor rely on acoustic remote sensing, near-bottom photography and/or television, bottom sampling, or a combination of these methods.

Two general approaches have been taken for acoustic remote sensing of nodules. The first is a single-frequency approach, using high-frequency (> 100 kHz) side-scan sonars on a deeply towed instrument (Spiess, 1980), or using a shipboard subbottom profiler to correlate the thickness of the transparent layer with nodule abundance (Piper et al., 1979; Mizuno and Moritani, 1976). The second is a multifrequency approach [Sumitomo Metal Mining Co. (MFES), Magnuson et al., 1981, 1982; Spiess et al., 1984] which uses the frequency dependence of sea-floor acoustic reflectivity to infer nodule sizes and abundance. Both approaches rely on the observation of a difference in acoustic backscatter between a sedimentary bottom laden with nodules and a bare one.

Near-bottom photography techniques range from the conventional deeply towed camera systems to the unmanned, deep diving, free vehicle Epaulard (Duranton et al., 1980; Galerne, 1983). Ground truth for remote sensing of manganese nodules is obtained through direct sampling of a nodule field. To this end, dredging is used where large amounts of nodules with little or no sediments are sought. On the other hand, box cores

Presented in part at the 106th meeting of the Acoustical Society of America in San Diego, November, 1983. Manuscript received by the Editor September 4, 1984; revised manuscript received December 12, 1984.
*Marine Physical Laboratory, Scripps Institution of Oceanography, University of California, San Diego, La Jolla, CA 92093.

provide an undisturbed sample of the bottom whenever an assessment of the geologic, biological, or acoustical properties of both the nodules and their underlying sediments is needed.

Normal incidence acoustic reflectivity

There is extensive literature dealing with acoustic properties of the ocean floor at various frequencies and angles of incidence, and with their geologic implications. Tyce (1976) and Parrot et al. (1980) gave good reviews of the literature available.

Due to its multibeam, narrow-beam characteristics, the Sea Beam system allows the measurement of the acoustic backscatter of the sea floor from each individual beam. An angular relationship of acoustic backscattering can then be derived. However, in this paper I take a first look at the data by selecting the beam nearest normal incidence and leave the others for later analysis.

Since the depth of this manganese nodule survey area is large (4 500 m on the average), the radius of curvature of the acoustic wavefronts reaching the bottom is much larger than Sea Beam's acoustic wavelength (12 cm), and the wavefronts can be considered nearly planar. Therefore, I use this approximation in the following development.

In general, the intensity of a plane acoustic wave is related to the acoustic pressure P by

$$I = \frac{\overline{P^2}}{\rho c}, \tag{1}$$

where ρ is the density of the medium and c the propagation velocity in this medium. The product ρc is called the characteristic acoustic impedance of the medium. The bar indicates that the pressure is averaged over some time (usually the integration time of the instrument) (Urick, 1983). If I_0 denotes the intensity of sound at unit distance from the source, the intensity of the normal incidence return I from the bottom at depth r is given by

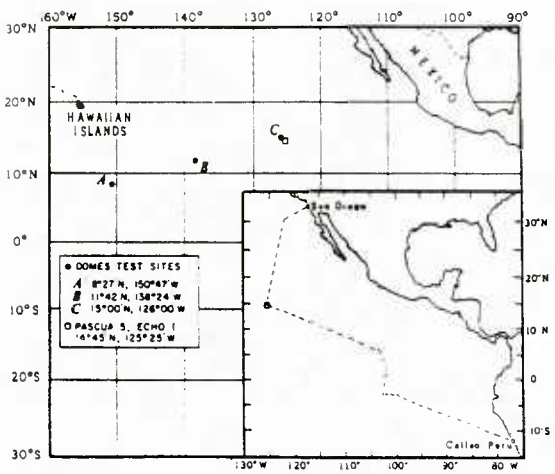

FIG. 1. Location of survey area. Deep Ocean Mining Environmental Studies (DOMES) sites A, B, C are shown by dots. Inset: track chart of the PASCUA expedition leg 5.

$$I = I_0 R^2 \frac{e^{-2\alpha r}}{(2r)^2}, \tag{2}$$

where α is the exponential attenuation coefficient and R is the Rayleigh reflection coefficient. Equation (2) assumes that the bottom reflects the sound rather than scatters it. This assumption seems reasonable for a manganese nodule field whose aggregate response was shown theoretically in Magnuson (1983) to be reflective rather than scattered.

For a plane wave normally incident on the boundary between two media of respective impedance $\rho_1 c_1$ and $\rho_2 c_2$, the Rayleigh reflection coefficient is the ratio of the reflected to the incident pressure waves:

$$R = \frac{\rho_2 c_2 - \rho_1 c_1}{\rho_2 c_2 + \rho_1 c_1}. \tag{3}$$

For the purpose, of this paper, medium 1 will be water and medium 2 will be sediment or nodules. The fraction on the right side of equation (2) indicates that sea water absorbs some of the energy, causing an exponential loss with distance from the source, and that intensity decreases proportionally to the square of distance due to geometric spreading. This is summarized in the sonar equation for an echo sounder obtained by taking $10 \log_{10}$ of both sides of equation (2):

$$EL = SL - BL - TL, \tag{4}$$

where

$EL = 10 \log_{10} I$ = echo level,

$SL = 10 \log_{10} I_0$ = source level,

$BL = -20 \log_{10} R$ = bottom loss,

and

$TL = 20 \log_{10}(2r) + 20\alpha r \log_{10} e$ = transmission loss.

Equation (4) was used to determine the reflection coefficients of various marine sediment types as a method of classification (Breslau, 1967). Likewise, Hamilton (1970a, b) did extensive work toward predicting in-situ acoustic and elastic properties of marine sediments. Tyce (1976) focused on the determination of the attenuation coefficient in ocean sediments with a 4 kHz near-bottom profiler. His data indicate a large variability in seafloor reflectivity over short horizontal distances due to changes in local bottom roughness and composition. Breaker and Winokur (1967) observed an increase in the magnitude of the echo level fluctuations with distance from the bottom. Considering that most of the acoustic reflection comes from the first Fresnel zone which increases in size with distance from the bottom, they attributed these fluctuations to changes in the reflective characteristics of the bottom over very short distances. Again, these changes are most likely due to variations in bottom substrate and or bottom roughness. The effect of roughness is to change the phase relationships between the different reflectors within a Fresnel zone. How rough a surface appears depends on the ratio of the root-mean-square (rms) bottom roughness σ to the acoustic wavelength λ (Clay and Medwin, 1977, chap. 10). Using the vertical component of wavenumber κ, one can distinguish three cases:

(1) $\kappa\sigma \ll 1$, the surface appears to be smooth and the amplitude of the backscattered return is determined by the reflection coefficient (coherent return);

(2) $\kappa\sigma > 1$, the surface appears to be rough and the returns are mostly incoherent;

(3) $\kappa\sigma \simeq 1$, intermediate range bridging the coherent and incoherent regimes.

Clay and Leong (1973) pointed out that when $\kappa\sigma \simeq 1$ and when the spatial dimensions of bottom roughness are much smaller than the diameter of the first Fresnel zone, the reflective components add as the sum of squares and the returned mean square signal is proportional to the number of reflectors in the ensonified area. This means that bottom loss depends also on the ensonified area and therefore on the beam width of the measuring system. The diameter of the first Fresnel zone is given by $d = (2\lambda h)^{1/2}$ where λ is the acoustic wavelength and h is the distance from the sonar to the reflection plane (Clay and Medwin, 1977, p. 50). For hull-mounted sonars such as Sea Beam, this distance is approximately the water depth. In this survey area Sea Beam's 12 cm wavelength yields a diameter of about 33 m for the first Fresnel zone at 4 500 m depth. As shown later, the rms roughness in this manganese nodule area is about 2 cm, so that $\kappa\sigma \simeq 1$, and the spatial dimensions of roughness (10 cm or less) are much smaller than the dimensions of the first Fresnel zone.

Other investigators have tried to correlate acoustic frequency dependence of bottom reflectivity with bottom type and/or bottom roughness (Mackenzie, 1960; Zhitkovskii et al., 1966). This turns out to be a difficult problem when the acoustic wavelength and/or the bottom are such that subbottom reflections can no longer be ignored. Note that when the bottom is assumed horizontally stratified with plane interfaces between layers, subbottom reflections from thin layers (Clay and Medwin, 1977, chap. 2) yield a closed-form solution. However, in order to perform a first-order analysis, simplifying assumptions considering the ocean bottom as locally homogeneous in depth are made. An ideal ocean bottom can then be defined where, for normal incidence, the dimensions of the bottom irregularities compared to the acoustic wavelength and the impedance mismatch at the water-sediment interface are the main parameters in the determination of bottom reflectivity. Higher reflectivity corresponds to a high impedance contrast between sea water and bottom (generally hard substrate) and a locally smooth relief (dimensions smaller than the acoustic wavelength). As the ratio of the size of the bottom irregularities to the acoustic wavelength increases, the bottom irregularities act as scatterers and the specular component of an echo is lower. Reflectivity is again lower when the impedance contrast is low (soft bottom with impedance similar to that of sea water).

A manganese nodule field consists of a soft bottom (sediments) on which a variable number of nodules lie. Nodule acoustic remote sensing is then possible, provided there is enough impedance contrast between nodules and sediments.

Although no values are presently available for the acoustic impedance of manganese nodules or surface sediments in the survey area, the values given in Hamilton (1970b) for sediments of the Pacific and in Magnuson et al. (1981) for nodules can be used to compute an expected acoustic reflectivity difference between nodules and their underlying sediments. The sediments are mostly pelagic silty clay (Spiess et al., 1984) for which Hamilton gave an in-situ reflective coefficient of 0.1316 at normal incidence and the corresponding bottom loss of 17.6 dB. For Pacific nodules, Magnuson gave a range of values for both nodule density and compressional wave speed. I use $\rho_2 =$ 1.95 g/cm^3, $c_2 = 2\,400$ m/s for a nodule, and from Urick (1983) $\rho_1 = 1.0475$ g/cm^3, $c_1 = 1\,520$ m/s for seawater at 4 500 m depth. Substituting these values in equation (3) yields a reflection coefficient $R = 0.4923$, which when expressed as the bottom loss term in equation (4) becomes $BL = 6.2$ dB. When the bottom depth is relatively constant, the transmission loss of equation (4) can be assumed constant. Therefore bottom loss is the only variable in equation (4), and the difference in reflectivity between a nodule and the underlying sediment is simply the difference in bottom loss: 11.4 dB.

Hamilton (1970b) also indicated there is little or no dependence of bottom loss with acoustic frequency for sediments where there is no lower layer to reflect sound which interferes with sea-floor reflections. Such is not the case for a nodule field. Studies by Magnuson et al. (1981, 1982) and the Sumitomo Metal Mining Co., where manganese nodules were modeled as spheres on an infinite flat plane, show that the bottom reflectivity of a nodule field can be expected to reach a maximum for a frequency corresponding to

$$ka = 1, \tag{5}$$

where k is the acoustic wavenumber and a is the mean nodule radius. By comparing the results from measurements at sea with the foregoing models, some clues arise as to the validity of the assumptions made. However, before I can discuss these results, I need to characterize the data base and the measuring systems, Sea Beam and Deep Tow, used in this survey.

SEA BEAM ACOUSTICS

The Sea Beam system uses a multibeam, narrow-beam echo sounder operating at a frequency of 12.158 kHz with a pulse length of 7 ms and an echo processor to generate, in near real time, contour maps of the ocean floor while the ship is under-

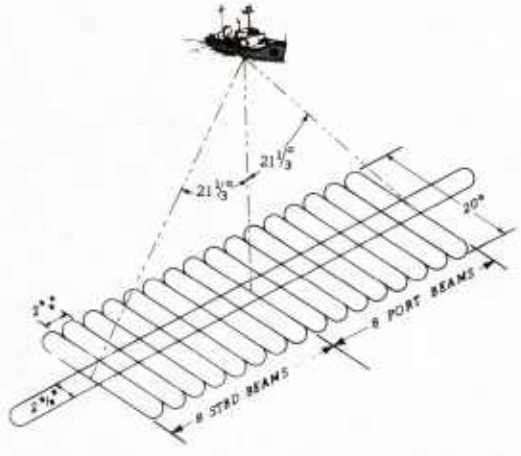

FIG. 2. Sea Beam geometry. The transmitted beam pattern ensonifies an area on the sea floor 2⅔ degrees in the fore-aft direction and 54 degrees athwartships, in a vertical plane from the ship. The receiving beam pattern appears on the sea floor as 16 rectangles, each 20 degrees fore-aft by 2⅔ degrees athwartships. The received acoustic energy therefore comes from the intersection of the two beam patterns which is delimited by 16 squares 2⅔ degrees on a side.

way. Figure 2 illustrates the Sea Beam transmit/receive geometry. The transmitted beam pattern spans 54 degrees athwartships by 2⅔ degrees in the fore-aft direction. It is pitch-stabilized to ensure vertical projection. As a result of the Sea Beam beam forming, the receiving beam pattern can be approximated by 16 adjacent rectangles 2 2/3 degrees by 20 degrees. The acoustic energy received at the ship comes from the intersection of the transmit and receive beam patterns, that is 16 "squares" 2 2/3 on a side.[1]

With contour mapping as a goal, the Sea Beam does not preserve all the acoustic information it receives. As a result some valuable information not necessary for depth determination, such as the amplitude and the shape of the echo signal, is lost.

In order to preserve the echo amplitude information, a parallel data acquisition system was built around an LSI 11/23 minicomputer (de Moustier, 1985). This allows digital recording on magnetic tape the 16 Sea Beam detected, nonroll-compensated beams, along with time-varied-gain (TVG) and ship roll information. The TVG is designed to compensate for transmission loss [attenuation and spreading terms in equation (2)] and has already been applied by the Sea Beam system when the data are recorded. Figure 3 shows a typical 16 beam return, not roll-compensated, where the envelopes of the detected acoustic signals are plotted in analog-to-digital (A/D) units versus time after transmission. These units correspond directly to sound pressure levels with TVG applied. In this instance, the sea floor is essentially flat, resulting in the parabola outlined by the 16 returns. The amplitude is highest in the near-specular direction (first arrival in time) and decreases rapidly from the center outward. The early, synchronous returns on the side beams represent side lobe energy from the specular return and are rejected in both depth and return amplitude processing.

The Sea Beam system has not been calibrated; therefore in the following all the measurements are presented as relative.

DATA

The data presented here were collected during a 40-hour Sea Beam survey and a subsequent Deep Tow near-bottom investigation. Although the Sea Beam system maps a swath of sea floor three-quarters of the ocean depth wide, a high degree of overlap between swaths (80 percent in places) was used to provide as much redundant acoustic data as possible. Figure 4 shows the topography of the survey area contoured from the Sea Beam data. The contours are at 20 m intervals, implying a relatively flat portion of sea floor with less than 200 m of total relief in 40 km. Aside from two north-south troughs which bottom out at 4 600 m on the edges of the map, the mean depth is 4 500 m.

The general pattern agrees well with the known north-south orientation of sea-floor features, perpendicular to the spreading direction in this part of the Pacific Ocean.

At this depth the Sea Beam system transmits every 8 s. For each transmission, a set of 16 returns (Figure 3) is digitized and recorded on magnetic tape. For a first look at these data, the postprocessing consisted in selecting the highest amplitude in each set. The highest amplitude generally represents the near-specular return, which in the case of a relatively flat bottom, as in this area, comes in first.

This set of peak amplitudes is then low-pass filtered by applying a running mean along the track, averaging over the

[1]For a detailed description of the system, see Renard and Allenou (1979).

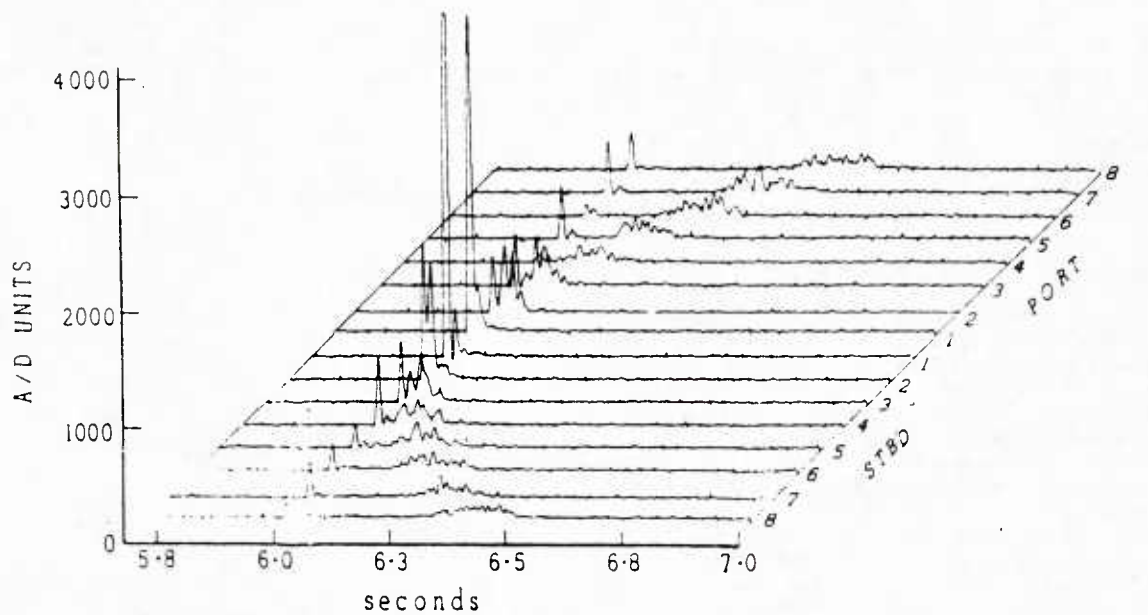

FIG. 3. Acoustic signal envelopes of the 16 performed beams at the output of the Sea Beam echo-processor receivers. The *x*-axis represents time after transmission in seconds. The *y*-axis represents the amplitude of the signals expressed in A/D units (0–4095) linear scale. Such data are recorded digitally on magnetic tape every transmission cycle, along with time-varied-gain and ship's roll. No roll correction has been applied to the data at this stage.

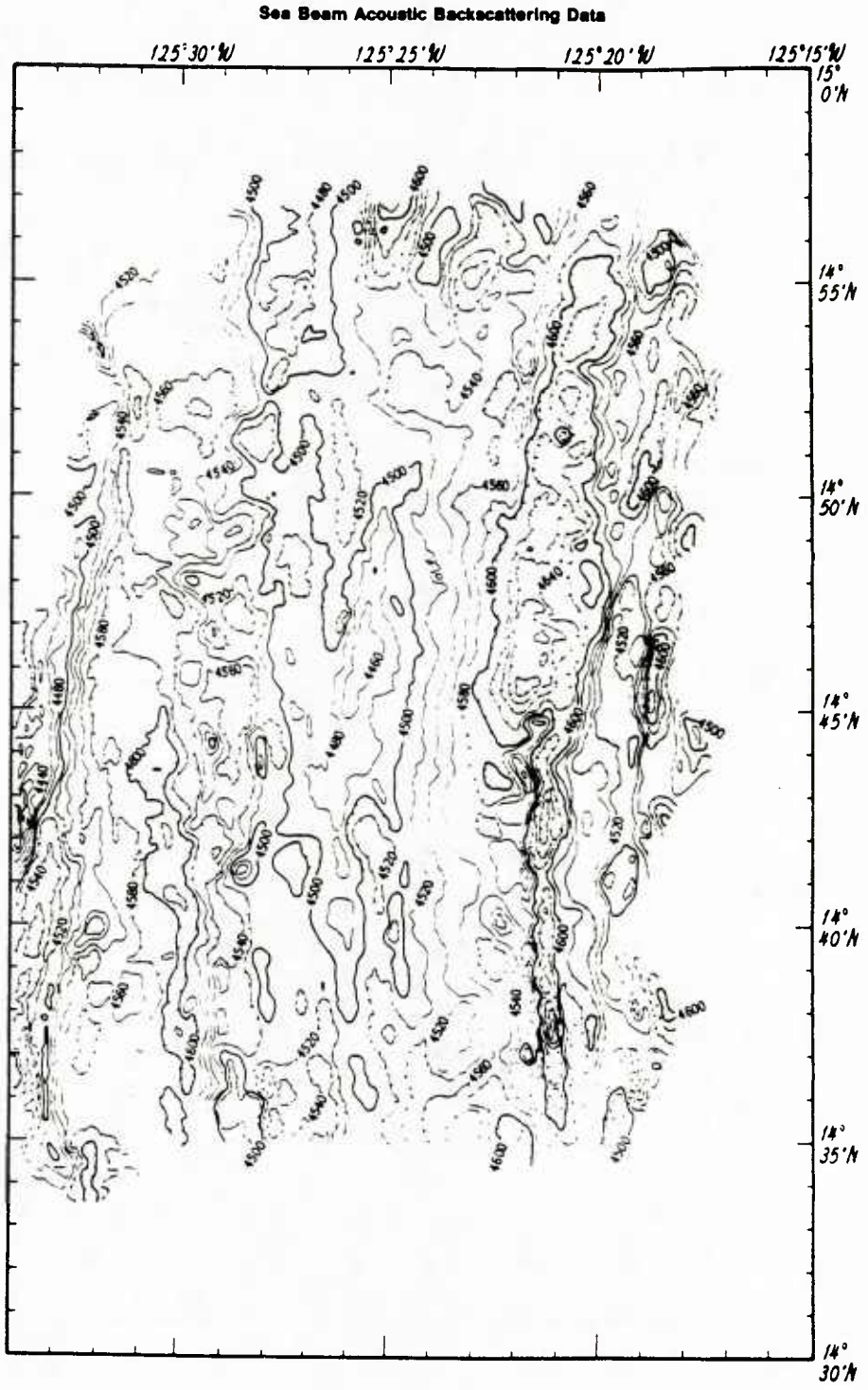

FIG. 4. Contoured map of the survey area from Sea Beam data. The contours are in uncorrected meters. The contour interval is 20 m.

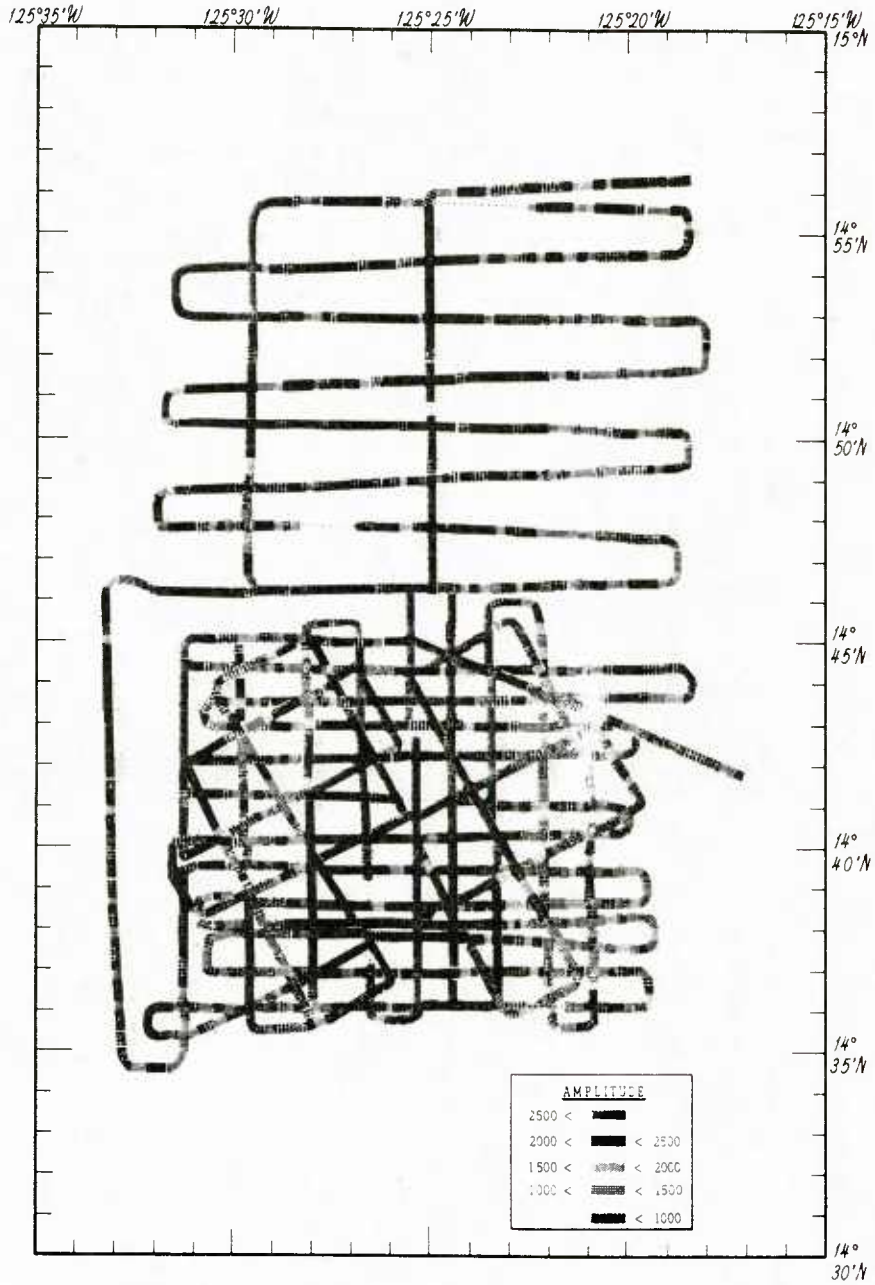

FIG. 5. Ship's track of the Sea Beam survey in the manganese nodule area (PASCUA leg 5). The peak amplitude from each ping (Figure 3) has been selected, low-pass filtered, and plotted along the track in A D units linear scale (0–4095). Five intervals were chosen on this scale and pattern coded as shown in the key.

size of the vertical beam's footprint: roughly five transmission cycles at 11 knots. The resulting data are plotted and pattern coded along the ship's track on Figure 5. The A/D units linear scale is the same as indicated in Figure 3.

The Deep Tow survey was concentrated in the southern portion of the area where the Sea Beam survey density is greatest. The Sea Beam acoustic data served as a reference for the Deep Tow work during which camera runs, near-bottom multifrequency (4.5, 9, 15, 30, 110, 160 kHz) backscattering measurements, and side-looking sonar data (110 kHz) were collected. As part of a mining environmental impact study, 16 box cores were also taken throughout the Deep Tow survey area. The various elements of the Deep Tow work are summarized in Figure 6 (Spiess et al., 1984).

DISCUSSION

Sea Beam reflectivity data

Inspection of the peak-amplitude data reveals a substantial ping-to-ping variability as well as definite mean amplitude highs and lows along the ship's track. This point is illustrated in Figure 7 where amplitude versus distance along the track is plotted in conjunction with the center beam width profile. The

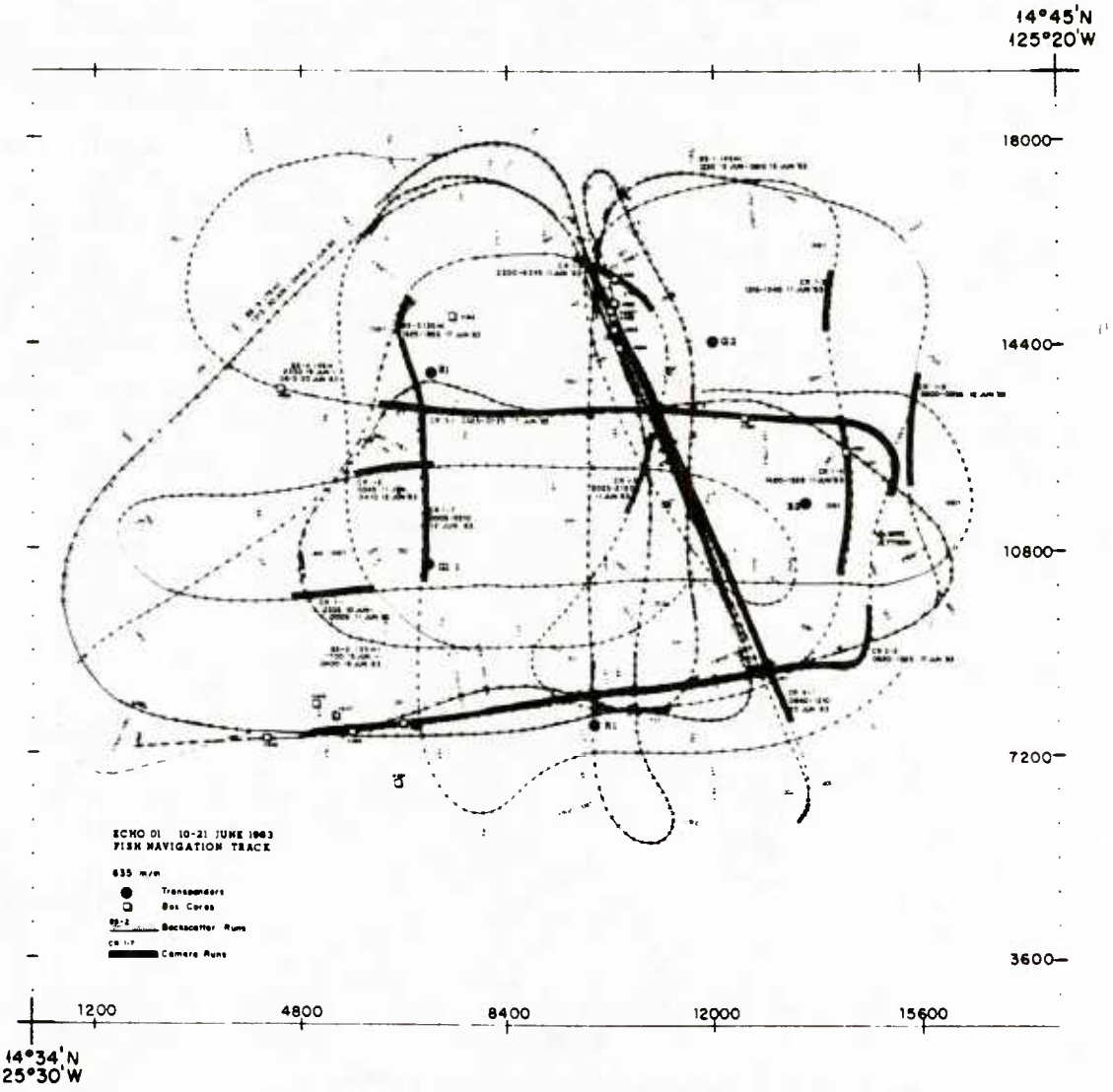

FIG. 6. Deep Tow track chart showing camera runs, near-bottom multifrequency backscattering measurement runs, box core locations, and navigation transponder positions. Coordinates are in meters east and north of 14°34'N, 125°30'W.

amplitude is expressed in relative decibels, with reference to the mean amplitude of the data displayed. The data shown in this figure have been averaged over five transmission cycles for clarity; actual ping-to-ping variability is much greater. Some small correlation with topography can be seen. However, remember that the vertical exaggeration on the depth profile is 18. The slopes are therefore rarely in excess of 2 degrees. On the left side of Figure 7, large fluctuations in amplitude are apparent, and the average value is around −6 dB. Compared with the right side where the average amplitude is +4 dB, the bottom reflectivity has changed significantly from one side to the other.

Following this result, I divided the peak amplitude data set into five intervals on the A/D linear scale (0–4 095) and pattern coded each one as shown in Figure 5. The data match, to within 130 A/D units on the average, over all except three track intersections where there are slight offsets. Because normal satellite navigation is simply inadequate for track positioning at the level of Sea Beam's resolution, one relies upon matching Sea Beam topography at crossings and overlaps for accurate track positioning. However, accurate adjustments are difficult to achieve when the sea floor surveyed exhibits little relief, as in this area.

A histogram of the data distribution is shown in Figure 8. The histogram suggests that the data suffer amplitude clipping at 3 000 A/D units, since there are no values beyond this point. This unfortunate characteristic is an artifact of the data acquisition system which was saturating at 7.3 V. This problem has since been corrected. In addition, it was found that the output of the Sea Beam echo processor receivers is limited to 8.5 V instead of the 10 V announced by the manufacturer. As a result, the receivers' dynamic range is apparently inadequate to accommodate both the low backscatter levels received on the side beams from a smooth bottom and the high amplitude associated with some strong specular returns. For this simplified application, however, the nodule distribution results are not significantly affected, since I arbitrarily chose to start the last A/D interval at 2 500 units. Nevertheless, this amplitude clipping does limit resolution for high-amplitude returns and prevents discussion of the abilities of such a sonar to characterize similar nodule fields or other seafloor types. From discussions with the Sea Beam manufacturer, it seems that a first-order improvement to this dynamic range limitation can be achieved by a simple modification of the detection amplifiers. Obtaining the full range needed, however, might require modification of the hydrophone preamplifiers which have been found to saturate occasionally and would also require use of logarithmic detection amplifiers.

Drawn from the data in Figure 5, a contour map of reflectivity in the southern portion of the survey area is presented in Figure 9. It uses the same pattern code as previously described. Two main characteristics stand out on this map: a region of strong reflectivity in the center, bordered to the east and to the west by strips of much lower reflectivity. Some of the low values correspond to the north-south troughs apparent in the bathymetry (Figure 4). However, the low reflectivity extends 3 to 4 km into the flat center portion. Changes in relative reflectivity of 12 dB or more (Figure 7) can therefore be expected as one crosses the leveled ground area in an east-west direction. Although this number is biased in trying to account for the clipping of the high-amplitude return (I added 2 dB to the 4 dB average amplitude shown on the right side of Figure 7), it is reassuring to note that it is close to the expected value computed in the "Background" section (11.4 dB). Since we were surveying a manganese nodule site, I would like to associate the above changes with differences in nodule coverage, with high-amplitude values corresponding to a dense coverage and low values indicating absence of nodules. To do so, however, re-

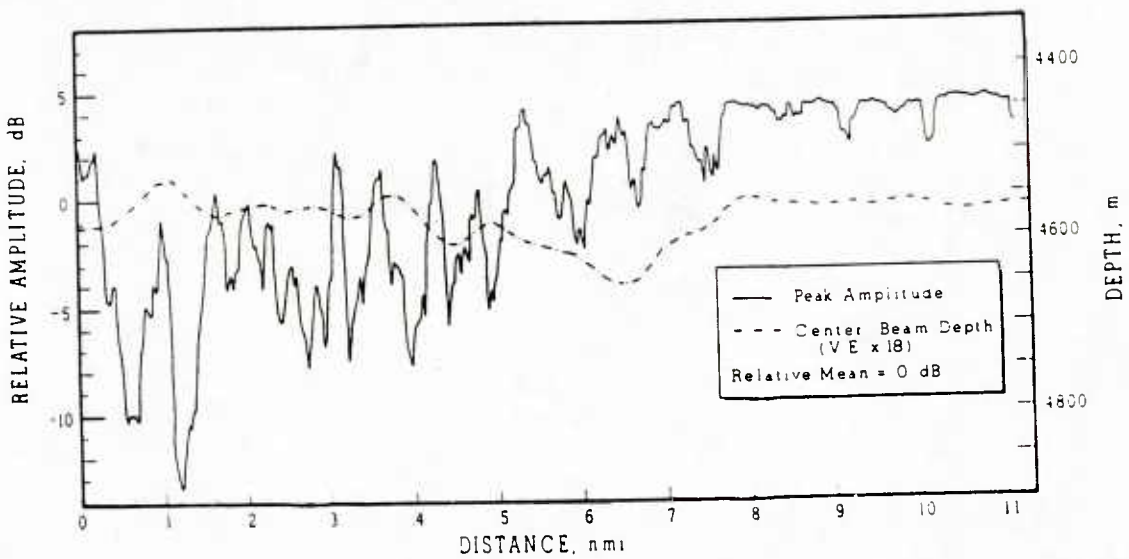

FIG. 7. The peak amplitude from each transmission cycle (Figure 3) is selected, low-pass filtered, and displayed as relative amplitude in decibels normalized by the mean of the portion of data shown. The mean is at 0 dB. The corresponding center beam depth profile is plotted with a vertical exaggeration of 18 to give an indication of slope along the ship's track. Depth is given in uncorrected meters and distance in nautical miles.

quires ground truth available only from near-bottom instruments with bottom photographic capabilities. Therefore, this Sea Beam reflectivity work was done in an area intended for Deep Tow coverage.

Deep Tow ground truth

It was a rewarding experience to watch Deep Tow camera runs unveil snapshots of the sea floor which matched the simple predicted bottom pattern. Each camera run (Figure 6) consistently output pictures which agreed with the simple manganese nodule coverage inferences made from the Sea Beam reflectivity data. Three representative pictures are shown on Figure 10. Each picture typifies an amplitude interval. The dense nodule coverage of photo A corresponds to the dot patterned areas on Figure 9 (2 500 A/D units and greater). The intermediate nodule coverage seen in photo B is found in areas with the brick pattern (2 000–2 500 A/D units) and the hatched pattern (2 000–1 500 A/D units). The two remaining patterns (1 500 A/D units or lower) turned out to be bare mud as shown on photo C. Inspection of over 3 000 Deep Tow bottom photographs and classification according to the three types shown (dense, intermediate, and bare) yielded a 98 percent correlation with the simple nodule coverage made from the Sea Beam data.

During a camera run, the towed instrument is flown approximately 10 m above the bottom. This renders pictures which cover about 35 m^2 of sea floor, thus giving a clue to nodule sizes. From the photographs and from the 1/4 m^2 box cores (photo D), the average nodule was found to be 4 to 8 cm in diameter, with a flattened and irregular cauliflower-like shape, as opposed to the rounder nodules found in other areas (Heezen and Hollister, 1971; Bischoff and Piper, 1979).

The first results from the Deep Tow multifrequency, near-bottom acoustic backscattering measurements (Spiess et al., 1984) also reinforce the belief that Sea Beam is well suited to map out manganese nodule coverage in this prospective mining area. Figure 11 shows the normal-incidence reflectivity difference between a densely nodule-covered patch and a barren one, as measured at the six frequencies of the Deep Tow backscatter system. The optimum frequency for this site appears to be between 15 kHz (16 dB) and 9 kHz (13 dB). The operating frequency of the Sea Beam system (12 kHz) falls exactly halfway between these two frequencies. At 12 kHz equation (5) yields a mean nodule radius of 2 cm (1.6 cm at 15 kHz). Although the nodules of this site are poorly approximated by spheres, the foregoing results indicate that the Sea Beam frequency is near optimum for the area surveyed. However, do not presume that 12 kHz will be optimum for all types of nodules, or that any 12 kHz sonar would provide the same results, since Sea Beam is a roll- and pitch-stabilized system with $2\frac{2}{3}$ degree resolution. As pointed out earlier, this high resolution has a significant effect on observed backscattered levels and associated fluctuations due to the size of the observed area. In comparison, normal echo sounders typically have a beam width between 30 and 60 degrees and a bandwidth wider than Sea Beam's, resulting in a substantially lower signal-to-noise ratio. Both the Deep Tow and the Sea Beam data point to the patchiness of the nodule coverage, some patches being less than a kilometer in extent. It is doubtful whether an unstabilized system which spans an area 2.4 km wide (30-degree beam at 4 500 m) can resolve such patches.

Note that the value obtained for mud-to-nodule reflectivity difference with Sea Beam is lower than those obtained with Deep Tow at 9 and 15 kHz. Even though the frequency dependence of mud-to-nodule reflectivity might not be linear, it is reasonable to expect the value at 12 kHz to be between those at 9 and 15 kHz. To explain this discrepancy, the differences in the geometry of measurement between the two systems should be considered. Indeed, for Sea Beam the area of the first Fresnel zone is approximately 33 m wide at 4 500 m depth, which is almost one order of magnitude larger than the diameter of the first Fresnel zone (4 m at 15 kHz) observed with Deep Tow when the instrument is 80 m off the bottom. However, the Deep Tow acoustic data have been averaged over spatial distances along track commensurate with Sea Beam's normal incidence footprint. Moreover, the beam width dependence presumably cancels out when the reflectivity difference between nodule and mud is measured with the same instrument. In the reflective model the geometric argument is then ruled out. To account for the Sea Beam's mud-to-nodule reflectivity difference being lower than those of the two neighboring Deep Tow frequencies (9, 15 kHz), I therefore need to reconsider the reflectivity model. In this manganese nodule area, the local roughness over a 200 m horizontal extent is primarily due to the presence or absence of nodules. From the bottom photographs and core samples, I estimate the rms roughness to be about 2 cm and spatial dimensions of roughness to be 10 cm or less. At 9 and 15 kHz, 80 m off the bottom, the diameter of the first Fresnel zone (5.2 and 4 m, respectively) is then still substantially larger than the spatial dimensions of the bottom roughness and $k\sigma = 0.75$ and 1.25, respectively. As mentioned in the "Background" section, $k\sigma \cong 1$ corresponds to the ill-defined boundary between reflection and scattering.

If I now take the difference between the mud-to-nodule reflectivity difference (16 dB) measured at 15 kHz and the computed bottom loss for the mud (17.6 dB), I obtain a bottom loss for nodules of 1.6 dB. In comparison, a smooth layer of chert (a

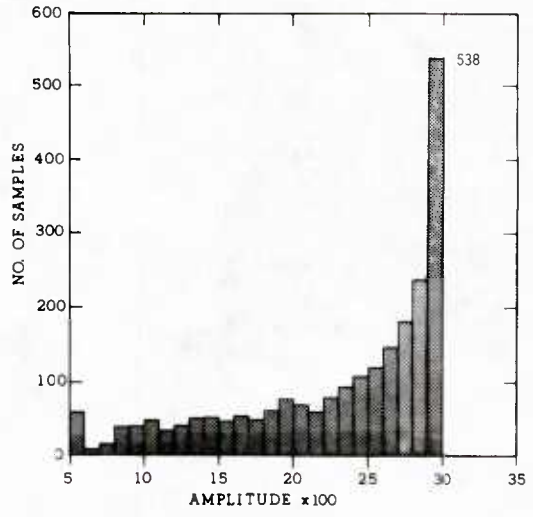

FIG. 8. Histogram of peak amplitude data distribution from the data shown in Figure 5. 20 percent of the values fall in the 2 900–3 000 A/D units range due to saturation in the data acquisition system.

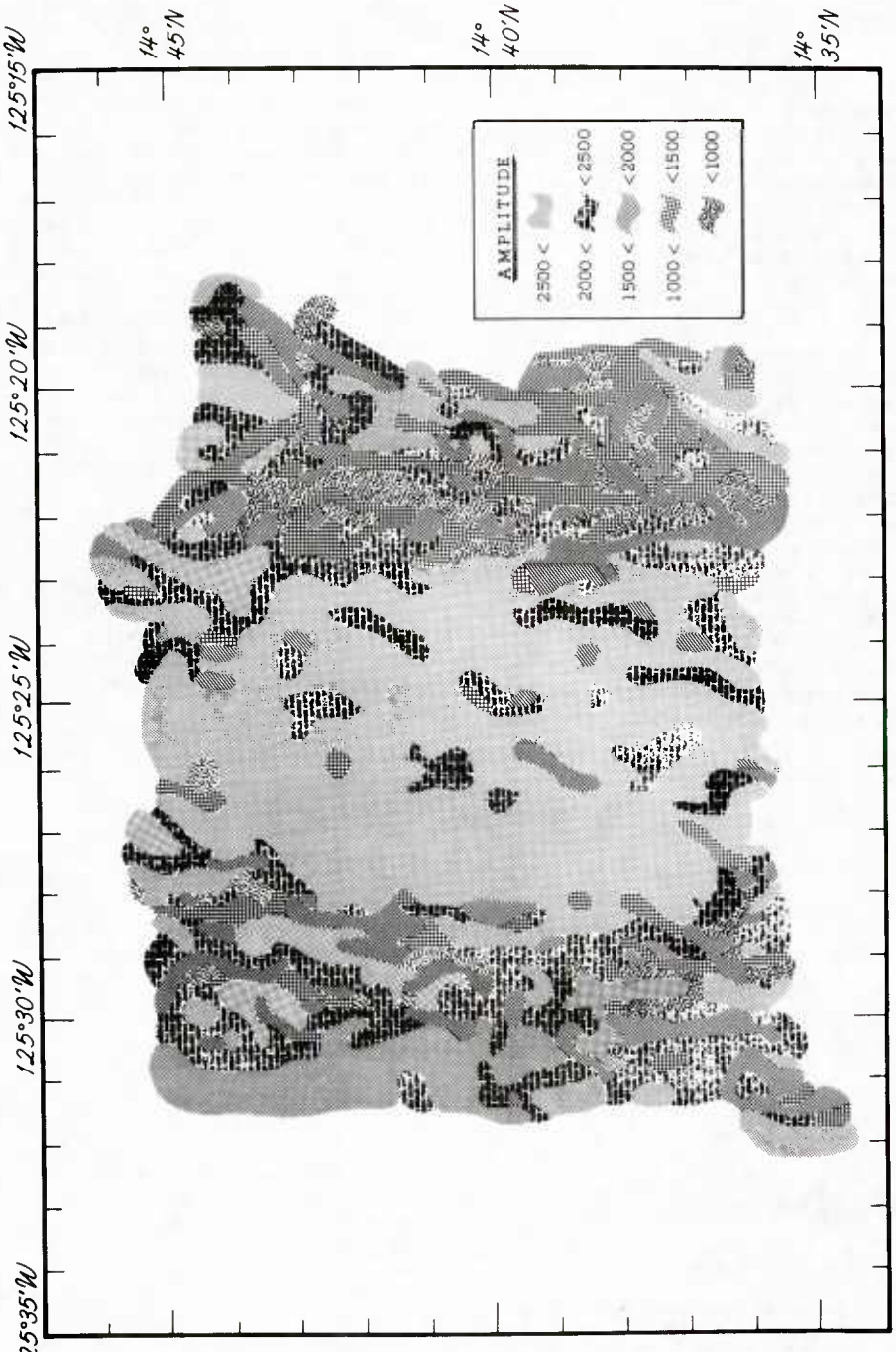

FIG. 9. Contour map of relative reflectivity drawn from the lower half of Figure 5, where ship track density is greatest. Same pattern code as in Figure 5. The dotted line delimits the Deep Tow survey area shown in Figure 6.

sedimentary rock having an acoustic impedance almost 4 times greater than the estimated impedance of a nodule) has a bottom loss of 3 dB (Tyce et al., 1980). The estimate of the mud bottom loss is perhaps questionable. However, it is reasonable to believe that this value is within 2 dB of the real one. Moreover, the nodules are porous and do not form a continuous slab, but rather are scattered at variable distances from each other. Therefore the bottom loss of such an assemblage is expected to be greater than the 3 dB given for a chert layer. Clearly, a simple reflective model is insufficient to explain the high value found at 15 kHz.

A more realistic result is obtained by considering the nodules as a thin layer separating water from mud. In this case, the reflection coefficient at normal incidence (Clay and Medwin, 1977, chap. 2) is given by

$$R = \frac{R_1^2 + R_2^2 + 2R_1R_2\cos(\phi)}{1 + (R_1R_2)^2 + 2R_1R_2\cos(\phi)}; \qquad \phi = \frac{4\pi f h}{C_{nod}}, \tag{6}$$

where R_1 is the water-nodule reflection coefficient [as given by equation (3)], R_2 is the nodule-mud reflection coefficient, f is the acoustic frequency, h is the thickness of the thin layer, C_{nod} is the compressional wave speed in nodules. Using $\rho = 1.37$ g/cm^3 and $C = 1\,507$ m/s for mud (Hamilton, 1970b), $h = 4$ cm for the thickness of the thin layer, and the values given in the "Background" section for the other parameters, yields a bottom loss of 3.3 dB at 15 kHz. Also with these values, the reflection coefficient R of equation (6) reaches a maximum at 15 kHz. Therefore, this thin-layer model agrees with the frequency dependence shown in the Deep Tow data (Figure 11), but does not match the mud-to-nodule reflectivity difference measured at 15 kHz, especially since (as mentioned above) the nodules do not form a continuous slab. A scattering model should then be considered for nodules. However, it requires knowledge of the ensonified areas and therefore of the beam patterns of the Deep Tow backscattering assembly. These beam patterns were not available at the time of this writing, precluding this analysis.

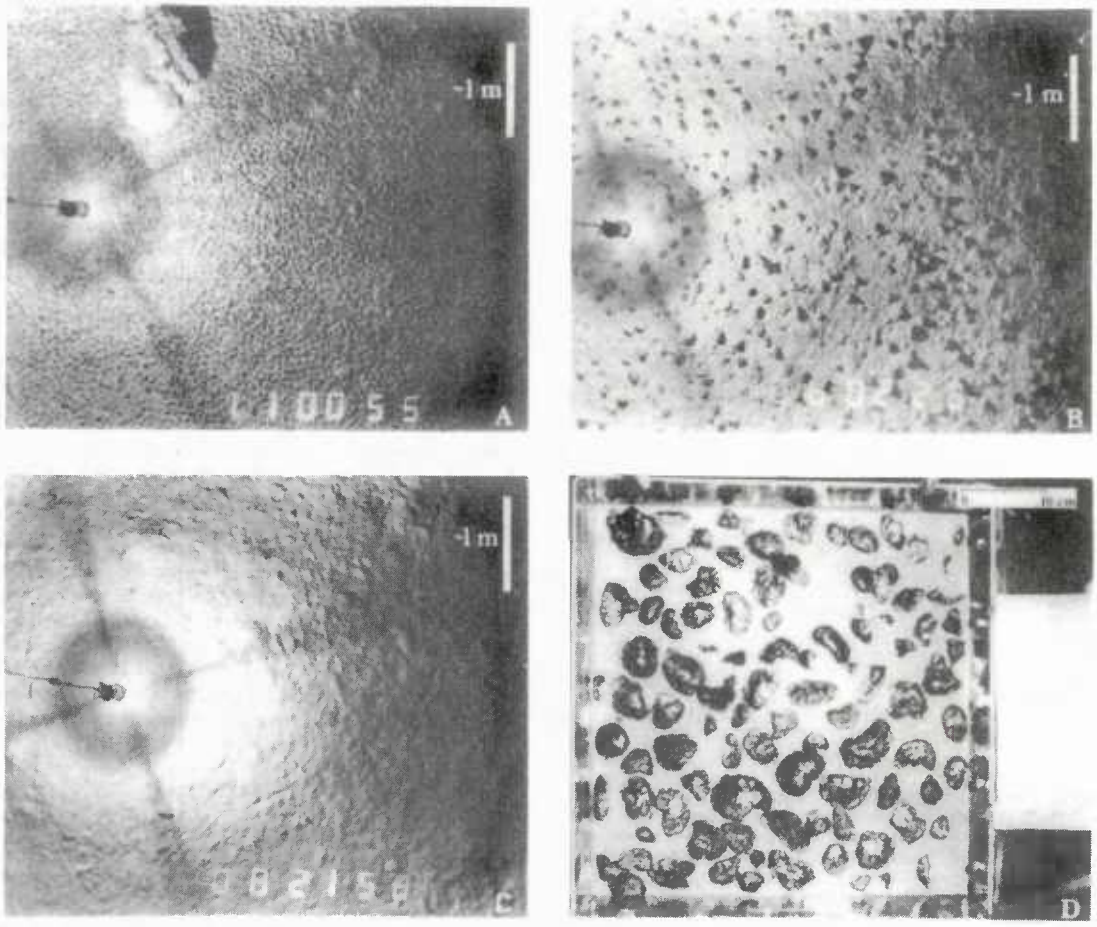

FIG. 10. Photographic ground truth: (a) dense nodule coverage representative of the dot patterned areas in Figure 9; (b) intermediate coverage representative of the brick and hatched patterns; (c) bare mud representative of peak amplitude values 1 500 A/D units and lower; (d) 1/4 m^2 box core number 358 (Figure 6) giving clues to representative nodule sizes for the area.

Further analysis of the data presented here, on a scattering rather than a reflective basis, and investigation of the angular dependence of acoustic backscattering from the Sea Beam and the Deep Tow data should help explain the processes at work here.

Further use of Sea Beam's acoustic returns

Using only the peak amplitude of the specular return of the 16 Sea Beam preformed beams to map out normal incidence bottom reflectivity is a nice first-order application. It yields good results over this particular manganese nodule field. Clearly, more can be expected from the Sea Beam acoustic data. Work is currently in progress to model the angular dependence of Sea Beam acoustic backscatter over various types of sea floor and to relate the data to the geologic characteristics of the bottom (Patterson, 1967). Following work done by Clay and Leong (1973) and recently by Stanton (1984) the variations in the shape of the echo envelope can also be used to predict bottom roughness. According to Stanton, his statistical analysis works best for amplitudes of sea floor roughness less than a quarter of the acoustic wavelength.

Since the Sea Beam acoustic wavelength is about 12 cm and since I estimated the local rms bottom roughness to be about 2 cm, the data from this manganese nodule area qualify for such a statistical analysis which could prove useful for discrimination between various bottom substrates with similar reflectivity patterns.

CONCLUSIONS

In a recent monograph on polymetallic nodules (Rapport de l'Académie des Sciences, Paris, 1984) the Sea Beam system was deemed an essential tool for any large-scale nodule prospection since detailed knowledge of the bathymetry is a prerequisite to nodule mining.

The data presented here bring a new dimension to the Sea Beam multibeam echo-sounding system. In addition to contour mapping, I have shown that it is possible to detect changes in reflectivity along the track by using the amplitude of the near-specular acoustic return. This works particularly well over a manganese nodule field with little relief, since nodules and mud provide a definite acoustic contrast (11 dB or more). Although a scattering model would seem more appropriate than the simple reflective one used here, the normal-incidence backscattering data gathered with the Deep Tow multifrequency acoustic array confirm that high reflectivity contrast between nodules and mud should be expected at Sea Beam operating frequency (12 kHz). This frequency seems to be near optimum for this manganese nodule site. Bottom photographs taken throughout the site agree surprisingly well with the simple nodule coverage prediction made from Sea Beam acoustic data.

In spite of dynamic range limitations evidenced in my data, I believe that nodule coverage assessment can be performed very effectively with a Sea Beam system while contour mapping the topography of a prospective mining site. In essence, areas where amplitude saturation occurred correspond to areas of denser nodule coverage with strong reflectivity. Photographic ground truth can be obtained with an unmanned, deep-diving free vehicle, with towed vehicle camera and sonar systems, or even with conventional bottom cameras.

More extensive processing of Sea Beam's detected echoes is in progress with the intent of assessing whether the backscattered returns separated by Sea Beam's high angular resolution can be correlated with seafloor geologic characteristics. This includes identification of the reflectivity and roughness characteristics of different bottom types: sediments, rocks, rock outcrops, manganese nodules, etc. Initial results have been very encouraging, as suggested both in this paper and in ongoing work on various types of sea floor.

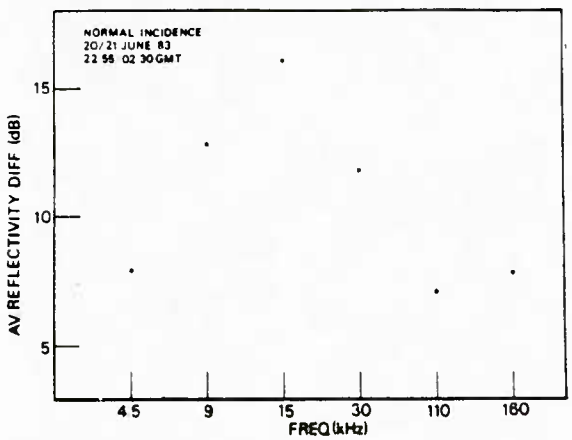

FIG. 11. Frequency dependence of relative reflectivity, as measured with the Deep Tow multifrequency acoustic array. Each point represents the difference in reflectivity between a densely nodule covered patch and bare mud at the acoustic frequency indicated. For the data shown in this figure, the transmit pulse lengths at the various frequencies are: 0.9 ms (4.5 and 9 kHz); 1.0 ms (30 and 100 kHz), and 1.1 ms (15 and 60 kHz). The Deep Tow instruction package is approximately 80 m off the bottom.

ACKNOWLEDGMENTS

The work reported here involved the cooperative efforts of many people including the captains and crews of the R/V *Thomas Washington* and *Melville*. Special thanks go to F. V. Pavlicek for his support during the development of the Sea Beam acoustic data acquisition system which made this work possible. I am especially indebted to Dr. F. N. Spiess and Dr. R. C. Tyce for their valuable suggestions and critical reviews of this paper and also grateful to J. Griffith for the art work, R. Hagen for the final editing, and A. Plueddemann for helpful comments. The Sea Beam work was supported by the Office of Naval Research, Contract No. N00014-79-C-0472. Shiptime and the Deep Tow work were funded through grants from the National Science Foundation and the National Oceanic and Atmospheric Administration. Contribution of the Scripps Institution of Oceanography, new series.

REFERENCES

Bischoff, J. L. and Piper, D. Z., 1979, Marine geology and oceanography of the Pacific manganese nodule province: Marine Science, 9, Plenum Press.

Breaker, L. C., and Winokur, R. S., 1967, The variability of bottom reflected signals using the Deep Research Vehicle ALVIN: U.S.N. Oceanog. Office IR No. 67–92.

Breslau, L., 1967, Classification of sea-floor sediments with a shipborne

acoustical system: Woods Hole Ocean. Inst. contribution no. 1678.
Clay, C. S., and Leong, W. K., 1973, Acoustic estimates of the topography and roughness spectrum of the sea floor southwest of the Iberian Peninsula, *in* Physics of sound in marine sediments: Hampton, L., Ed., Plenum Press, 373–446.
Clay, C. S., and Medwin, H., 1977, Acoustical oceanography: principles and applications: John Wiley and Sons.
Duranton, R., Michel, J. L., and Grandvaux, B., 1980, Epaulard = an unmanned, untethered vehicle for deep ocean survey: Proc. 12th Annual Offshore Tech. Conf., OTC 3680, 41–48.
Galerne, E., 1983, Epaulard ROV used in NOAA polymetallic sulfide research: Sea Tech., 24, 40–42.
Hamilton, E. L., 1970a, Sound velocity and related properties of marine sediments, North Pacific: J. Geophys. Res., 75, 4423–4446.
——— 1970b, Reflection coefficients and bottom losses at normal incidence computed from Pacific sediment properties: Geophysics, 35, 995–1004.
Heezen, B. C., and Hollister, C. D., 1971, Chap. 10 *in* The face of the deep: Oxford Univ. Press.
Mackenzie, K. V., 1960, Reflection of sound from coastal bottoms: J. Acoust. Soc. Am., 32, 221–231.
Magnuson, A. H., 1983, Manganese nodule abundance and size from bottom reflectivity measurements: Marine Mining, 4, 265–296.
Magnuson, A. H., Sundkvist, K., Ma, Yu., and Smith, K., 1981, Acoustic soundings for manganese nodules: Proc. 13th Annual Offshore Tech. Conf., OTC 4133, 147–161.
Magnuson, A. H., Sundkvist, K., Ma, Yu., Riggins, D., and Sen, R., 1982, Remote acoustic sensing of manganese nodule deposits: Proc. 14th Annual Offshore Tech. Conf., OTC 4260, 431–444.
Mizuno, A., and Moritani, T., 1976, Manganese nodule deposits of the Central Pacific Basin, *in* World mining and metals technology: 267–281.
de Moustier, C., 1985, Approaches to backscattering measurements of the deep sea floor: Scripps Inst. of Ocean. Ref. 85.
Parrot, D. R., Dodds, D. J., King, L. H., and Simpkin, P. G., 1980, Measurements and evaluation of the acoustic reflectivity of the sea floor: Can. J. Earth Sci., 17, 722–737.
Patterson, R. B., 1967, Relationships between acoustic backscatter and geological characteristics of the deep ocean floor: J. Acoust. Soc. Am., 46, 756–761.
Piper, D. Z., Leong, K., and Cannon, W. F., 1979, Manganese nodule and surface sediment compositions: Domes sites A, B, and C, *in* Marine geology and oceanography of the Pacific manganese nodule province: Marine Sci., 9, Plenum Press, 437–473.
Rapport de l'Académie des Sciences, Paris, 1984, Les nodules polymétalliques faut-il exploiter les mines océaniques?: Gauthier-Villars.
Renard, V., and Allenou, J. P., 1979, Seabeam, multi-beam echosounding in "Jean Charcot". Description, evaluation and first results: Internat'l Hydrogr. Rev. LVI(1), 35–67.
Spiess, F. N., 1980, Ocean acoustic remote sensing of the sea floor: Nat. Ocean. and Atmos. Adminis. Workshop on Ocean Acoustic Remote Sensing, II, Seattle, 11-1, 11-38.
Spiess, F. N., Hessler, R., Wilson, G., Weydert, M., and Rude, P., 1984, Echo I cruise report: Scripps Inst. of Ocean. Ref. 84-3.
Spiess, F. N., and Lonsdale, P. F., 1982, Deep Tow rise crest exploration techniques: MTS Journal, 16, 67–75.
Spiess, F. N., and Tyce, R. C., 1973, Marine Physical Laboratory Deep Tow instrumentation system: Scripps Inst. of Ocean. Ref., 73-4.
Stanton, T. K., 1984, Sonar estimates of sea floor microroughness: J. Acoust. Soc. Am., 75-3, 809–818.
Sumitomo Metal Mining Co., LTD., Multi-frequency exploration system: (MFES) Tech. inf. 24-8, 4-Chome Shimbashi, Minato-ku, Tokyo.
Tyce, R. C., 1976, Near-bottom observations of 4 kHz acoustic reflectivity and attenuation: Geophysics, 41, 673–699.
Tyce, R. C., Mayer, L. A., and Spiess, F. N., 1980, Near-bottom seismic profiling: High lateral variability, anomalous amplitudes, and estimates of attenuation: J. Acoust. Soc. Am., 68, 1391–1402.
Urick, R. J., 1983, Principles of underwater sound, 3rd ed.: McGraw-Hill Book Co.
Zhitkovskii, Y. Y., and Lysanov, Yu. P., 1966, Reflection and scattering of sound from the ocean bottom (review): Soviet Phys. Acoust., 13, 1–13.

Chapter IV

BEYOND BATHYMETRY: MAPPING ACOUSTIC BACKSCATTERING FROM THE DEEP SEAFLOOR WITH SEA BEAM.

IV.1. ABSTRACT

In its standard mode of operation, the multibeam echo-sounder Sea Beam produces high resolution bathymetric contour charts of the seafloor surveyed. However, additional information about the nature of the seafloor can be extracted from the structure of the echo signals received by the system. Such signals have been recorded digitally over a variety of seafloor environments for which independent observations from bottom photographs or sidescan sonars were available.

An attempt is made to relate the statistical properties of the bottom-backscattered sound field to the independently observed geological characteristics of the seafloor surveyed. Acoustic boundary mapping over flat areas is achieved by following trend changes in the acoustic data both along and across track. Such changes in the acoustics are found to correlate with changes in bottom type or roughness structure. The overall energy level of a partial angular-dependence function of backscattering appears to depend strongly on bottom type, whereas the shape of the function does not. Clues to the roughness structure of the bottom are obtained by relating the shape of the probability density function of normal-incidence echo envelopes to the degree of coherence in the backscattered acoustic field.

IV.2. INTRODUCTION

In the past few years, multibeam echo-sounders have become available to the scientific community, allowing investigators to map, with high resolution and in near-real time, a large swath of seafloor on each traverse of the ship. The bathymetric charts thus obtained represent a great improvement over those drawn from conventional single-point depth recording systems. However, bathymetry reveals the shape of seafloor features only to the resolution of the sounding system; it does not yield other seafloor characteristics such as bottom type or bottom microroughness and their respective lateral homogeneity.

Because bottom roughness and variations in bottom substrate cause fluctuations in the backscattered acoustic signal, such seafloor characteristics can be inferred in part by analyzing the structure and the variations of this signal over several transmission cycles (pings). This analysis is necessarily statistical, and deals with an ensemble of independent samples since, as the ship moves, each ping ensonifies a slightly different portion of seafloor. In order to relate the statistics of the backscattered sound field to the characteristics of the seafloor from which it emanates, two main theoretical approaches have been taken. By analogy with the Huygens-Fresnel principle of physical optics [Born and Wolf, 1970], both approaches consider that the sound field scattered by the seafloor consists of elementary waves in mutual phase interference. Their difference lies in the representation of the irregularities of the seafloor. In the first approach the seafloor is a surface whose irregularities are described by a root-mean square (rms) roughness in the vertical dimension, and a correlation distance or area in the lateral dimension. The statistics of the surface are then incorporated into the Helmholtz-Kirchhoff formulation of the scattering theory so that statistics of the sound field (usually a Gaussian process) can be used to estimate the characteristics of the surface [Eckart, 1953; Beckmann and Spizzichino, 1963;

Tolstoy and Clay, 1966; Clay and Leong, 1974; Clay and Medwin, 1977; Bass and Fuks, 1979; Brekhovskikh and Lysanov, 1982]. The second approach describes the rough surface as a random distribution of point scatterers reradiating independently in time. It is the quasiphenomenological model of Faure [1964], O'lshevskii [1967], and Middleton [1967], which uses a Poisson process giving clues to the density of the scatterers. In this model, however, no relation exists between the statistics of the scatterers and those of the rough surface. For this reason, the first approach mentioned above is preferred in this paper.

In the Helmholtz-Kirchhoff formulation it is possible to determine a measure of the degree of coherence in the backscattered sound-field, and use it to relate the shape of the probability density function (pdf) of echo envelopes to the characteristics of the surface (rms roughness, correlation function) [Stanton, 1984]. Because of their inherent narrow beam geometry, multibeam echo-sounders are well suited for such analysis. In addition, backscatter measurements with well defined spatial resolution are obtainable both along and across the ship's track. A description of seafloor characteristics is then possible in terms of acoustic boundaries.

This paper presents the results of an experiment to map seafloor acoustic backscattering boundaries with a Sea Beam multibeam echo-sounder operating at a frequency of 12 kHz with a 7 ms pulse length and a 2 2/3 degree angular resolution. As this system does not retain the acoustic data it receives, a parallel data acquisition system [de Moustier, 1985a] built by the Marine Physical Laboratory (MPL) of the Scripps Institution of Oceanography was used to record digitally the envelope of the detected echoes over a variety of sea floor environments. These data are analyzed as follows:

(1) First-order statistics (mean and variance) of peak amplitude in the near-specular direction, and of total energy for nonspecular beams serve to quan-

tify spatial homogeneity of the backscattered sound field.

(2) Angular dependence of total energy is used to complement (1) in the estimation of acoustic boundaries over the swath of seafloor ensonified by the Sea Beam.

(3) Probability density functions of peak amplitude in the near-specular direction are compared to a Rician pdf to estimate the degree of coherency of the backscattered signals, yielding a qualitative estimate of the roughness structure of the seafloor.

However, the lack of phase information, occasional saturation in both the data acquisition and the Sea Beam systems, and sidelobe interference problems limit the scope of this analysis. Therefore this paper only intends to show the potential for determining seafloor characteristics that exists in acoustic backscatter measurements derived from a multibeam echo-sounder. Also, acoustic measurements alone are insufficient to determine the exact nature of the bottom. Consequently ground truth must be obtained by independent remote sensing (e.g. deep sea photography and/or television, core or grab samples, etc.). To this end most of the data presented here are supported by at least one independent source of measurements.

IV.3. THEORY

In this section we review the theory of seafloor acoustic backscattering using the Helmholtz-Kirchhoff formulation, and consider its applicability to backscatter measurements made with a Sea Beam system. Next we derive an expression for the degree of coherence of the backscattered sound field valid for all roughness within the limits of the Kirchhoff approximation. This is an extension of Stanton's [1984] small-roughness derivation, which relates the degree of coherence in the field to the roughness and correlation structure of the scattering surface. An estimate of these parameters is then obtainable from the shape of the pdf of normal-incidence echo envelopes.

IV.3.1 Seafloor acoustic backscattering

When measuring acoustic backscatter from the deep seafloor, the first common observation is that individual echoes are not reproducible and that there can be several dB of variation in the amplitude of the returned signal from one ping to the next. The backscattering process is therefore considered stochastic, and its description needs to be statistical.

In its general form, the narrow-band acoustic backscatter is expressed as a random process $U(t)$ such that:

$$U(t) = E \cos(\omega_o t + \psi). \tag{1}$$

where E is the signal envelope, ψ its phase and ω_o the carrier frequency. All the information concerning the random function U is therefore contained in E and ψ, which are random functions as well.

The function U represents the output of the receiving hydrophone array, commonly a voltage, which is proportional to the sound pressure of the bottom echo impinging upon the array. Expressions for this sound pressure have been derived [Tolstoy and Clay, 1966; Clay and Leong, 1974; Clay and Medwin, 1977; Bass and Fuks, 1979; Brekhovskikh and Lysanov, 1982] using the Helmholtz-Kirchhoff formulation in the bistatic scattering from a rough surface. In the backscattering case, omitting the time dependence and propagation losses, a receiver at Q (Fig. 4.1) will sense the pressure:

$$p(Q) = jB_1 \exp(2jkR_o) \int_{-\infty}^{+\infty}\int D_o \exp\left[2j\left(ax + c\varsigma + \frac{k}{2R_o}(x^2\cos^2\theta + y^2)\right)\right] dxdy$$

$$\text{with} \begin{cases} a &= \mathrm{k} \sin\theta \\ c &= -\mathrm{k} \cos\theta \\ B_1 &= \dfrac{kB\mathbf{R}}{2\pi R_o^2 \cos\theta} \end{cases} \tag{2}$$

The notation follows that of Clay and Medwin [1977, (Appendix 10)] where B is

proportional to the source power, D_o is the source directivity, k is the acoustic wave number and **R** is the reflection coefficient. As shown in Figure 4.1, R_o is the range to the center of the scattering region and θ is the angle of incidence. In their notation $\theta = \theta_1$ with $\theta_2 = -\theta_1$ and $\theta_3 = 0$. a and c are the horizontal and vertical components of wave number. ς is the normal deviation of the scattering surface from the xy plane and depends on position in the plane: $\varsigma = \varsigma(x,y)$; it characterizes the roughness of the surface. In the limit $\varsigma = 0$, corresponding to a plane surface, the return is a specular reflection at normal incidence, and outside of normal incidence Eq. (2) is a function of the beam pattern of the acoustic array. At the other extreme, when ς is large the return comes mostly from acoustic energy scattered by the rough surface back towards the receiver. So in the general case the return is a combination of scattered (incoherent) and reflected (coherent) energy which varies depending on the angle of incidence and the beam pattern of the array.

Eq. (2) is derived in the far-field of the transmit/receive system so that ranges R can be approximated by R_o (Fig. 4.1) in the expressions of the incident and backscattered pressure fields except in the phase terms, where R is expanded to second order terms to account for Fresnel zone contributions. This approximation is valid for Sea Beam's 12 cm wavelength at ocean depths.

The Kirchhoff approximation is also used. It assumes that in the boundary conditions on the surface, the reflection coefficient **R** can be used at every point on the rough surface by approximating the field at any point on the surface by that which would be present on the tangent plane at that point (Ch. 3 of Beckmann and Spizzichino [1963]). This requires that the radius of curvature of the irregularities on the seafloor be large compared to the acoustic wavelength or that no shadowing effects occur within the ensonified area. These conditions are met in most of the data presented here.

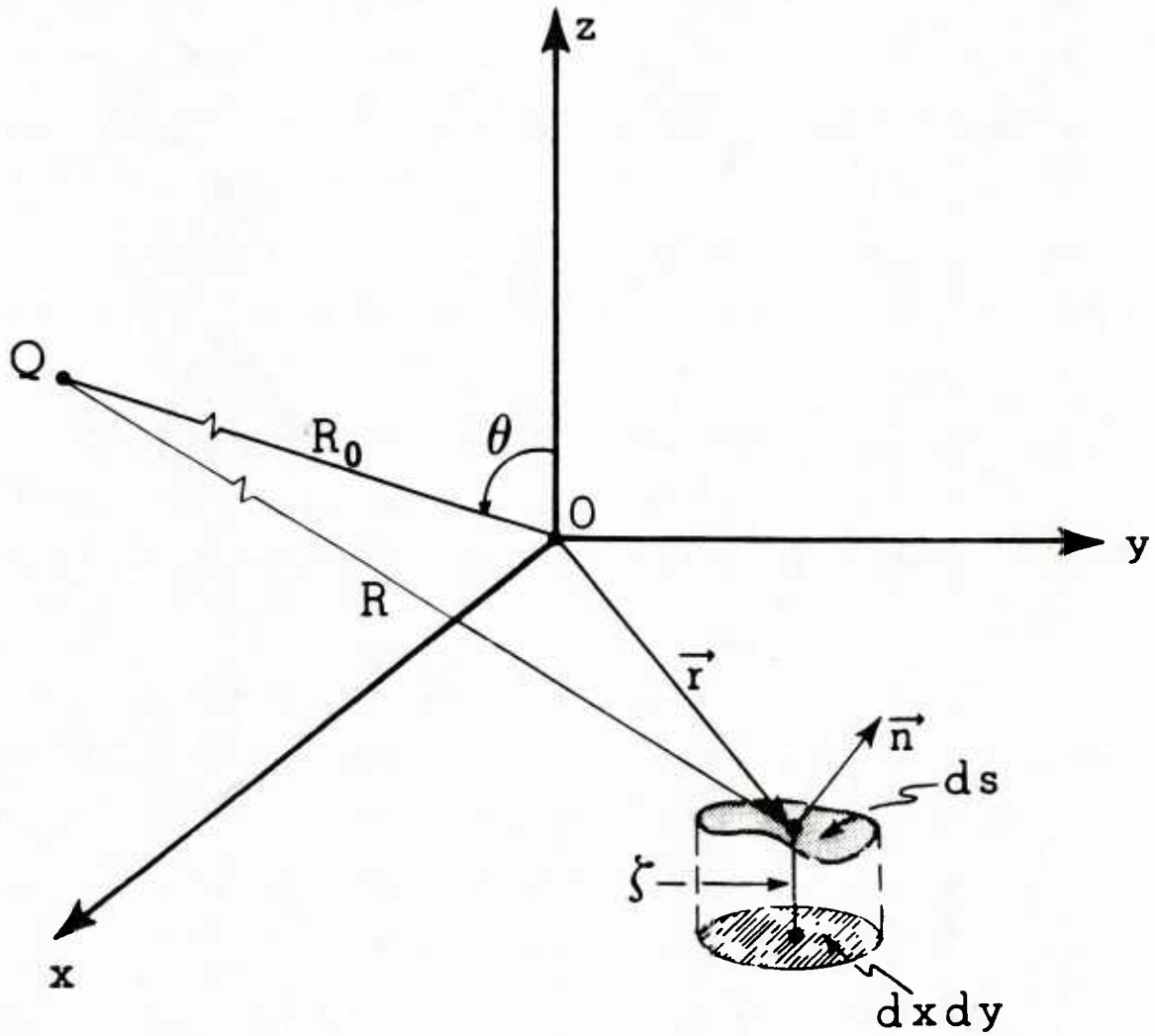

Figure 4.1 *Geometry of backscattering.* Source and receiver are at Q(x,z) a distance R away from the element of surface ds. ζ (x,y) is the elevation of ds above the xy plane.

Eckart's [1953] small-slope approximation was not used in this derivation. Had this approximation been used, the angular dependence in the fraction B_1 of Eq. (2) would appear as a $\cos\theta$ in the numerator instead of the denominator. The discrepancy between these two results comes from the contribution of the horizontal component of wavenumber (a), which is neglected in the small-slope approximation.

Eq. (2) also assumes that the area ensonified is small compared to R_o, so that the dependence of R_o on x,y or ς can be ignored. Likewise $\mathbf{R}$, a and c, which depend mostly on the angle of incidence θ, are assumed to have only small variations within the scattering area. These approximations therefore require that the acoustic system have a small beam width and commensurate pulse length. Both assumptions are reasonable for the Sea Beam system.

It follows that for a given angle of incidence θ, the random character of $p(Q)$ in Eq. (2) is mostly due to the fluctuations of the phase term $e^{2jc\varsigma}$, which accounts for the irregularities of the bottom. As a consequence, the bottom roughness ς is considered a random process, a statistical description of the backscattered sound field can be achieved by ensemble-averaging returns from successive pings. Such returns are independent from each other since the ship moves between pings and a slightly different portion of seafloor is sampled every time. For an ensemble of such surfaces over several pings, the stochastic function $\varsigma(x,y)$ is characterized by a rms roughness amplitude (assuming ς has a zero mean)

$$\sigma = <\varsigma(x,y)^2>^{1/2}, \tag{3}$$

a "correlation function":

$$C(x',y') = \frac{1}{\sigma^2} <\varsigma(x,y)\, \varsigma(x + x',\, y + y')> \tag{4}$$

and a pdf W(ς). Eq. (3) and (4) describe respectively the vertical and the lateral dimensions of the random rough surface. (Note that in the statistics literature, Eq. (4) is referred to as a normalized correlation function or correlation coefficient).

The (ensemble) average pressure is then:

$$<p>_{\mathrm{E}} \approx \int_{-\infty}^{+\infty} pW(\varsigma)d\varsigma = p_o <e^{2jc\varsigma}> \tag{5}$$

where p_o is the reflection from a plane interface ($\varsigma = 0$ in Eq. (2)), and $<e^{2jc\varsigma}>$ is defined [Papoulis, 1965] as the characteristic function of ς.

Assuming ς to be normally distributed with zero mean, Eq. (5) reduces to:

$$<p>_{\mathrm{E}} = p_o e^{-2c^2\sigma^2}, \quad c^2 = k^2 \cos^2\theta \tag{6}$$

where the exponential term is associated with the degree of coherence in the backscattered sound [Eckart, 1953; Tolstoy and Clay, 1966]. For large $c^2\sigma^2$, $<p>_{\mathrm{E}}$ tends to zero and the backscatter is incoherent. Conversely, as $c^2\sigma^2$ tends to zero (plane interface) $<p>_{\mathrm{E}}$ tends to p_o and the backscatter is coherent.

Eq. (6) makes it possible to estimate the rms roughness σ directly from measurements of the coherently backscattered signals $<p>_{\mathrm{E}}$. However, although this is a proven technique [Tolstoy and Clay, 1966; Clay and Leong, 1974; Clay, 1966; Proud et al., 1960], it requires measurements of the phases of the echo signal, which are not available in our data. For this reason, we resort to the mean square pressure:

$$<p^2>_{\mathrm{E}} = <pp^*>_{\mathrm{E}} \tag{7}$$

where p^* is the complex conjugate of p.

Substitution of Eq. (2) yields:

$$<p^2>_{\mathrm{E}} \approx B_1^2 \int_{-\infty}^{\infty}\int\int\int D_1 <\exp\,[2jc(\varsigma-\varsigma')]> dxdydx'dy'$$

$$\text{with } D_1 = D_o\, D_o' \exp\, 2j[a(x-x') + \frac{k}{2R_o}((x^2-x'^2)\cos^2\theta + y^2-y'^2)] \tag{8}$$

The average within the integral is the joint characteristic function of ς and ς'. Under the assumption of a normally distributed surface roughness, the joint characteristic function becomes [Papoulis, 1965]:

$$<\exp\, 2jc(\varsigma-\varsigma')> = \exp(-4c^2\sigma^2(1-C)) \tag{9}$$

where C is the correlation function defined by Eq. (4).

The mean square pressure $<p^2>_E$, which includes the contribution of both the reflected (coherent) and scattered (incoherent) components of the backscatter, is therefore related to the statistics of the rough surface through the rms roughness σ and the spatial correlation function C. To estimate these parameters requires the determination of the respective contributions from the coherent and incoherent components to the total backscattered field, which is equivalent to obtaining a measure of the degree of coherence in the field. To this end, the total mean square pressure is expressed as the sum of the coherent $<p>_E^2$ and incoherent $<S^2>_E$ components [Tolstoy and Clay, 1966, p. 204]

$$<p^2>_E = <p>_E^2 + <S^2>_E \tag{10}$$

where $<p>_E^2 = <p>_E <p^*>_E$, so that $<S^2>_E$ is simply the mean square second moment of p:

$$<S^2>_E \approx B_I^2 \int\int\int\int_{-\infty}^{+\infty} D_1 \Big[<\exp 2jc(\varsigma - \varsigma')> - <\exp 2jc\varsigma><\exp(-2jc\varsigma')> \Big] dx dy dx' dy'. \tag{11}$$

It follows that the ratio of the coherent to the incoherent components,

$$\gamma = \frac{<p>_E^2}{<S^2>_E}, \tag{12}$$

is a measure of the degree of coherence of the backscattered field. Other authors [Novarini and Caruthers, 1972] have used the ratio of the coherent part $<p>^2$ to the total mean square pressure $<p^2>$ as a measure of the degree of coherence. Both expressions are valid, but Eq. (12) is the more useful in this context since it gives a link between the statistics of the backscattered field and a Rician pdf [Stanton, 1984].

To express γ as a function of σ and C, we first use Clay's change of variable (Appendix of Clay and Medwin [1977] and Clay and Leong [1974]):

$$\begin{aligned} x &= x'' + \xi_{/2}, \quad x' = x'' - \xi_{/2} \\ y &= y'' + \eta_{/2}, \quad y' = y'' - \eta_{/2} \end{aligned} \tag{13}$$

to integrate Eq. (11) over x'' and y'', using a Gaussian illumination function for D_o:

$$D_o = \exp(-\frac{x^2}{X^2} - \frac{y^2}{Y^2}) \tag{14}$$

where X and Y are the semi-minor (respectively major) axes of the ellipse outlined by the intersection of the mainlobe of the beam pattern and the scattering surface.

For beamwidths $\Delta\chi$ and $\Delta\phi$ in the x and y directions respectively, we have

$$X = \frac{R\sin\Delta\chi}{\cos\theta}, \quad Y = R\sin\Delta\phi, \tag{15}$$

where ϑ is the angle of incidence of the beam. We assume spatial stationarity for the surface which means that the joint characteristic function of ς and ς' depends only on the distance between points on the surface through $\xi = x - x'$ and $\eta = y - y'$, and that the correlation function depends only on ξ and η: $C = C(\xi,\eta)$. Then, substituting (13) and (14) into (11) and integrating over x'' and y'' yield:

$$<S^2>_E = B_2 \int_{-\infty}^{+\infty}\int D_2(<\exp 2jc(\varsigma - \varsigma')> - <\exp 2jc\varsigma><\exp(-2jc\varsigma')>) d\xi d\eta$$

$$with \quad B_2 = \frac{B_1^2 \pi XY}{2} = \frac{B^2 R^2 k^2 XY}{8\pi R_o^2 \cos^2\theta}, \quad D_2 = \exp\left[-(2aj\xi + \alpha\xi^2 + \beta\eta^2)\right],$$

$$\alpha = \frac{1}{2}\left(\frac{X^2 k^2 \cos^4\theta}{R_o^2} + \frac{1}{X^2}\right) \text{ and } \beta = \frac{1}{2}\left(Y^2\frac{k^2}{R_o^2} + \frac{1}{Y^2}\right). \tag{16}$$

We then obtain an expression for $<p>_E^2 = <p>_E <p^*>_E$ using Eq. (2), (5), and (14)

$$<p>_E^2 = B_2 \int_{-\infty}^{+\infty}\int D_2 <\exp 2jc\varsigma><\exp(-2jc\varsigma')> d\xi d\eta \tag{17}$$

In keeping with the assumption of a normally distributed surface roughness, we substitute the characteristic function by its expression given in Eq (6) and integrate Eq (17) to obtain:

$$<p>_E^2 = \frac{B_2 \pi}{\sqrt{\alpha\beta}} \exp\left(-4c^2\sigma^2 - \frac{a^2}{\alpha}\right) \tag{18}$$

Likewise, using (6) and (9), Eq. (16) becomes:

$$<S^2>_E = B_2 \int_{-\infty}^{+\infty}\int D_2\left[\exp(4c^2\sigma^2 C(\xi,\eta)) - 1\right] d\xi d\eta \tag{19}$$

Hence the result:

$$\gamma^{-1} = \frac{<S^2>_E}{<p>_E^2}$$

$$= \frac{\sqrt{\alpha\beta}}{\pi} \exp\left[a^2/\alpha\right] \int\int_{-\infty}^{+\infty} \left[\exp -(2aj\xi + \alpha\xi^2 + \beta\eta^2)\right]\left[\exp\left(4c^2\sigma^2 C(\xi,\eta)\right) - 1\right] d\xi\, d\eta \qquad (20)$$

which relates the degree of coherence of the backscattered field to the parameters of the rough surface σ and C.

This result is general in the sense that no limitations have been imposed on the wave length of the sound radiation or equivalently on the length scale of the surface roughness. We have only assumed that the surface satisfies the Kirchhoff boundary condition, which requires there be no sharp edges on the scattering surface. We have also assumed that the roughness is normally distributed and that it is spatially stationary by casting the correlation function C as a function of the distance between points on the surface ($C(\xi,\eta)$). Although the applicability of such statistical properties to the ocean floor may seem questionable, especially with regard to stationarity, they are useful in reducing the foregoing integrals to more manageable expressions.

Outside of normal incidence, the coherent component of backscattering is likely to be small or negligible compared to the incoherent component, so that γ will tend to zero. Normal incidence is more interesting in that both components are then equally likely to dominate, depending on the type of rough surface; and there is a direct relationship between γ and the shape of the pdf of normal incidence echo envelopes.

At normal incidence ($\theta = 0$), Eq. (20) becomes:

$$\gamma^{-1} = \frac{\sqrt{\alpha\beta}}{\pi} \int\int_{-\infty}^{+\infty} \exp\left[-(\alpha\xi^2 + \beta\eta^2)\right]\left(\exp\left[4k^2\sigma^2\ C(\xi,\eta)\right] - 1\right) d\xi\, d\eta \qquad (21)$$

To integrate Eq. (21) requires the determination of an analytical form of the correlation function. Although several forms of this function have been used in rough-surface scattering theory [Horton, 1972], most of them are one-dimensional and are restricted

to ripple-like features. Stanton [1984] introduced a correlation area by considering a two-dimensional correlation function which is zero on the average except for a small "elliptic cone" around $\xi = \eta = 0$ where it decreases linearly from 1 at $\xi = \eta = 0$. His application was a surface consisting of ripples, but the approach is also valid for other types of roughness (nodule fields, bed rocks, etc.) more representative of our data. For ease of integration we prefer to use, as a two-dimensional correlation function, an elliptic paraboloid such that:

$$C(\xi,\eta) = \begin{cases} 1 - \dfrac{\xi^2}{l_1^2} - \dfrac{\eta^2}{l_2^2} \geq 0 \\ \\ 0 \quad \text{otherwise} \end{cases} \tag{22}$$

In the limit ($4k^2\sigma^2 \ll 1$) of small to moderate roughness the second exponential in Eq. (21) is expandable in a Taylor series. Keeping the first two terms of the expansion and using Eq. (22), Eq. (21) integrates into:

$$\gamma^{-1} \simeq \frac{16}{3} \frac{\sqrt{\alpha\beta}}{\pi} k^2\sigma^2 l_1 l_2 \tag{23}$$

where l_1 and l_2 are the correlation distances beyond which $C(\xi,\eta) = 0$.

It has been assumed that for $|\xi| \leq l_1$ and $|\eta| \leq l_2$ the contribution of the first exponential term in Eq. (21) can be neglected. This is equivalent to requiring the exponential term to reach e^{-1} outside of the range $|\xi| \leq l_1$ $|\eta| \leq l_2$, so that $\alpha\xi^2 + \beta\eta^2 = 1$ for $|\xi| \succ l_1$ and $|\xi| \succ l_2$. Except for a factor of 2, Eq. (23) is equivalent to Stanton's Eq. (16) [1984]. It shows that for small to moderate roughness, the degree of coherence in the specular backscattered sound field depends on the relative roughness ($k\sigma$) and the correlation area ($l_1 l_2$) of the surface as well as on the beam widths of the measuring system (α,β). Because the same degree of coherence is a parameter which controls the shape of the pdf of normal incidence echo envelopes, Eq. (23) makes it possible to evaluate the parameters of the rough surface directly from the shape of the pdf. Also,

pending determination of the rms roughness from coherent measurements (Eq. (6)), the correlation area is readily obtained from Eq. (23).

IV.3.2 Envelope distributions

As summarized in Appendix A, the Rician distribution [Rice, 1945] is useful in describing the effects of coherent scattering on the shape of the pdf of echo envelopes. By considering the backscattered pressure wave as a sum of a coherent component of rms value A and an incoherent component normally distributed with variance σ_p^2, the parameter γ can be written as:

$$\gamma = \frac{A^2}{\sigma_p^2}. \tag{24}$$

It follows that the Rician distribution for the corresponding echo envelopes E (Eq. 1) can be expressed as a function of E, its second moment $<E^2>$, and γ:

$$W(E) = (2+\gamma)\,\frac{E}{<E^2>}\,\exp\left[-\frac{(2+\gamma)E^2+\gamma<E^2>}{2<E^2>}\right] I_0\left[\frac{E}{<E^2>^{1/2}}\,(\gamma(2+\gamma))^{1/2}\right] \tag{25}$$

In the limit where γ tends to zero (dominance of the incoherent component), Eq. (25) tends to the Rayleigh distribution (Eq. A.4). Conversely, when the coherent component dominates ($\gamma \gg 1$) Eq. (25) tends to a Gaussian-like distribution. A qualitative estimate of the degree of coherence in the backscattered sound field can then be obtained directly from the value of γ that gives the best fit of the Rician distribution to a histogram of the normal-incidence echo-envelope peak distribution.

This is analogous to the determination of the contrast of a speckle pattern [Goodman, 1975] in laser optics. Speckle patterns are the result of constructive and destructive interference between light waves scattered from elementary areas of a rough surface. Their contrast is analogous to γ^{-1} (Eq. 21) since an ideal mirror surface does not produce a speckle pattern (contrast $=0$).

As in optics, useful quantitative results concerning the roughness structure of

the surface are obtained for acoustic backscatter only when the roughness of the surface is a fraction of the acoustic wavelength. In such cases, the value of γ derived from the shape of the pdf can be directly related to the product of the rms roughness and the correlation area of the surface (Eq. 23). For practical purposes, this technique is applicable when $\gamma \geq 1$ because there is little difference in the shape of the pdf's for $0 \leq \gamma \leq 1$ (e.g. Figure 2 of [Stanton, 1984]).

IV.4. SEA BEAM ACOUSTIC DATA.

To explain some of the peculiarities of the Sea Beam data presented here, a brief description of the acoustic geometry is necessary.

IV.4.1 Acoustic geometry

Sea Beam uses two arrays perpendicular to each other. The transmit array consists of twenty projectors aligned along the ship's keel. The outputs of the projectors are amplitude-shaded for sidelobe control according to the Dolph-Chebyschev method [Dolph, 1946], and phase corrected to ensure vertical projection at all times. The resulting beam pattern is 2 2/3 degrees wide in the fore-aft direction and 54 degrees athwartships (Fig. 4.2a). These angles correspond to the half power point of the beam patterns. This convention will be kept in the following.

The receive array consists of forty elements arranged athwartships in a V-shaped array symmetrical about the ship's keel. The outputs of these elements are amplitude-shaded (Dolph-Chebyschev shading) for sidelobe control, and the resulting beam is steered phase-wise to form sixteen preformed beams spaced 2 2/3 degrees apart between +20 and - 20 degrees of incidence. Each beam is 2 2/3 degrees wide in the athwartships direction and 20 degrees fore-aft (Fig. 4.2b). The comparatively wide beam width in the fore-aft direction is meant to accommodate pitch angles of $\pm$ 10 degrees for no pitch correction is performed on the receive array.

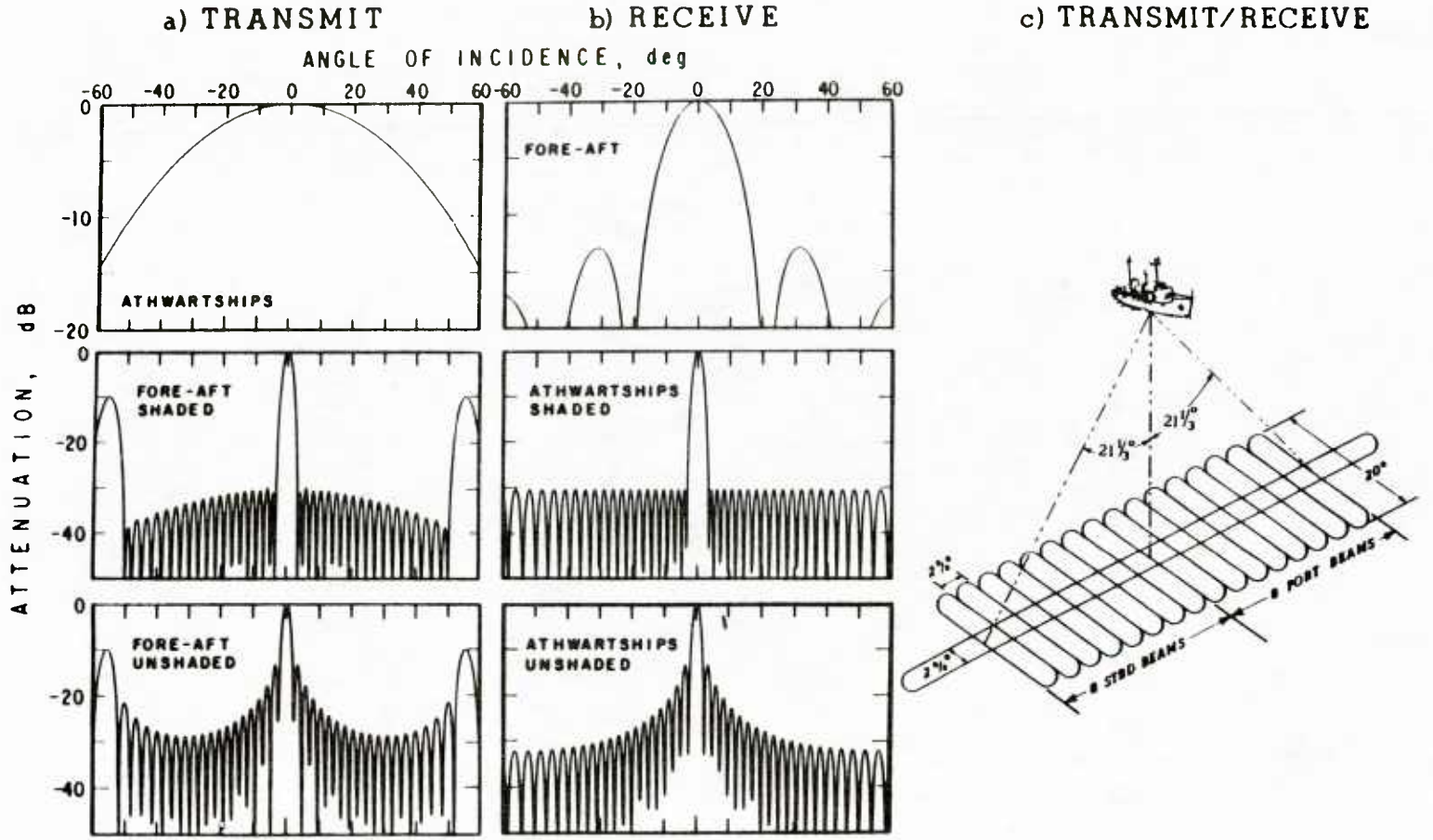

Figure 4.2 *Sea Beam transmit/receive geometry.* Theoretical beam pattern cross-sections are computed in the athwartships vertical plane centered on the array and in the vertical plane through the ship's fore-aft axis. The transmit beam pattern (a) spans 54° athwartships by 2° 2/3 in the fore-aft direction. The receive beam pattern (b) is 20° wide in the fore-aft direction by 2° 2/3 athwartships. Sixteen such beams are formed by steering the receiving hydrophone array athwartships between ± 20° of incidence at 2° 2/3 intervals. The effect of Dolph-Chebyschev amplitude shading is shown for both arrays with Sea Beam's design criterion of 30 dB sidelobe attenuation. A cartoon (c) shows the angular relationship between the mainlobes of the transmit and receive beam patterns. Their intersection is represented by sixteen "squares" 2° 2/3 on a side.

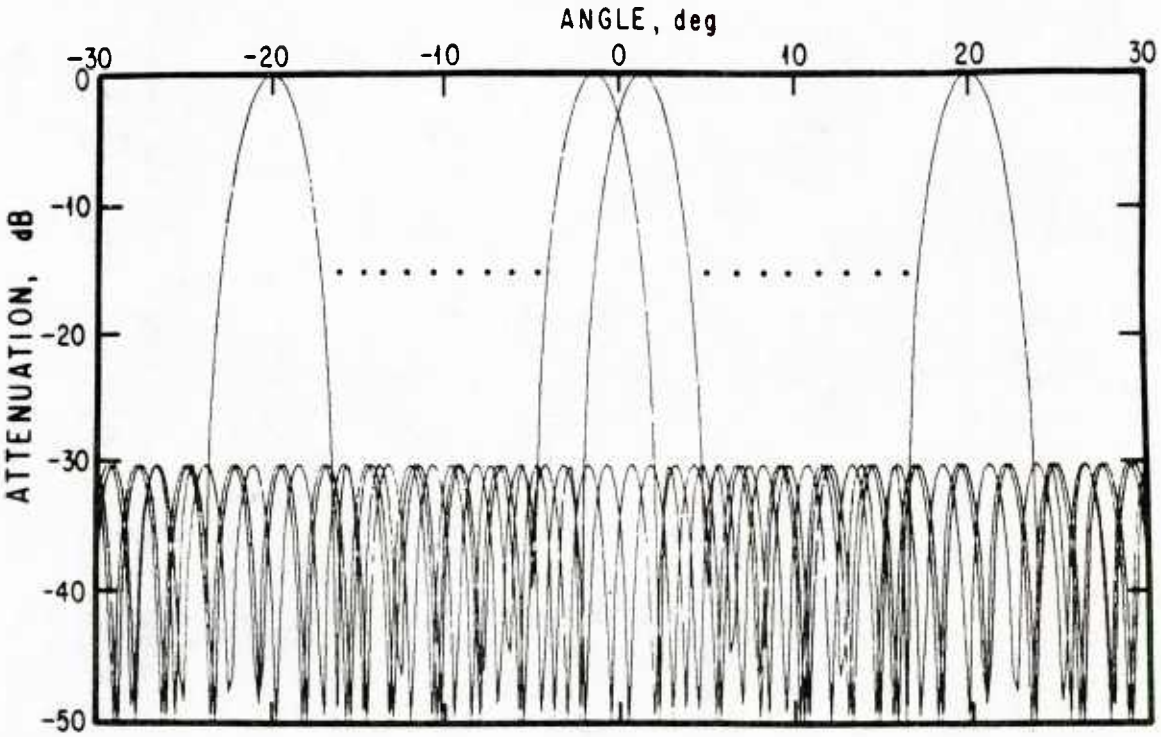

Figure 4.3 *Preformed beams.* Four out of the sixteen preformed beams are displayed to show how sidelobes from each beam "look" into the direction of the mainlobe of all the others. The sidelobe contributions to the sixteen bottom echoes received each ping can be seen in Figure 4.4.

Note also that each of the preformed beams has sidelobes pointing in the direction of (but not necessarily aligned with) the mainlobe of all the other beams (Figure 4.3). As will be shown in the following, this fact is significant when dealing with echo envelopes of the sixteen preformed beams. For a broader description of the Sea Beam system, the reader is referred to a comprehensive review by Renard and Allenou [1979].

IV.4.2 Sea Beam digitized echo envelopes

Figure 4.4 illustrates a typical set of echo envelopes as they appear at the output of Sea Beam's echo-processor receivers. Each envelope corresponds to the return on one of the sixteen preformed beams numbered 1 through 8 from the center of the ship out, on both port and starboard. These data have not been roll-compensated; therefore the ship's center line does not necessarily lie on the true vertical. The ridge of synchronous returns corresponds to energy from a strong return in the near-specular direction leaking into the sidelobes of all the other beams (e.g. starboard beam #1 in this figure). The term near-specular is used here to indicate that because Sea Beam receives with discrete beams, the return may be within 2 2/3 degrees of the specular direction. Likewise, in the following nonspecular beams refer to those beams which are not within 2 2/3 degrees of the specular direction. In its current mode of operation, the Sea Beam echo processor digitizes these echo envelopes and applies ray-bending, roll, gain and sidelobe corrections. A time of arrival is then determined at the center of mass of each of the corrected echoes and is converted into a depth and a cross-track distance. These are in turn logged on magnetic tape as well as recorded on paper as a bathymetric contour chart. No further use is made of the echo signals, which are then discarded. In an effort to preserve these echo signals for analysis, MPL built a parallel acoustic data acquisition system to record digitally data such as that of Figure 4.4 along with a time-varied gain and the ship's roll angle. In this paper some of the envelope data collected with the MPL system suffer

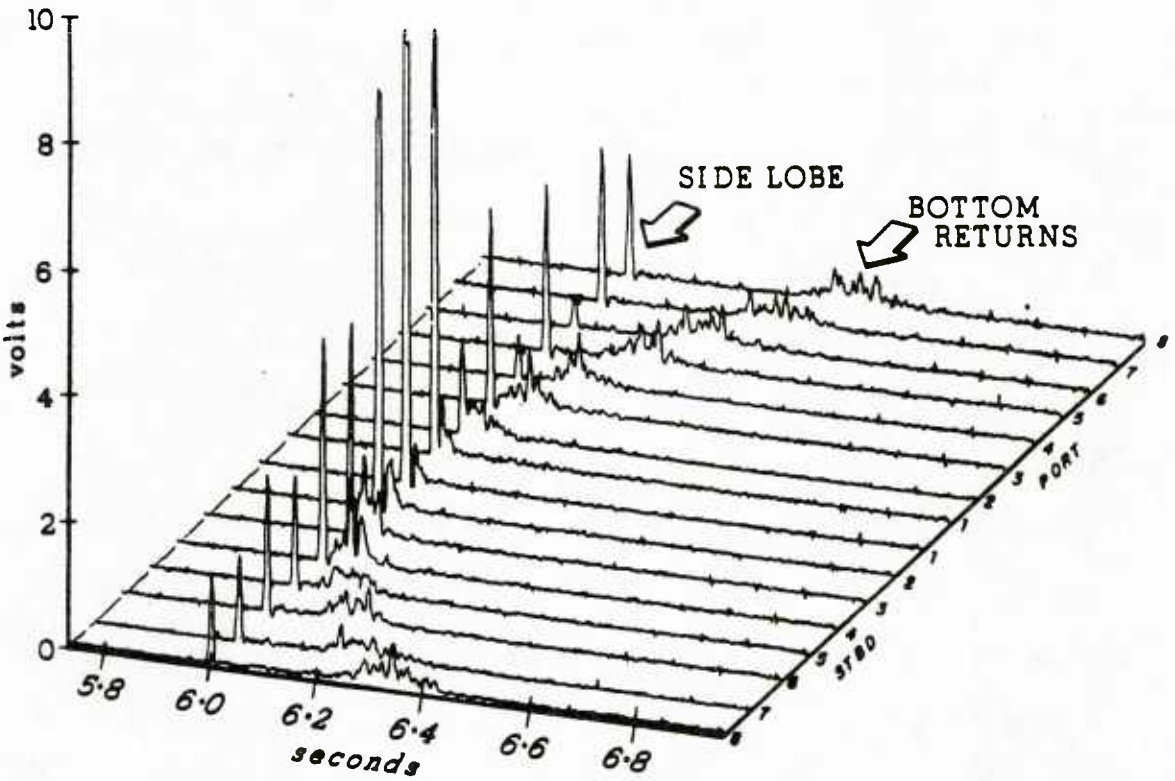

Figure 4.4 *Acoustic signal envelopes of the sixteen preformed beams at the output of Sea Beam's Echo Processor Receivers.* Time is in seconds after transmission. Signal amplitude is in volts corrected for acoustic transmission loss by a time-varied gain. In this display, the data have not been corrected for ship roll or receiver gain. The ridge of synchronous returns is the sidelobe response to a strong return in the near-specular direction (STBD beam #1 in this Figure).

amplitude clipping due to saturation in both the data acquisition system and the Sea Beam echo-processor receivers. The saturation in the receivers occasionally disrupts Sea Beam's echo processing, resulting in spurious depth measurements. Likewise, because the echo processing is done on the envelope of the signals, the system cannot differentiate between sidelobe response and bottom return when the two overlap (e.g. beam # 2 in Fig. 4.4). Improper depth determination and, bathymetric artifacts result. Such bathymetric artifacts have been analyzed in detail elsewhere, [de Moustier and Kleinrock, in press] and we shall not repeat the discussion here. Nevertheless this sidelobe interference constitutes a serious hindrance when analyzing signal envelopes where sidelobe and bottom return overlap. To tell them apart requires phase information which is not available in our present data set.

IV.4.3 Data reduction

Owing to the limitations outlined above, the acoustic data recorded from Sea Beam were reduced to be analyzed in two ways. The first approach concentrates on the statistics of the peak amplitude in the near-specular direction; the second deals with both angular dependence and statistics of total energy in nonspecular beams. To overcome the saturation problem mentioned above, the mean sidelobe response was used to retrieve the peak amplitude of the near-specular returns that appeared clipped. The method assumes that the ratio of the near-specular peak amplitude to the corresponding mean sidelobe response is approximately constant from ping to ping, and that most of the variability in this ratio is due to (1) the slight misalignment of sidelobes with the mainlobe of the near-specular beam (Figure 4.3) and (2) the roll of the ship. For simplicity, only data collected over nearly flat seafloor (slope angles less than 2 2/3 degrees) were used in this exercise, for owing to the acoustic geometry, no specular backscatter is to be expected from bottoms sloping up or down. To avoid bias from bottom returns, the mean sidelobe response was computed as the arithmetic

mean of the peak values of sidelobe contributions well separated from the bottom returns. As an example, beams number port 8-3 and starboard 4-8 would qualify in Figure 4.4. By working on non-clipped data, this mean was then compared with the amplitude of the corresponding near-specular peak by computing their ratio.

From an ensemble of over four hundred such ratios the mainlobe to sidelobe ratio is 17.80 (25 dB) with a standard deviation of 2.14. This value is in agreement with what Dolph [1946] predicted for his amplitude shading method. It is however 2 to 3 dB lower than the level measured by Renard and Allenou [1979] (27-28 dB) on a different Sea Beam system. But because their measurements were done on only two preformed beams, it is reasonable to expect the level obtained by averaging over ten beams to be lower.

The ping-to-ping variations of the near-specular peak were then inferred from the variations of the corresponding mean sidelobe response using the same method. When the sidelobe response had insufficient signal-to-noise ratio, the near-specular return was not clipped so its peak amplitude was used to compute the mean sidelobe level by subtracting 25 dB. Results of this method are illustrated in Figure 4.5.

Because of the time stretching evidenced on the non specular returns (Fig. 4.4), their description is more appropriately based on total energy than on peak amplitude. To establish a common reference between pings, the sixteen beams are roll-compensated and put into a set of beams 2 2/3 degrees apart, one of which is centered on the true vertical. Each roll-compensated beam is obtained by linear interpolation between the two adjacent unstabilized beams. Ideally, a ray-bending correction should also be applied. However, errors resulting from the omission of this correction are small at the steep angles of incidence considered here and are inconsequential in the scope of this paper. Again roll-compensated beams for which sidelobe response and bottom return overlap are disregarded. The total energy in a return is then

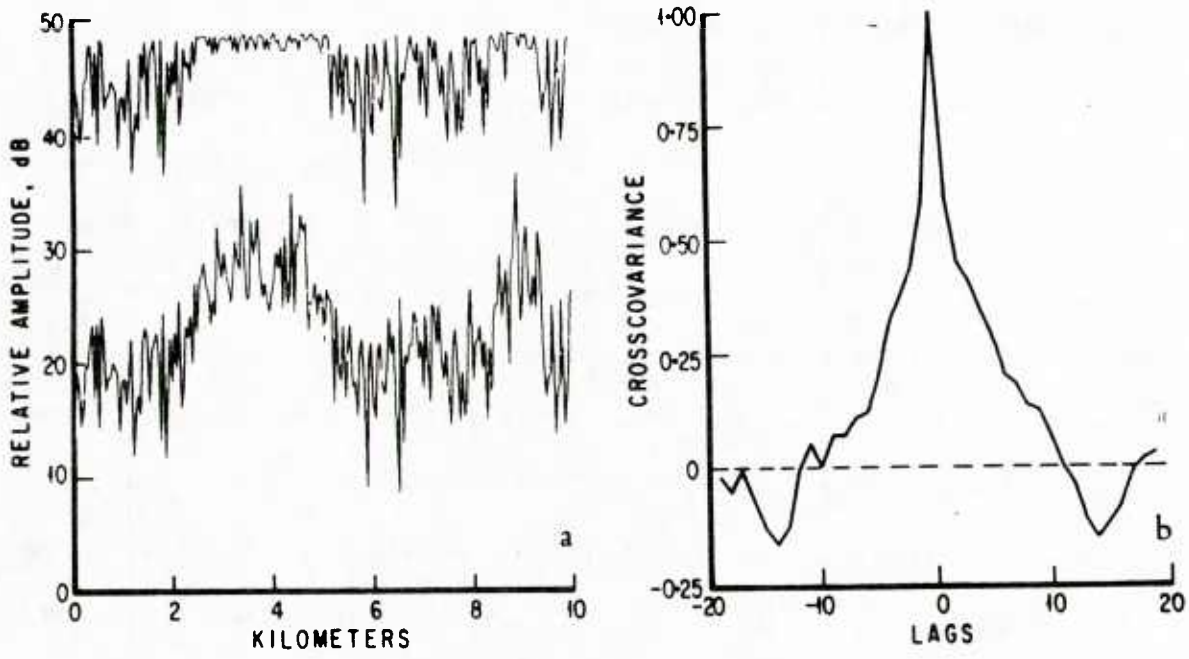

Figure 4.5. Variations in the amplitude of the near-specular return which is clipped in the recorded data (a, top) are recovered from the corresponding mean sidelobe response (a, bottom). Each data point corresponds to one ping. The cross covariance between these two time series, excluding the clipped portions, is shown in (b) where successive lags are successive pings. The mean sidelobe response was found to be 25 dB below the near-specular return.

computed as the difference between the mean square amplitude (signal + noise) in a predetermined window and the mean square noise in an equivalent window. This way a fixed window size can be used for all beams.

As no accurate calibration exists for the Sea Beam system from which this acoustic data was recorded, the following results are given in relative units.

IV.5. RESULTS AND DISCUSSION.

Given that variations in bottom type and bottom roughness are the main factors in the nature of the fluctuations of the acoustic backscatter from the seafloor, data from three geologically different areas have been analyzed to determine what could be learned from the acoustics. Although it is possible to tell these areas apart from analysis of the acoustic data alone, our acoustic data base is too small and incomplete to identify them, and we use ground truth from independent measurements to validate the acoustic measurements made with Sea Beam.

The three areas investigated are: (1) a manganese nodule field in the North Eastern Tropical Pacific (15°N, 125°W) for which there are bottom photographs taken with MPL's Deep Tow instrument package [Spiess and Lonsdale, 1982], as well as box core data; (2) a sedimentary environment in the North San Clemente basin (~ 150 km south-west of San Diego, Calif.) with Deep Tow bottom photographs in the general area; and (3) a lava sheet flow on the crest of the East Pacific Rise around 10°N with supporting data from the Lamont-Doherty Geological Observatory Sea MARC I side-looking sonar [Kosalos and Chayes, 1983] and bottom photographs.

For each area, a composite figure (Figures 4.6,8,10) has been assembled to give a synopsis of the Sea Beam data. Sea Beam bathymetry is shown in a three-dimensional view of a single swath, as a mesh of instantaneous cross track depth profiles, low-pass filtered along track and displayed with a vertical exaggeration of 10. The acoustic data are presented as along-track variations of relative peak amplitude

in the specular direction and relative total energy for nonspecular beams. As described in Section IV.4, the peak amplitude information has been recovered from sidelobe data, and the energy has been calculated only for nonspecular beams where bottom return and sidelobe response were well separated. In all displays, the data have been low-pass filtered with a running mean averaging over the number of pings necessary to traverse a single beam footprint (2 2/3 x 2 2/3 degree) on the seafloor at the depth considered. A coefficient of variation, which is simply the standard deviation normalized by the mean over the averaging interval, is also displayed to give a measure of the variability in the data. Finally, partial angular dependence profiles of total energy are stacked and low-pass filtered along track to show trends in the backscattered acoustic energy both along and across track. The central portion of the angular dependence of total energy has been purposely left out because of our inability to remove the sidelobe contribution contaminating the returns closest to the specular direction without seriously degrading the returns themselves.

In the following discussion, we assess how much can be learned about a portion of seafloor surveyed with Sea Beam by analysis of the acoustic backscatter it receives. We consider successively the system's ability to delineate acoustic boundaries, the use of an angular dependence function of backscattering to differentiate between various types of substrate, and the potential for estimating the microroughness of the bottom.

IV.5.1 Mapping acoustic boundaries

Because most statistical analyses of the backscattered sound field are based upon the assumption of a homogeneous (stationary) scattering surface, it is important to be able to isolate seafloor areas for which this assumption holds. To this end we define an acoustic boundary as the place where a marked change in trend appears in the acoustic data. With a multibeam system such trends can be followed both along

and across tracks, given that it is possible to correct for bottom slope in both directions. In this paper, we simplify the problem by limiting ourselves to nearly flat portions of seafloor.

IV.5.1.a Manganese nodule area:

In a previous paper [de Moustier, 1985b], we used the variations in amplitude of the specular beam alone to infer manganese nodule coverage over a well documented nodule mining site. Although the estimates of coverage were crude, they were in very good qualitative agreement with estimates of coverage derived from Deep Tow bottom photographs of the same area. Our ability to correctly identify bare mud patches, areas sparsely covered with nodules, and areas densely covered throughout the mining field was a good indication that acoustic boundary mapping is feasible with Sea Beam. Here we extend the analysis to nonspecular beams.

As shown in Figure 4.6, the portion of seafloor considered is nearly flat, and the average depth is about 4500 m. At this depth, the Sea Beam transmits every 8 seconds and, since the ship was moving at $\sim$ 5 m/s (10 knots), the spatial sampling interval is roughly 40 m along track. By comparison, the diameter of the vertical incidence footprint is about 200 m, so that it takes five pings to traverse a footprint. This number was used as the averaging interval in the low-pass filter of the data for the area.

With this averaging, the peak amplitude of normal incidence (0°) returns is seen to fluctuate around a mean level of about 15 dB between 0 and 6 km and then drop sharply beyond the 6 km mark (Fig. 4.6). A similar trend, although much better defined, is seen in the mean total energy. For reference, $\pm$ 13 degrees incidence corresponds to a distance across track of $\pm$ 1 km from the vertical incidence point. The drop in level is clearly seen in both port and starboard plots, but it happens $\sim$ 1 km further along track (7 km mark) on the starboard side. It can be followed also on

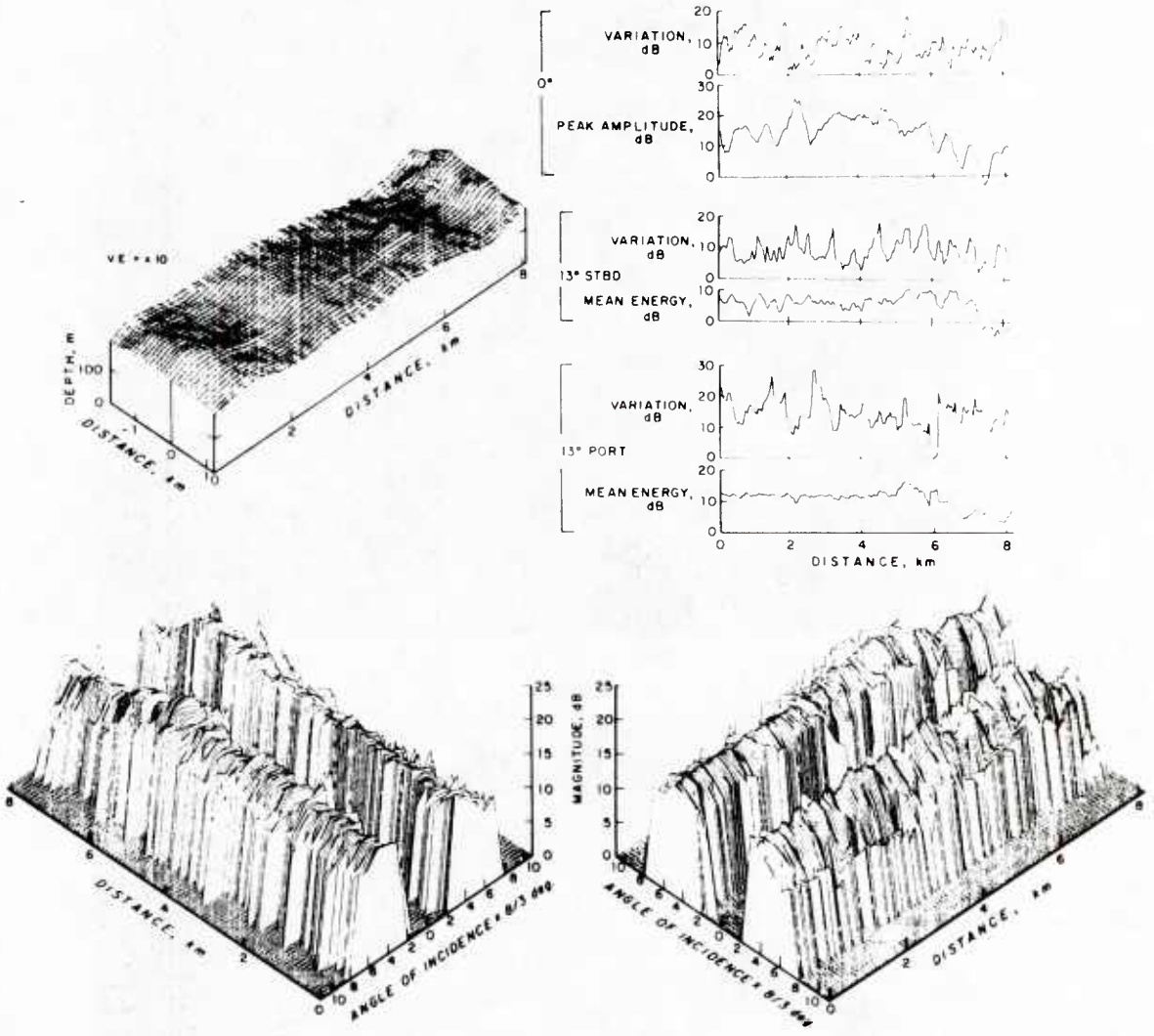

Figure 4.6 *Manganese nodule area: synopsis of Sea Beam data.* Upper left: bathymetry for one swath of Sea Beam. The depth scale in meters is shown with a vertical exaggeration of 10 and its origin is at 4600m. The distance across and along track are in kilometers. Across track, a vertical bar indicates the position of normal incidence. The terrain has a very gentle undulation along track. Upper right: along-track variations of peak amplitude in the near-specular direction ($\sim 0^\circ$ incidence) and of total energy at about 13° incidence. Plots have been low-pass filtered by averaging over five pings. The coefficient of variation (standard deviation/mean) shows the variability in the data for each of the three angles of incidence. Lower: partial angular dependence of total energy and its variations along-track are displayed in both left and right view. The center portion (between $\pm 5^\circ$ 1/3 incidence) has been left out because of sidelobe interference and saturation in the data. The notch seen on the outer starboard side is probably a system-related artifact, for it is found to some extent in all the recorded data.

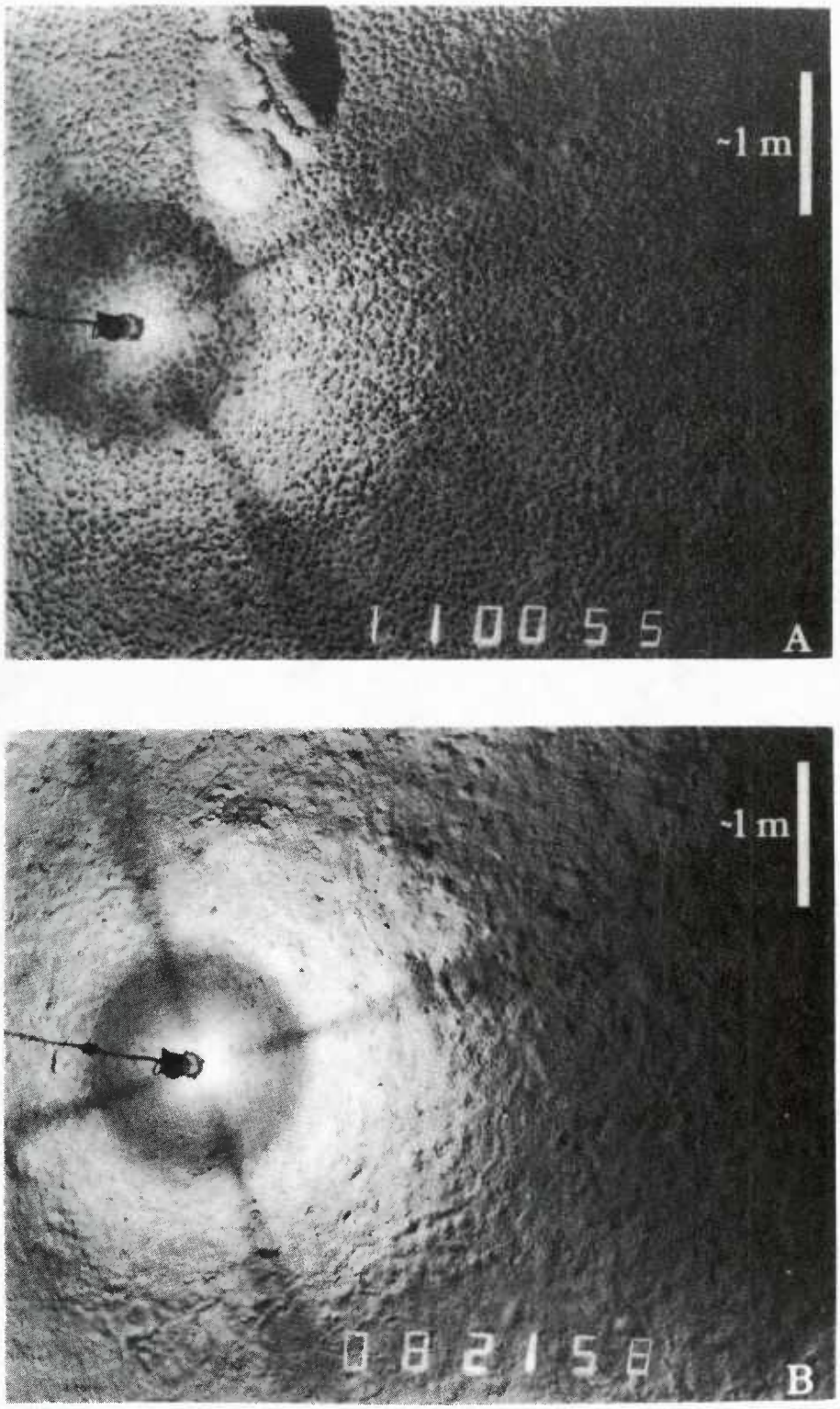

Figure 4.7 *Representative Deep Tow bottom photographs taken in the manganese nodule field.* They show the contrast between a relatively dense coverage of manganese nodules (a) and bare mud (b).

the stacked profiles of total energy, where it is seen to run diagonal to the ship's track. This diagonal therefore defines an acoustic boundary.

Deep Tow bottom photographs taken along the same track show that this boundary is associated with a rapid transition between dense nodule coverage (Fig. 4.7a) and bare mud (Fig. 4.7b). In this case, the change in bottom substrate from nodules to mud, rather than their relative roughness, seems to be the dominant factor in the backscattering process. Also, it is interesting to note that in this area, nonspecular beams energy is better suited for acoustic boundary mapping than peak amplitude in the specular return. The peak amplitude data shown in Figure 4.6 seems to be more sensitive to small variations in bottom slope and to potential bottom focusing effects, and would therefore require more averaging to bring out the underlying trend readily observable in the energy data of nonspecular beams.

IV.5.1.b North San Clemente basin

The portion of Sea Beam data considered in Figure 4.8 corresponds to a flat area around 32°30′N, 118°10′W. The bathymetry shows a small diagonal step rising 10 m over 150 m, and the average depth is 1900 m. At this depth Sea Beam transmits every 4 seconds. In this instance, the ship speed was about 1 m/s ($\sim$ 2 knots), yielding a sampling interval along track of roughly 4 m, so that 22 pings are necessary to transverse the length of a vertical incidence footprint (88 m). This number of pings was therefore used as the averaging interval to low-pass filter the data.

Because this averaging interval is large, the profile of normal incidence peak amplitude data appears relatively smooth, with less variability than that of Figure 4.6. No major trend changes are observable in this profile (Fig. 4.8). The drop in amplitude (arrow) around the 1 km mark is most likely due to the small bathymetric step. The uniformity of this portion of seafloor is confirmed by the mean total energy data even though a small undulation with a 1.5 km wavelength is noticeable on both

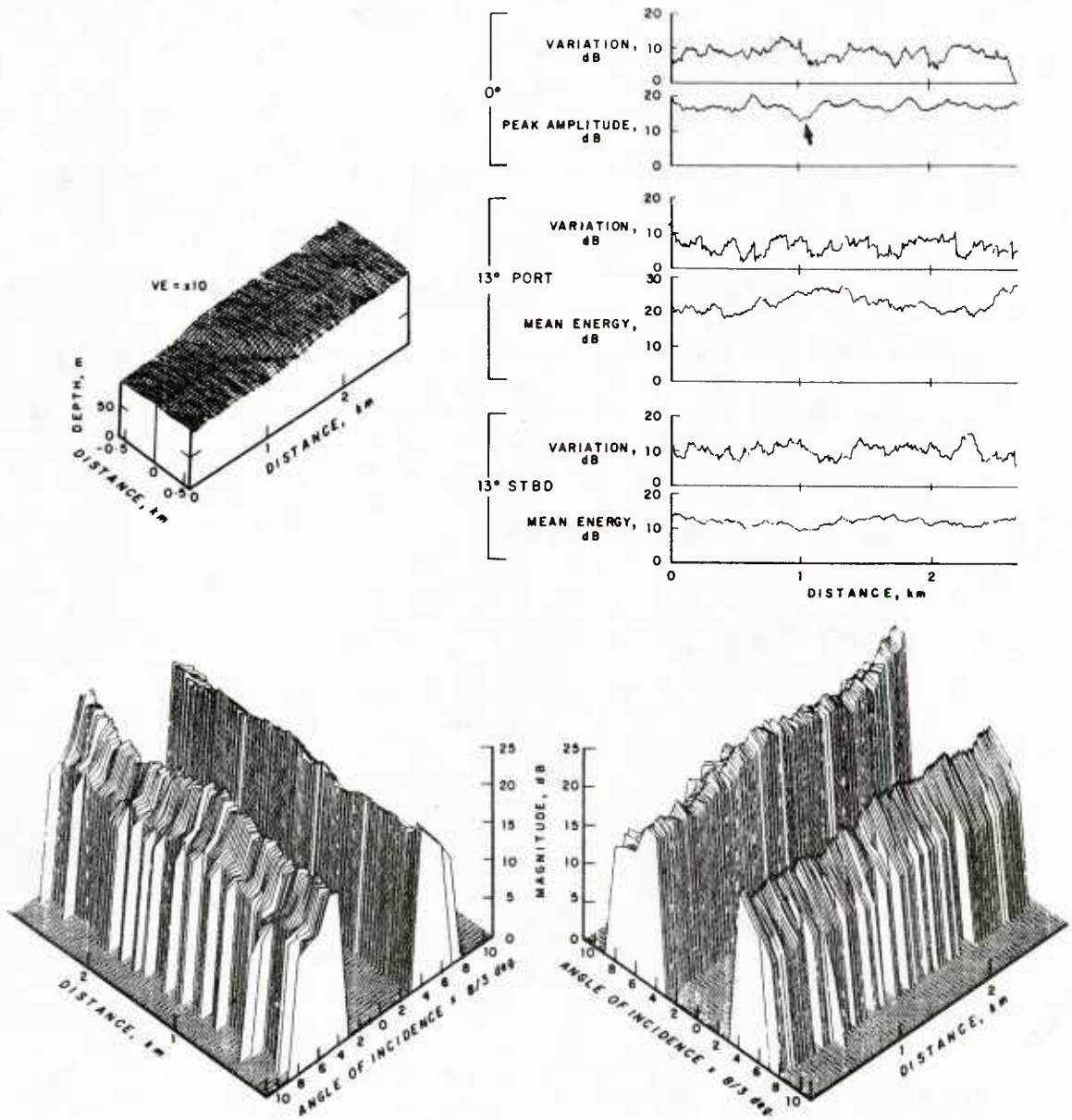

Figure 4.8 *North San Clemente Basin: synopsis of Sea Beam data.* Layout and scales are the same as in Figure 4.6. The origin of the depth scale is at 2000 m. Depth is shown with a vertical exaggeration of 10. A small step ($\sim$ 10 m high) runs diagonal to the swath around the 1 km mark along-track. Plots of amplitude and total energy data have been low-pass filtered by averaging over 22 pings. The small step in the bathymetry appears in the amplitude data (arrow) as a marked dip in amplitude. The gap in the center portion of the angular dependence of total energy is larger in this figure than in Figure 4.6 because as the water depth decreases so does the time separation between arrivals on individual beams. As a result, the sidelobe interference affects more beams.

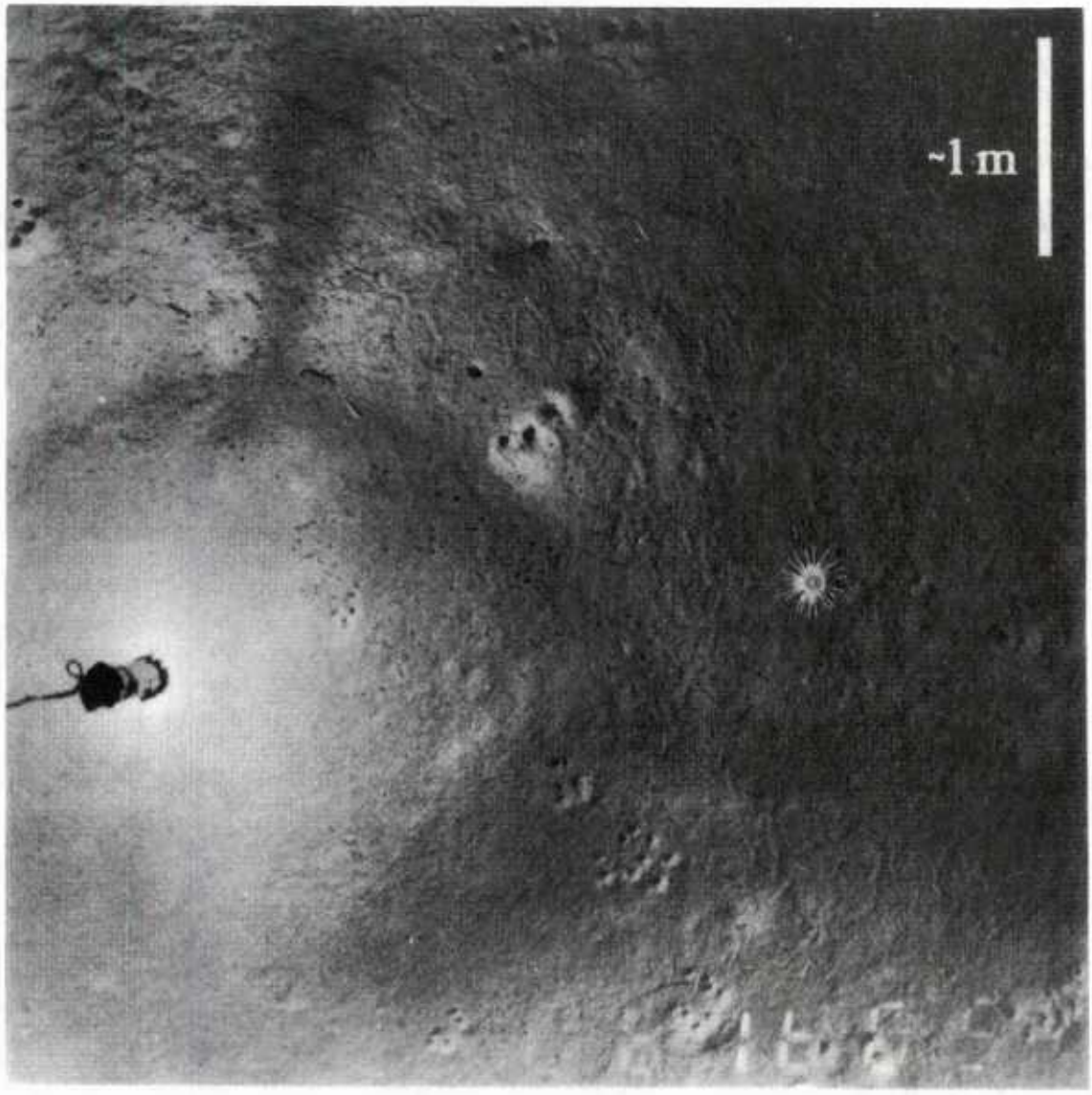

Figure 4.9 *Deep Tow bottom photograph taken in the North San Clemente Basin.* The sediments appear relatively smooth with occasional animal generated boreholes and craters, and numerous worm tracks.

port and starboard. This trend is most marked at 13 degrees incidence to port. Distances across track are 440 m and 545 m from the vertical incidence point at 13 and 16 degrees incidence respectively. As seen in the stacked profiles of total energy, the undulations on port and starboard are not symmetric with respect to vertical incidence, but appear to be offset diagonally from each other in roughly the same orientation as the bathymetric step. A tenuous acoustic boundary can then be defined on this Sea Beam swath as a patch of higher backscatter extending 1.5 km along track and trending diagonally across track.

Owing to the complex nature of sedimentation patterns in this area, it is difficult to relate the patchiness observed in the acoustics to geological processes. Sediments of the San Clemente basin are of both turbidite and pelagic origin and contain mostly fine grained sand and muds (biogenic and/or micaceous) [Normark and Piper, 1972; Emery, 1960]. Deep Tow bottom photographs taken in the vicinity (Fig. 4.9) show a smooth sedimentary bottom with evidence of intense animal activity (worm tracks and feces, holes and craters, etc.) so that bioturbation must play a major role in the vertical distribution of sediments. Several speculations can be made to account for the acoustic boundary observed. It could be due to a patch of seafloor where sand has been bioturbated with the overlying mud, thereby enhancing its backscattering properties. A thinning of the surficial mud layer over sand would have a similar effect. Another possibility is a change in the fine-scale roughness of the bottom as a result of animal activity, higher backscattered energy corresponding to a rougher interface. More data (subbottom profiles and/or cores) are necessary to determine whether roughness or bottom type or a combination dominates the backscattering process in this area.

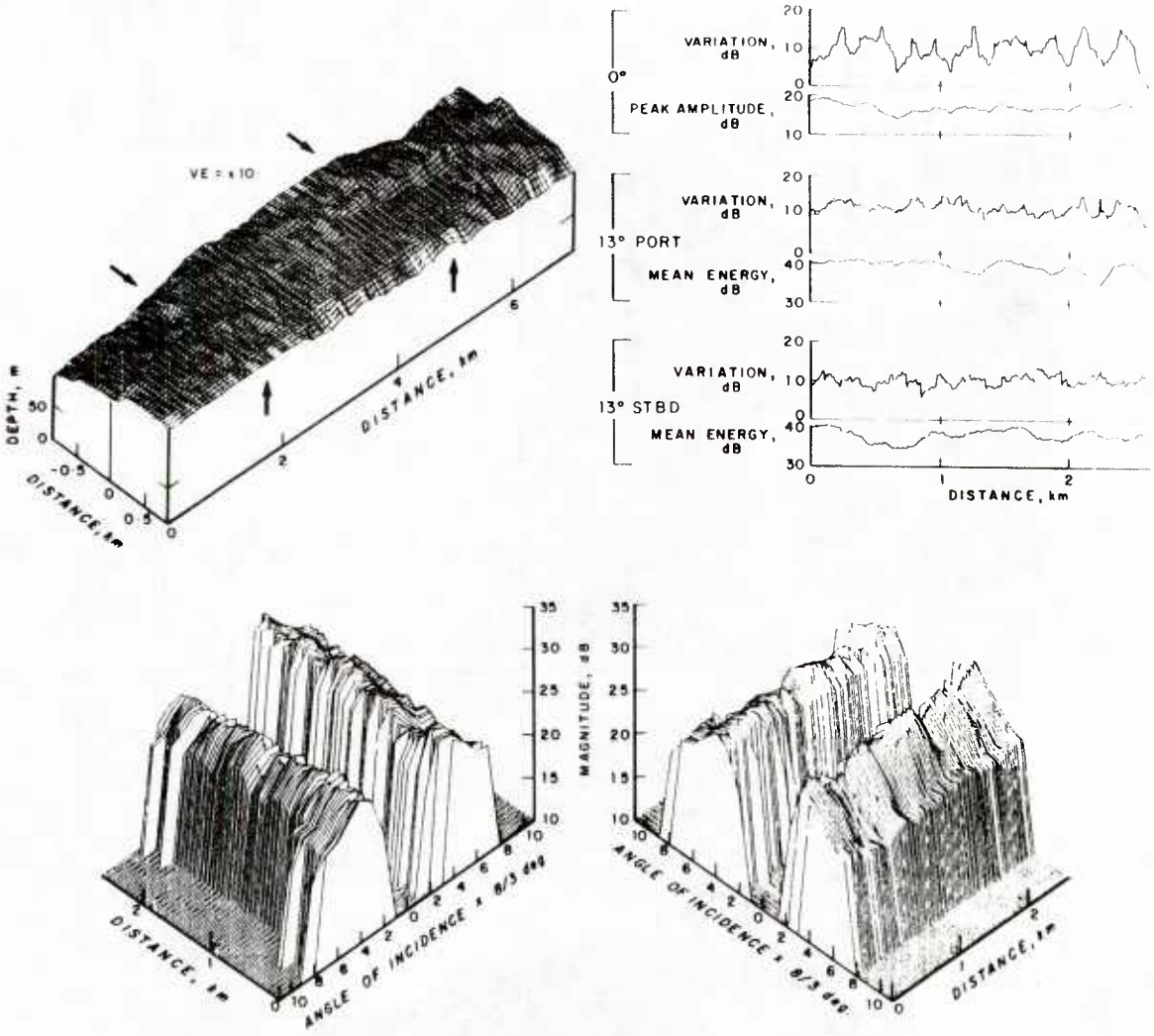

Figure 4.10 *Lava sheet flow on the crest of the East Pacific Rise: synopsis of Sea Beam data.* Layout and scales are identical to those of Figures 4.6 and 4.8. The origin of the depth scale is at 2700 m. The acoustic data displayed correspond to the section of bathymetry ($\sim$ 2.7 km long) delimited by the arrows. In this section, the bathymetry is nearly flat. For compactness of this figure, the origin (0) of the vertical axes for the acoustic data is not shown; however the scale is the same as in Figures 4.6 and 4.8.

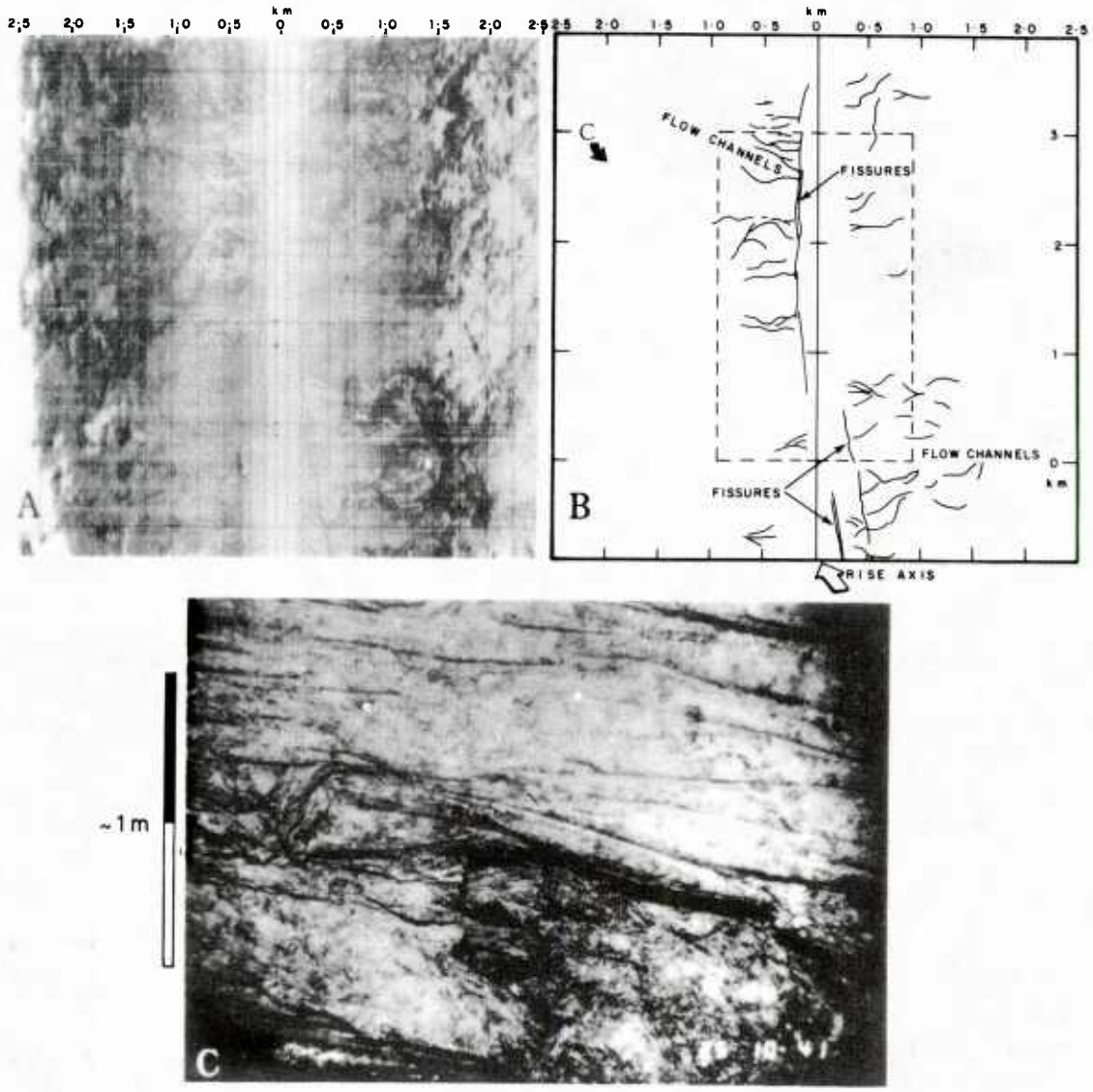

Figure 4.11 Sea MARC I side looking sonar image of the lava sheet flow (a). The swath covered by Sea Beam is delimited by the dotted line. On this image acoustic shadows are white and intense backscatter is black. Fissures and flow channels observable in this image are outlined in (b) where distance along-track originates at the same location as the 0 km point of the acoustic data in Figure 4.10. The arrow points to the location of the bottom photograph (c).

IV.5.1.c Rise crest environment

The acoustic data presented in Figure 4.10 corresponds to the section of bathymetry delimited by the arrows. In those bounds, the sea floor is nearly flat, with an average depth of 2560 m. With a 6 second ping rate and a ship speed of about 1 m/s, the along-track sampling interval is 6 m (compared to a footprint 120 m in diameter), and the averaging interval used for low-pass filtering of the data is 20 pings.

The same smoothing effect of large averaging intervals noted in the San Clemente basin data is seen here. However, peak amplitude variations are relatively higher indicating a greater variability in the raw data. Small trend changes over along-track distances 1 km or less are noticeable in the peak amplitude as well as in the total energy data. They can also be followed in the stacked profiles of total energy, which show no along-track symmetry about vertical incidence. In this case, relation of the acoustic data to the geological processes is facilitated by the uniqueness of the area and the availability of independent measurements made simultaneously with the Sea MARC I system.

This region of the East Pacific Rise around 10°05'N is characterized by nearly flat-lying basalt sheet flows covering an area over 10 km long and 3 km wide on the rise axis [Rise Axis Tectonic Team, 1983]. A 5 km segment from this area imaged with the Sea MARC I side-looking sonar system is shown in Figure 4.11a. On this image, acoustic shadows are white and intense backscatter is black. A line drawing (Fig 4.11b) of this image indicates fissures and flow channels observable in the sidescan data as well as in the area covered by the Sea Beam acoustic data considered here (dotted line). The basalts are fresh as evidenced by their glass coatings and the paucity of sediment seen in bottom photographs in the area (Fig. 4.11c). Patches of benthic organisms seen in the bottom photographs and temperature measurements

also indicate that this region of the rise axis is hydrothermally active [Rise Axis Tectonics Team, 1983].

The distribution of flow channels outlined inside the dotted line (Fig. 4.11b) coincides remarkably well with the pattern seen in the total-energy profiles (Fig. 4.10) at $\pm$ 13 degrees incidence ($\sim$ 590 m across track from the point of vertical incidence). Total energy is high between flow channel zones and drops upon crossing the zones. These flow channels appear in the side-scan image (Fig. 4.11a) as a lighter shade of grey than their surroundings, indicating reduced backscattering properties. Because this portion of seafloor is uniform in type (basalts) and nearly flat, the change in backscattering properties is most likely due to a change in the microroughness. We therefore conclude that in this area the acoustic backscatter is dominated by bottom microroughness.

IV.5.2 Angular dependence

Having isolated acoustically homogeneous areas of the seafloor by defining acoustic boundaries, one would like to use the acoustic data to identify the type of bottom within each area. Because Sea Beam measures acoustic backscatter simultaneously at sixteen angles of incidence spaced 2 2/3 degrees apart (usually over $\pm$ 20 degrees from vertical when the ship is not rolling), a discrete angular-dependence function is readily obtainable. This function is a potential criterion for differentiating between bottom types.

As mentioned previously, it has not been possible to obtain the complete angular dependence from the data presented here because of saturation and sidelobe interference. As a result, only the tails of the function are shown in Figure 4.12 for the three types of sea floor considered. In this figure, the levels indicated correspond to the relative total energy measured at each angle over flat, acoustically homogeneous regions and corrected for transmission loss.

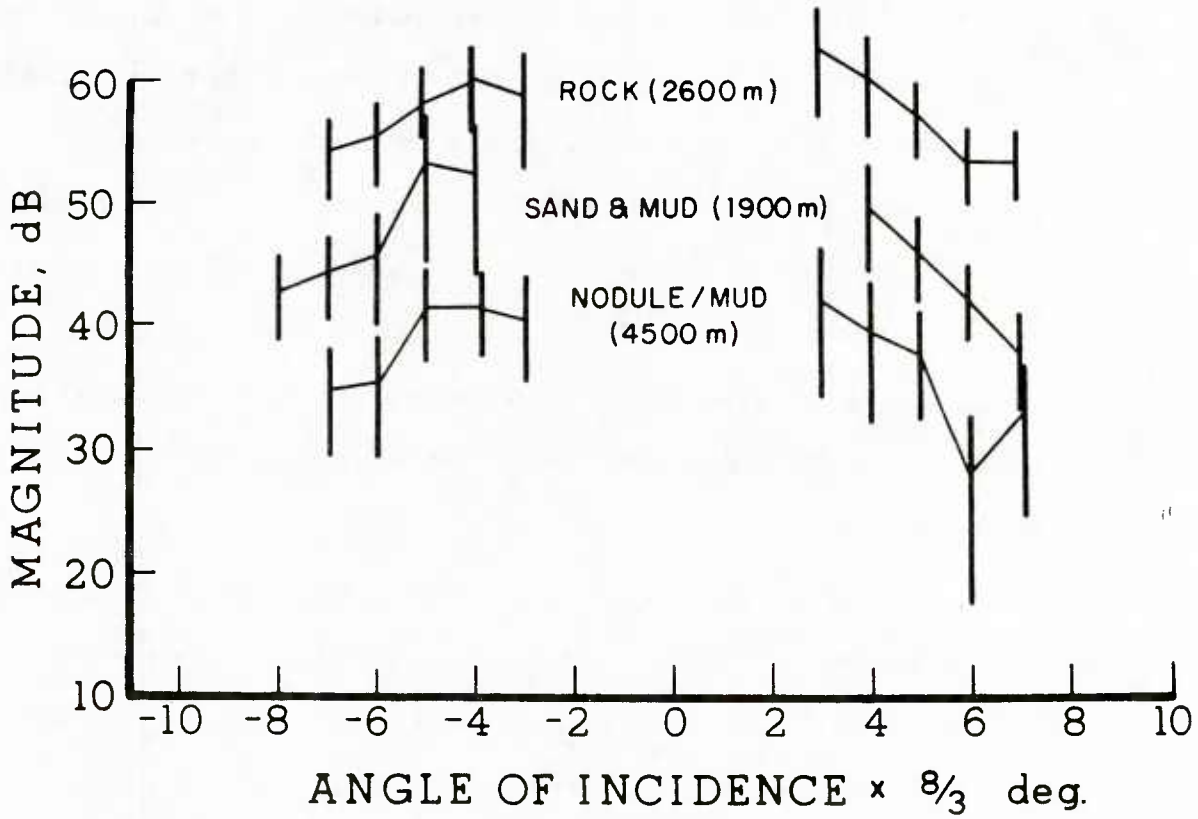

Figure 4.12 ***Angular dependence of total backscattered energy.*** The tails of the angular dependence function shown here for the three types of seafloor considered are remarkable for the differences in their energy level. However, their shapes are too similar to tell them apart on that criterion alone. Vertical bars represent 1 standard deviation about the mean value. The label "nodule/mud" corresponds to dense nodule coverage over a mud substrate, "sand and mud" indicates hemipelagic sediments found in the North San Clemente basin, and "rock" refers to basalts from the lava sheet flow on the East Pacific Rise at 10°N.

The tails of these three angular-dependence functions are mostly remarkable for the differences in their relative energy levels. Hemipelagic sediments (sand and mud) appear to be about 10 dB above nodules and 10 dB below basalts. Although very few deep sea data in the kilohertz range exist in the literature, these relative levels are in general agreement with comparable measurements in coastal locations summarized by Urick [1983]. In spite of the very different nature of the three areas considered, the shape of their partial angular-dependence function is similar (Fig. 4.12), and therefore cannot be used to identify them. Consequently, in our data the overall difference in levels between the bottom types is the only tangible criterion available on which to separate them. However, we are missing the information contained in the beams near normal incidence, which when expressed as the ratio of the specular backscattered energy to that of the adjacent nonspecular beams could prove a good indicator of the nature of the bottom.

To confirm this, a modification of the MPL Sea Beam acoustic data acquisition system is in progress to record both amplitude and phase of the backscattered signals. Sidelobe interference can then be removed without degrading the bottom return to produce a complete angular dependence function. Also, the availability of phase information gives access to coherent scattering measurements as described in Section IV.3, and yields a direct estimate of the bottom microroughness (Eq. 6).

IV.5.3 Estimates of Surface Statistics

In the present data set, we are restricted to echo envelope statistics for estimating parameters of the rough surface such as rms roughness and correlation area. For small to moderate relative roughness ($4k^2\sigma^2 \ll 1$), these parameters are directly related to the shape of the pdf of normal-incidence echo envelopes through the ratio γ of coherent to incoherent energy in the echo (Eq. 23 and 24). Estimates of γ are obtained by fitting a Rician distribution (Eq. 25) to the histogram of normal

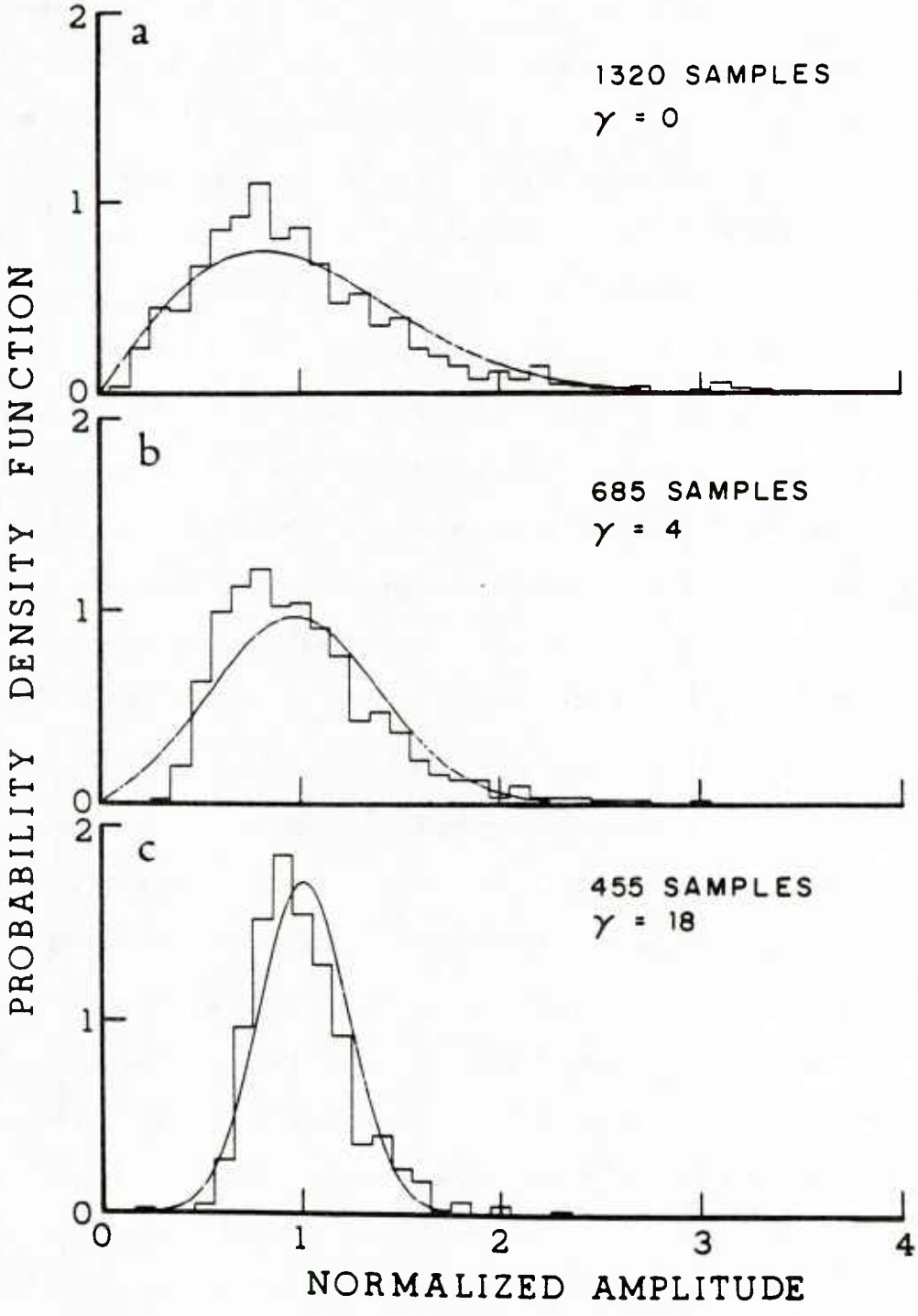

Figure 4.13 *Probability density functions of peak amplitude in the near-specular returns for the three types of seafloor.* (a) manganese nodule area, (b) sediments in the North San Clemente basin and (c) lava sheet flow on the crest of the East Pacific Rise. Histograms are from Sea Beam data. Superimposed curves represent the corresponding "best" fit of a Rician pdf with the parameter γ holding the values indicated in each case.

incidence echo peak amplitude. This method has the advantage of being independent of system calibration. Therefore peak-amplitude variations recovered from sidelobe levels (e.g. Fig. 4.5) can be used to produce a histogram. Three such histograms for the three areas under consideration are shown in Figure 4.13. The overlying curves represent the "best" fit, in a chi-square goodness of fit [Bendat and Piersol, 1971] sense, of a Rician distribution to the corresponding values of γ. The fit is not good in all three cases and a different distribution may yield a better fit, however the Rician distribution is the only one which relates to physical parameters. It is used here for this reason. The three areas yield markedly different values of γ, indicating differences in their roughness structure. We can estimate the rms roughness of each area from the bottom photographs and calculate an approximate correlation area by using Eq. 23 and the values of γ given in Figure 4.13. With Sea Beam $k = 2\pi/\lambda \simeq 51$ and $\Delta\phi = \Delta\chi = 2\ 2/3$ degrees so that at normal incidence $\alpha = \beta \simeq 2.8$ in Eq. 23.

In the manganese nodule area, $\gamma = 0$, indicating an infinitely rough surface according to Eq. 23. In fact, the rms roughness estimated from box cores and bottom photographs is about 2 cm [de Moustier, 1985b], and $4k^2\sigma^2 = 4.15 > 1$ so that the assumptions leading to Eq. 23 are violated. The surface can therefore be considered rough for our purposes. By comparison, $\gamma = 4$ for the North San Clemente basin data and $\gamma = 18$ for the basalt sheet flow, indicating relatively smoother surfaces. With these two values of γ, Eq. 23 yields $\sigma^2 l_1 l_2 = 2.03\ 10^{-6} m^4$ and $4.5\ 10^{-6} m^4$ respectively. If σ were the same for both regions, the correlation areas ($l_1 l_2$) would differ by a factor of 5, making it possible to tell the two types of bottom apart. Using the roughness (2 cm) in the nodule area as a photographic reference scale, it is reasonable to assume $\sigma < 1$ cm for the two other regions. This yields a lower bound on the correlation areas of $.203 m^2$ in the San Clemente basin and $.045\ m^2$ on the basalt sheet flow.

Both correlation areas support the assumptions which lead to Eq. 23. In the

San Clemente basin, the Gaussian assumption is justified because the surface microroughness is due mostly to animal activity and is therefore randomly distributed with many irregularities within the ensonified area. These irregularities are most likely isotropic so that $l_1 \simeq l_2 \simeq 45cm$. In the rise-crest data, the irregularities are presumably anisotropic. By analogy with current generated ripples, roughness in the direction perpendicular to the flow of lava probably has a longer correlation length than roughness parallel to the flow which is typically characterized by linear wrinkles (Fig. 4.11c). From bottom photographs taken in the general area, the spacing between wrinkles appears random, giving some justification for the Gaussian assumption. The limiting values required to satisfy $\alpha l_1^2 + \beta l_2^2 = 1$ in Eq. 21 given that $l_1 l_2 = .045m^2$ are $l_1 \simeq 60cm$ and $l_2 \simeq 7.5cm$. Although the value of the correlation area ($l_1 l_2$) is based on an empirical estimate of the rms roughness σ, the values obtained for l_1 and l_2 are consistent with the general roughness character observed in the area. It follows that in the limit $4k^2\sigma^2 \ll 1$ (rms roughness of the order of 1 cm or less at 12 kHz), two seafloor environments with the same rms roughness can be differentiated by their correlation area.

IV.6. CONCLUSIONS

Deep seafloor acoustic backscatter data measured with a Sea Beam system have been shown to hold a wealth of information on the nature of the seafloor surveyed. Acoustic boundaries are mapped over flat areas by following trend changes in acoustic data (peak amplitude at normal incidence and total energy otherwise) both along and across track. Clues to the nature of the bottom are found in the overall energy level of a partial angular-dependence function of backscattering as well as in the shape of the pdf of normal-incidence echo envelopes, which is related to the degree of coherence in the backscattered acoustic field.

Data from three geologically different environments (a manganese nodule field, a hemipelagic sedimentary basin, and a rise-crest basalt sheet flow) have been analyzed and validated with independent measurements (bottom photographs and side-looking sonar data). The backscattering process seemed to be more sensitive to bottom type in the manganese nodule area, to bottom roughness in the rise-crest data, and to a combination of both in the sedimentary basin. Total energy in the partial angular-dependence function was highest for basalts on the rise crest; it was roughly 10 dB lower for hemipelagic sediment in San Clemente basin and another 10 dB lower for manganese nodules.

The shape of the pdf of echo envelopes was indicative of a rough surface in the manganese nodule area, and of smoother surfaces in the two other environments. This was confirmed by bottom photographs. When given the same roughness, the sedimentary basin and the rise-crest sheet flow were found to have quite different correlation areas. For small relative roughness ($4k^2\sigma^2 \ll 1$) the correlation area is therefore a useful parameter to differentiate between seafloor types having the same roughness.

IV.7. ACKNOWLEDGMENTS

Funds for this research were provided by the Office of Naval Research (Contract No. N00014-79-C-0472). Data collection at sea was made possible through the cooperative efforts of the officers, crew and scientific parties of R/V Thomas Washington during expeditions CERES Leg 1 and PASCUA Leg 1 and 5. The author wishes to thank K. Crane for making Sea MARC I data available and providing helpful comments, V. C. Anderson, F. N. Spiess, C. W. Helstrom, E. L. Winterer and D. Alexandrou for valuable suggestions, R. C. Tyce for initiating the Sea Beam acoustic backscatter experiment at MPL, and F. V. Pavlicek for his support during the development of the MPL Sea Beam acoustic data acquisition system. He is also grateful to E. Ford for typing and editing and J. Griffith for the art work.

IV.8. APPENDIX : Envelope distributions

For surfaces rough compared to an acoustic wavelength, the phase of the backscattered echo is to a good approximation distributed uniformly over the interval (0,2π), and the set of pressures received can be assumed to be normally distributed with variance σ_p^2. From the central limit theorem, this approximation is better as the set gets larger ($\gtrsim$30). Under such conditions, the amplitude E of the echo as defined in Eq. (1) in the text, has been shown [Ol'shevskii, 1967; Proud et al., 1960] to be Rayleigh distributed with a pdf:

$$W(E) = \frac{E}{\sigma_p^2} \exp\left(-\frac{E^2}{2\sigma_p^2}\right) \tag{A1}$$

The various moments of E are by definition:

$$<E^n> = \int_{-\infty}^{+\infty} E^n \; W(E) dE \tag{A2}$$

from which, after substitution of Eq. (A1), we obtain the second moment:

$$<E^2> = 2\sigma_p^2. \tag{A3}$$

The Rayleigh pdf can then be expressed in terms of the amplitude of the echo envelope E and its mean square value $<E^2>$ two quantities readily measurable in our data.

$$W(E) = \frac{2E}{<E^2>} \exp\left(-\frac{E^2}{<E^2>}\right). \tag{A4}$$

The generalized Rayleigh distribution or Rice distribution [Rice, 1945] has been used also to describe the effects of coherent scattering on the pdf of the echo envelope [Ol'shevskii, 1967; Stanton, 1984]. In this case, the backscattered pressure wave is considered as the sum of a coherent component of rms value A and an incoherent component normally distributed with variance σ_p^2, respectively analogous to the sine wave and the narrow-band Gaussian noise of the original Rician distribution.

The corresponding echo envelope E is distributed with a pdf:

$$W(E) = \begin{cases} \frac{E}{\sigma_p^2} \exp\left(-\frac{E+A^2}{2\sigma_p^2}\right) I_o\left\{\frac{EA}{\sigma_p^2}\right\} & E \geq 0 \\ 0 \quad \text{otherwise} \end{cases} \tag{A5}$$

where I_o is the zeroth order modified Bessel function. Remembering Eq. (A2), the moments of E are given by

$$<E^n> = (2\sigma_p^2)^{\frac{n}{2}} \Gamma\left(\frac{n}{2}+1\right) {}_1F_1\left(-\frac{n}{2}; 1, -\frac{A^2}{2\sigma_p^2}\right) \tag{A6}$$

For even order moments, the confluent hypergeometric function ${}_1F_1$ (-n; 1,nr) is equal to the n^{th} Laguerre polynomial [Helstrom, 1968]

$$L_n(r) = \sum_{i=1}^{n} (-r)^i \frac{n!}{(i!)^2(n-i)!} \tag{A7}$$

Therefore the second moment of E is

$$<E^2> = 2\sigma_p^2 + A^2 \tag{A8}$$

To express the Rician distribution in terms of readily measurable quantities, it is convenient to define a parameter

$$\gamma = \frac{A^2}{\sigma_p^2} \tag{A9}$$

which is the coherent to incoherent power ratio in the echo. Substitution of Eq. (A8) and (A9) into (A5) yields:

$$W(E) = (2+\gamma)\frac{E}{<E^2>} \exp\left[-\frac{(2+\gamma)E^2 + \gamma<E^2>}{2<E^2>}\right] I_o\left[\frac{E}{<E^2>^{1/2}} (\gamma(2+\gamma))^{1/2}\right] \tag{A10}$$

when $\gamma \ll 1$, Eq. (A10) tends to the Rayleigh distribution

Eq. (A4) conversely, when $\gamma \gg 1$ Eq. (A10) tends to a Gaussian-like distribution:

$$W(E) \simeq \left[\frac{\gamma X}{2\pi < E^2 >}\right]^{1/2} \exp\left[-\frac{\gamma (X-1)^2}{2}\right]$$

$$\text{with } X = \frac{E}{< E^2 >^{1/2}} \tag{A11}$$

since $I_o(Z)$ tends to $(2\pi Z)^{-1/2}\, e^Z$ when Z tends to infinity.

IV.9 REFERENCES

Bass F. G. and I. M. Fuks, *Wave scattering from statistically rough surfaces,* Pergamon Press, 1979.

Beckmann P. and A. Spizzichino, *The scattering of electromagnetic waves from rough surfaces,* Pergamon Press, 1963.

Bendat J. S. and A. G. Piersol, *Random Data: analysis and measurement procedures,* Wiley-Interscience, 1971.

Born M. and E. Wolf, *Principles of Optics,* Pergamon Press, 1970. 4th edition.

Brekhovskikh L. and Yu Lysanov, *Fundamentals of ocean acoustics, Chapter 9,* Springer-Verlag, 1982.

Clay C. S., Coherent reflection of sound from the ocean bottom, *J. Geol. Res., 71,* 2037-2046, 1966.

Clay C. S. and W. K. Leong, Acoustic estimates of topography and roughness spectrum of the sea floor southwest of the Iberian penninsula, in *Physics of sound in marine sediments,* pp. 373-445, Plenum Press, 1974.

Clay C. S. and H. Medwin, Chapter 10 and Appendix 10, in *Acoustical Oceanography: Principles and Applications,* Wiley Interscience, 1977.

Dolph C. L., A current distribution of broadside arrays which optimizes the relationship between beam width and side-lobe level, *Proc. Inst. Radio Engrs., 34,* 335-348, 1946.

Eckart C., The scattering of sound from the sea surface, *J. Acoust. Soc. Am., 25,* 566-570, 1953.

Emery K. O., *The sea off southern California - a modern habitat of petroleum,* John Wiley & Sons, Inc., New York, 1960.

Faure P., Theoretical model of reverberation noise, *J. Acoust. Soc. Am., 36,* 259-266, 1964.

Goodman J. W., Statistical properties of laser speckle patterns, in *Laser Speckle and Related Phenomena,* edited by J. C. Dainty, pp. 9-75, Springer-Verlag, 1975.

Helstrom C. W., *Statistical theory of signal detection, 2nd Ed.,* Pergamon Press, 1968.

Horton C. W., A review of reverberation, scattering and echo structure, *JASA, 51,* 1049-1061, 1972.

Kosalos J. G. and D. N. Chayes, A portable system for ocean bottom imaging and charting, *Proc. Oceans '83,* 649-656, 1983.

Eq. (A4) conversely, when $\gamma \gg 1$ Eq. (A10) tends to a Gaussian-like distribution:

$$W(E) \simeq \left[\frac{\gamma X}{2\pi < E^2 >}\right]^{1/2} \exp\left[-\frac{\gamma(X-1)^2}{2}\right]$$

$$\text{with } X = \frac{E}{< E^2 >^{1/2}} \tag{A11}$$

since $I_o(Z)$ tends to $(2\pi Z)^{-1/2}\, e^Z$ when Z tends to infinity.

IV.9 REFERENCES

Bass F. G. and I. M. Fuks, *Wave scattering from statistically rough surfaces,* Pergamon Press, 1979.

Beckmann P. and A. Spizzichino, *The scattering of electromagnetic waves from rough surfaces,* Pergamon Press, 1963.

Bendat J. S. and A. G. Piersol, *Random Data: analysis and measurement procedures,* Wiley-Interscience, 1971.

Born M. and E. Wolf, *Principles of Optics,* Pergamon Press, 1970. 4th edition.

Brekhovskikh L. and Yu Lysanov, *Fundamentals of ocean acoustics, Chapter 9,* Springer-Verlag, 1982.

Clay C. S., Coherent reflection of sound from the ocean bottom, *J. Geol. Res., 71,* 2037-2046, 1966.

Clay C. S. and W. K. Leong, Acoustic estimates of topography and roughness spectrum of the sea floor southwest of the Iberian penninsula, in *Physics of sound in marine sediments,* pp. 373-445, Plenum Press, 1974.

Clay C. S. and H. Medwin, Chapter 10 and Appendix 10, in *Acoustical Oceanography: Principles and Applications,* Wiley Interscience, 1977.

Dolph C. L., A current distribution of broadside arrays which optimizes the relationship between beam width and side-lobe level, *Proc. Inst. Radio Engrs., 34,* 335-348, 1946.

Eckart C., The scattering of sound from the sea surface, *J. Acoust. Soc. Am., 25,* 566-570, 1953.

Emery K. O., *The sea off southern California - a modern habitat of petroleum,* John Wiley & Sons, Inc., New York, 1960.

Faure P., Theoretical model of reverberation noise, *J. Acoust. Soc. Am., 36,* 259-266, 1964.

Goodman J. W., Statistical properties of laser speckle patterns, in *Laser Speckle and Related Phenomena,* edited by J. C. Dainty, pp. 9-75, Springer-Verlag, 1975.

Helstrom C. W., *Statistical theory of signal detection, 2nd Ed.,* Pergamon Press, 1968.

Horton C. W., A review of reverberation, scattering and echo structure, *JASA, 51,* 1049-1061, 1972.

Kosalos J. G. and D. N. Chayes, A portable system for ocean bottom imaging and charting, *Proc. Oceans '83,* 649-656, 1983.

Middleton D., A statistical theory of reverberation and similar first-order scattered fields - Part I: Waveforms and general process; Part II: Moments, spectra and special distributions, *IEEE Trans. Information Theory, IT-13,* 372-414, 1967.

de Moustier C., A Sea Beam acoustic data acquisition system, MPL TM-379, Marine Physical Laboratory, Scripps Institution of Oceanography, San Diego, CA., 1985a.

de Moustier C., Inference of manganese nodule coverage from Sea Beam acoustic backscattering data, *Geophysics, 50,* 989-1001, 1985b .

de Moustier C. and M. C. Kleinrock, Bathymetric artifacts in Sea Beam: How to recognize them, what causes them, *JGR,* in press.

Normark W. R. and D. J. W. Piper, Sediments and growth pattern of Navy deep-sea fan, San Clemente basin, California borderland, *J. Geol., 80,* 198-223, 1972.

Novarini J. C. and J. W. Caruthers, The degree of coherence of acoustic signals scattered at randomly rough surfaces, *J. Acoust. Soc. of Am., 51,* 417-418, 1972.

Ol'shevskii V. V., *Characteristics of sea reverberation,* Plenum Press, Ed. Consultant Bureau, 1967.

Papoulis A., *Probability, random variables, and stochastic processes,* McGraw-Hill, 1965.

Proud J. M., R. T. Beyer, and P. Tamarkin, Reflection of sound from randomly rough surfaces, *J. Appl. Phys., 31,* 543-552, 1960.

Renard V. and J. P. Allenou, Sea Beam multi-beam echo-sounding in "Jean Charcot" Description, evaluation and first results, *International Hydrographic Review, LVI(1),* 35-67, Monaco, 1979.

Rice S. O., Mathematical analysis of random noise Part III, *Bell System Tech. Journ., 24,* 46-156, 1945.

Rise Axis Tectonic Team, An along strike Sea Beam and Sea Marc I perspective of the axis of the East Pacific Rise: Implications for the accretion of oceanic lithosphere, *International Lithosphere Congress, Texas A&M Univ.,* 1983.

Spiess F. N. and P. F. Lonsdale, Deep Tow Rise Crest exploration techniques, *Mar. Tech., 16,* 67-75, 1982.

Stanton T. K., Sonar estimates of microroughness, *J. Acoust. So. Am., 75,* 809-818, 1984.

Tolstoy I. and C. S. Clay, Chapter 6, in *Ocean Acoustics Theory and experiment in underwater sound,* McGraw-Hill, 1966.

Urick R. J., *Principles of underwater sound (3rd ed.),* McGraw-Hill, 1983.

Appendix

A SEA BEAM ACOUSTIC DATA ACQUISITION SYSTEM

A.1 INTRODUCTION

In the last quarter of 1981, a Sea Beam bathymetric survey system was installed aboard the R/V *Thomas Washington* of the Scripps Institution of Oceanography (SIO). The system is a multibeam echo-sounder manufactured by General Instrument Corporation and its main function is to generate contour maps of the ocean floor in near-real time.

It is believed that more information is contained in the acoustic signals returned from the ocean floor than is necessary for contour mapping. However, these signals are discarded by the system once depth determination has been achieved. In order to take greater advantage of Sea Beam's capabilities SIO's Marine Physical Laboratory devised a parallel acoustic data acquisition system which saves the Sea Beam detected echoes before they reach the processing stage. This paper describes briefly the Sea Beam system and presents the method used to record the echo envelopes it detects.

A.2 THE SEA BEAM SYSTEM

The Sea Beam bathymetric survey system comprises two major subsystems: a narrow beam echo-sounder (NBES), and an echo-processor (EP). The narrow beam echo-sounder uses sixteen 2 2/3 degree beams to measure water depth across the ship's track. The swath thus obtained on the seafloor has a width roughly equal to three quarters of the water depth. The echo-processor uses a mini-computer as a central control and processing element, providing for automatic control of the system. Figure A.1 is a block diagram describing the functional interfaces of the Sea Beam.

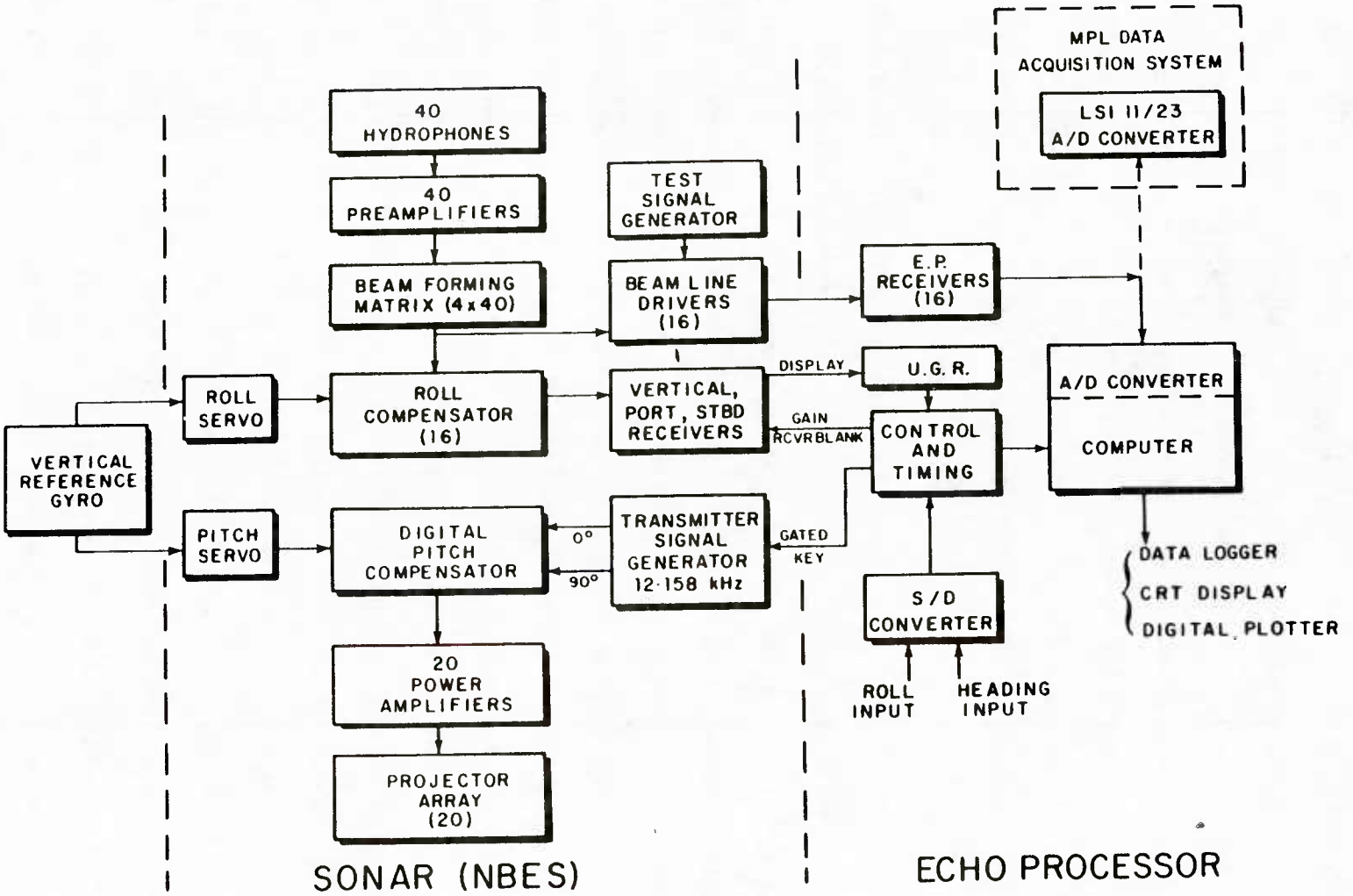

Figure A.1 *Block diagram of the Sea Beam system showing the Narrow Beam Echo Sounder and the Echo Processor.* The position of the MPL data acquisition system is shown for reference.

The sonar signal originates in the transmitter signal generator which produces two low impedance 12.158 kHz sinewaves in quadrature. A gated key pulse 7ms wide is produced by the timing unit in the echo-processor module. A Universal Graphic Recorder (UGR) usually determines the ping period. The signal is fed into a digital pitch compensator which steers the transmitted beam pattern by varying the phase of the signal fed into each of the twenty power amplifiers relative to a pitch angle from the vertical reference gyroscope. This insures vertical projection of the sonar transmission within the limits of ± 10 degrees of pitch with a quarter of a degree of accuracy.

Each power amplifier drives one of the twenty transducers in the projector array. This array is mounted along the ship's keel and is roughly 2.8 m long by 0.16 m wide. Figure A.2a shows that the corresponding theoretical transmit beam pattern is 54 degrees wide athwartship and 2 2/3 degrees wide in the fore-aft direction. The sidelobes are attenuated 30 dB below the main lobe by adjusting the power output of the amplifiers. The receiving unit is a V-shaped 40 element line hydrophone array centered on the ship's keel. It measures about 2.8 m athwartships and 0.4 m fore-aft. The corresponding theoretical beam pattern is 2 2/3 degrees wide athwartships by 20 degrees in the fore-aft direction (Fig. A.2b). The preamplifiers associated with each hydrophone create four quadrature outputs (45, 135, 225 and 315 degrees). The resulting 160 signals are fed into a resistors matrix which steers the 2 2/3 by 20 degree beam in the athwartships plane to form sixteen beams within + 20 and - 20 degrees of the ship's vertical axis. The sidelobes are attenuated 30 dB below the mainlobe by adjusting the signal amplitudes in the resistors matrix.

The combination of the projector and receiver array beam patterns outlines on the seafloor sixteen squares 2 2/3 degrees on a side, in a vertical plane through the ship's fore-aft axis, but roll dependent athwartships (Fig. A.2c).

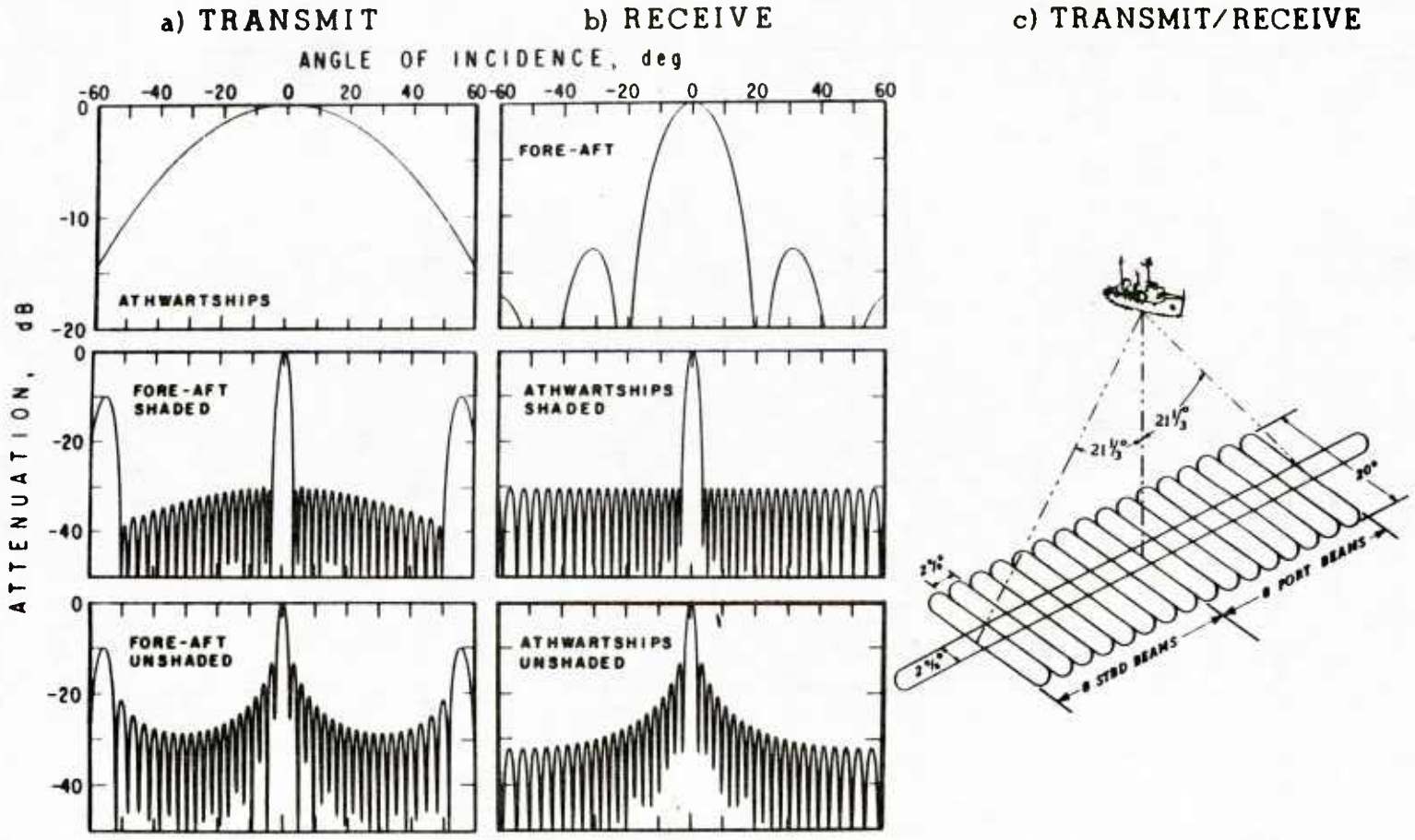

Figure A.2 *Sea beam transmit/receive geometry.* Computed beam pattern cross-sections in the athwartships vertical plane centered on the array and in the vertical plane passing through the ship's fore-aft axis are shown for (a) the projector array, (b) the receiver array. The effect of Dolph-Chebyshev amplitude shading is also illustrated. (c) is a summary cartoon showing the angular relationship between the mainlobe of the transmitted beam pattern and those of the sixteen preformed beams.

Beams are numbered from the keel out: 1 to 8 for both port and starboard. The sixteen beams are sent on one hand to the echo-processor receivers, via the beam line drivers which act as buffers between the sonar and the receivers; and on the other hand to the NBES roll-compensator.

In response to a roll signal from the vertical reference gyroscope, within the limits of $\pm$ 20 degrees and with an accuracy of a quarter of a degree, sixteen beams are compensated for roll. As an example of the roll effect, a 20 degree roll to port results in port beam number 8 looking directly below the ship. This beam will be the vertical beam, and no echoes will show on port side.

The roll-stabilized echo signals go to the NBES receivers. These are three identical receivers (port, center, starboard) whose function is to detect, filter, amplify and compress the dynamic range of the echo, while maximizing the signal to noise ratio with band-pass filters.

The control unit of the echo-processor sets the gain of these receivers, and gates them off (rec. blank, in Figure A.1) during a sonar ping and its reverberation. It is also possible to output a depth profile on the UGR by selecting one or a combination of these receivers.

In the echo-processor, the signals (not roll-compensated) coming from the sonar line drivers are fed into sixteen identical receivers. Each receiver has a narrow band amplifier centered at 12.158 kHz, a detector and a DC amplifier. The echo-processor receivers output linear detected signals which are sent to the analog-to-digital (A/D) converter in the computer.

The computer also receives roll and heading inputs through a synchro-to-digital (S/D) converter and performs the various corrections such as: ray bending, receiver gain correction, roll-compensation, slant-range calculation, etc. The computer does the depth determination and keeps track of the bottom by setting up

self-adjusting gates above and below the instantaneous cross-track bottom profile. The final product is a set of depths and horizontal distances across the ship's track which are subsequently used to generate contour maps. More extensive descriptions of the Sea Beam system and its echo-processing methods may be found in Renard and Allenou (1979), in Farr (1980) and in de Moustier and Kleinrock (1985).

A.3 A Parallel Acoustic Data Acquisition System

Because Sea Beam does not preserve the bottom backscattered acoustic signals it receives, and because these signals contain information about the nature of the seafloor, it was necessary to build a parallel acoustic data acquisition system to record them for later analysis.

The approach taken consists in recording the detected echo envelopes of Sea Beam's sixteen beams at the output of the EP receivers (Fig. A.1). The data acquisition system is build around a DEC LSI 11/23 minicomputer with at least 64 kw of memory. The various components of the system and their interface with Sea Beam are illustrated in the block diagram of Figure A.3.

The analog detected signal envelopes are tapped at the output of the EP receivers along with a time-varying gain (TVG) which is applied to the receivers to compensate for acoustic transmission loss through the water column. The seventeen channels are sent via buffer amplifiers (Fig. A.4) to a multichannel 12 bit A/D converter with direct memory access (DMA). The buffer amplifiers' function is to minimize interferences with the Sea Beam system. In addition, the ship's instantaneous roll angle is sampled from the vertical reference gyroscope by a S/D converter. The resulting eighteen digitized channels (16 beams, TVG and roll) are accumulated in a memory buffer until the bottom echo reception cycle is completed. When the reception cycle is completed, the buffer is written on a standard 9-track magnetic tape in a DMA operation Meanwhile, the digitized data from one of the eighteen channels is

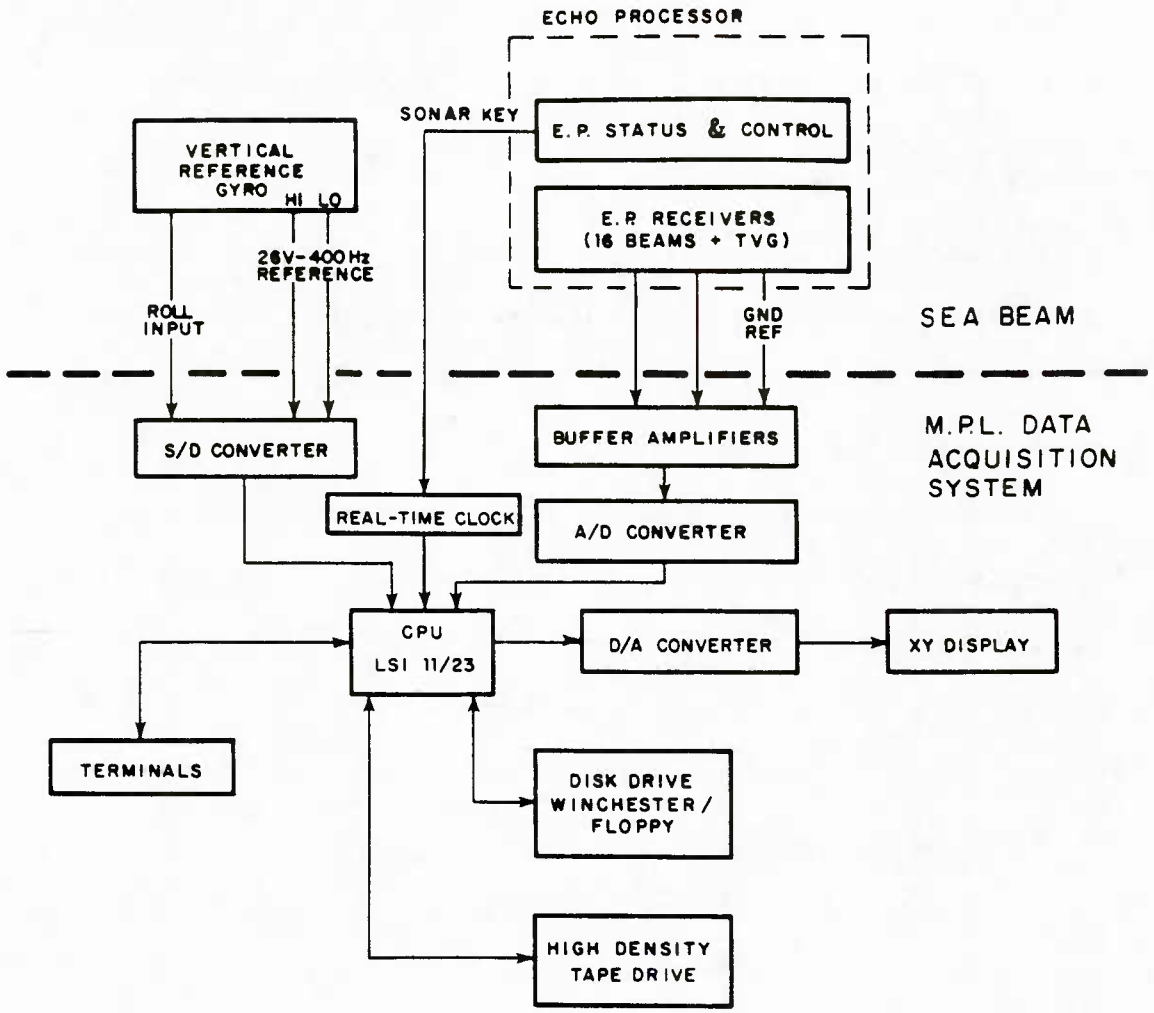

Figure A.3 *Block diagram of the MPL Sea Beam acoustic data acquisition system.*

transferred by DMA into a digital-to-analog converter which drives an xy display oscilloscope. Outputting a selected channel on the oscilloscope allows the operator to monitor the proper functioning of the data acquisition system and the performance of its bottom tracking algorithm. Should an external sound source interfere with Sea Beam's reception cycle, the interference would be observable in the display so that the operator would know when corrective action (e.g. phase the interfering sound source out of Sea Beam's reception cycle) is required.

In Figure A.5 a simplified timing diagram indicates the sequence of events taking place during data acquisition. The timing reference for this sequence is the sonar key pulse which is taken from the echo-processor in Sea Beam. Upon a sonar key pulse, the timer of an accurate (0.01%) real-time clock is loaded with a delay corresponding to the time required for sound to travel from the ship to the bottom and back. When the timer has counted down to zero, it sends an interrupt to the LSI 11/23 central processing unit (CPU) which triggers the digitizing sequence. The digitization rate is about 10 kHz for eighteen channels so that for any one channel samples are approximately 1.8 ms apart. The CPU is interrupted each A/D conversion scan cycle to take in the ship's roll data from the S/D converter.

At the end of the digitizing sequence, bottom tracking is performed by detecting the first digitized sample which exceeds a preset threshold in the set of sixteen beams. The position of this sample inside the digitization window is compared with the ideal position for which all of the returns fall within the window. Discrepancies between these two positions are resolved by adjusting the delay time between the sonar key pulse and the onset of digitization.

The digitized data is then written to tape while one of the channels is also loaded into the xy display. Both operations are done DMA. The CPU spends the remaining time waiting for the next sonar key pulse and the above sequence repeats.

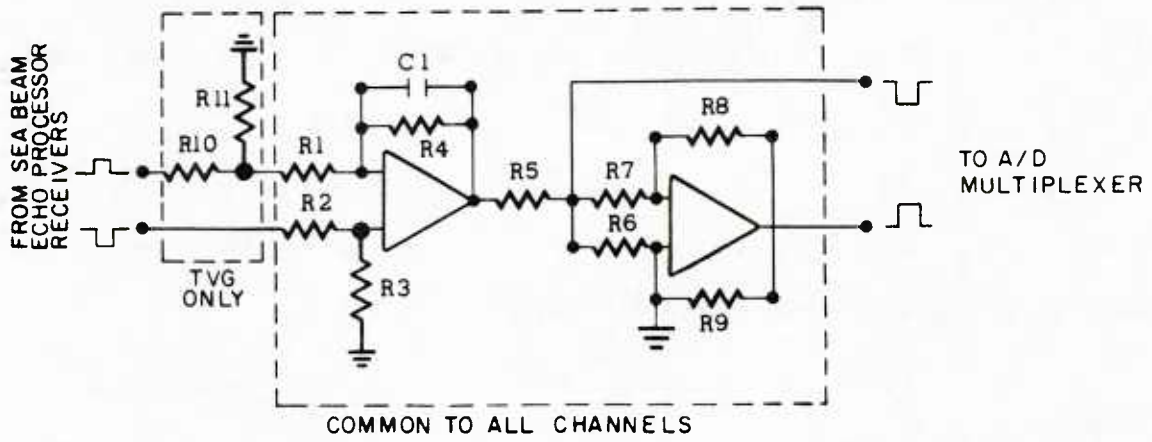

Figure A.4 *Buffer amplifier schematic.*

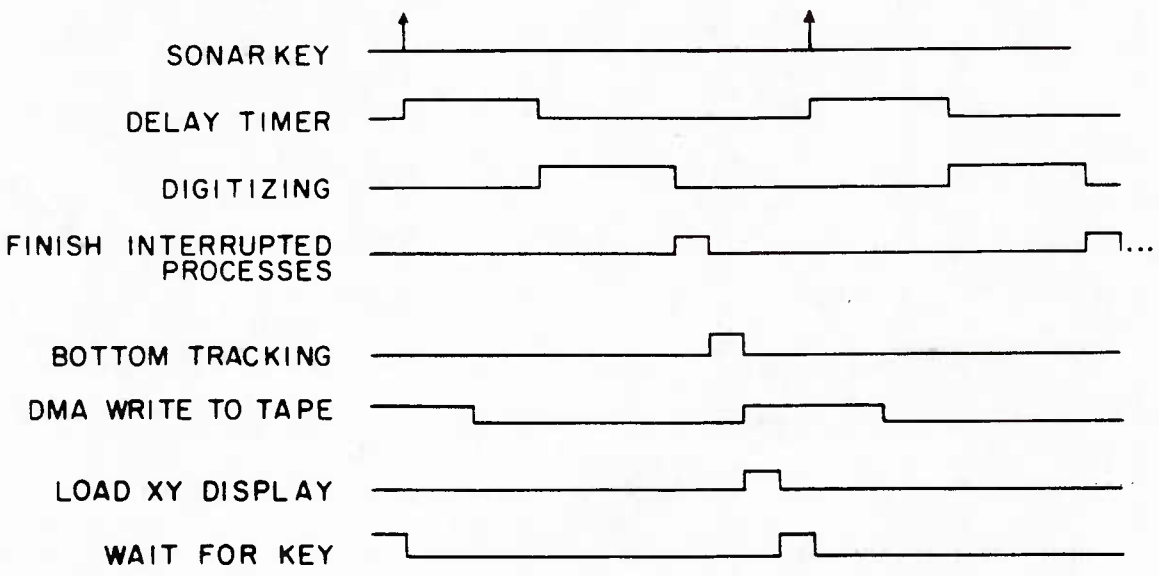

Figure A.5 *Data acquisition timing diagram.*

Double buffering in memory is used to avoid overwriting buffers during a transfer to tape. By this method one buffer fills up with data during digitization while the other is being written on tape.

The data are written on tape sequentially. Each tape record corresponds to one Sea Beam reception cycle and contains 14408 words (8 word header + 800 words x 18 channels). The record header is formated as follows:

word 0:	number of words in buffer
word 1:	record number (sequential from start of tape)
word 2:	tape error status for previous record
word 3:	digitization rate (bit 15-12), conversion gain (bit 11-9), first A/D multiplexer channel to be digitized.
word 4:	delay from key pulse to start of digitizing in increments of 10 ms
word 5:	seconds of start of digitization
word 6:	hour-minute of start of digitization
word 7:	date (day-month-year). Word 5 through 7 are read into memory from a time-of-day clock once per Sea Beam reception cycle.
word 8-23	= 16 beams
word 24	= TVG
word 25	= roll
word 26-42	= 16 beams
word 43	= TVG
word 44	= roll
----	for 800 iterations.

With this format approximately 2950 records fit on a 2400 ft. reel of 9-track standard magnetic tape recorded at 3200 bits per inch (BPI). Recording time per tape varies

with the key pulse repetition rate which depends on the water depth. Provision has been made in the data acquisition software to allow a certain number of reception cycles not to be recorded on tape if desired. The tape consumption may therefore vary depending on the number of reception cycles skipped.

Initial post-processing operations

The Sea Beam acoustic data recorded on tape are referenced to the ship's vertical whose orientation varies with the roll of the ship. To compare data from successive reception cycles, it is therefore convenient to roll-compensate the recorded data so as to reference them to the true vertical. In addition, because the EP receivers have inherent gain differences between them, beam to beam comparisons require correcting the amplitudes of the recorded data by establishing a gain reference common to the sixteen beam channels. This gain correction and the roll-compensation are common to most post-processing applications of the recorded data. For this reason they are outlined in the following.

Every half hour the Sea Beam system calibrates the relative gains of the EP receivers by injecting a signal from the test signal generator (Fig. A.1). This is not an absolute calibration for the echo-processor only seeks to compensate for gain differences among the individual receivers. The test signal is not constant through time at the input to the receivers because it is multiplied by the inverse of the TVG which compensates the detected echoes for transmission loss during normal echo-sounding operation. This results in a nearly constant signal level at the output of each individual receiver. For this reason it is possible to approximate the relative gain on any one digitized receiver output by the mean amplitude observed over the digitizing time window. The data recorded on tape has been digitized by a 12 bit A/D converter scaled in the range 0 to 10 volts. An arbitrary level of 2.5 volts (1024 A/D units) was selected as the reference level to which individual receiver gains would be

adjusted. 2.5 volts corresponds roughly to the mean amplitude observed across all sixteen beams during a calibration cycle. For each digitized beam channel, a receiver gain correction coefficient is calculated as the ratio of the reference level (2.5 volts) to the mean amplitude observed on that channel during a calibration cycle. In subsequent processing of the recorded acoustic data, the digitized samples for each of the sixteen beams are multiplied by the corresponding gain correction coefficients thereby giving them a common reference.

Gain homogeneity across all sixteen beam channels is important during the roll-compensation process because this process involves interpolation between beams. Ideally, before roll-compensation a refraction correction should be applied to determine the true angles of arrival of the received beams with respect to the ship's vertical. Because of the computational advantage of constant received beam spacing and because angular variations due to refraction are small for small angles of incidence, the refraction correction is omitted in the following.

Figure A.6 illustrates the roll-compensation process. The sixteen received beams are fixed with reference to the ship's vertical axis, labeled "keel" in Figures A.6, and the angle between this axis and the true vertical is the ship's roll angle. These beams are placed in an array of fixed stabilized beams spaced 2 2/3 degrees apart, one of which points vertically down. Each stabilized beam is created by linear interpolation between the two received beams closest to its direction. With a zero roll angle, such a scheme creates fifteen stabilized beams: one vertical beam and seven on either side.

For computing purposes, received beams are numbered 1 to 16 from port to starboard. In the example of Figure A.6, the roll-stabilized array contains twenty three beams numbered 1 to 23 from port to starboard, and beam 12 lies on the vertical. By comparison with the fifteen stabilized beams mentioned above,

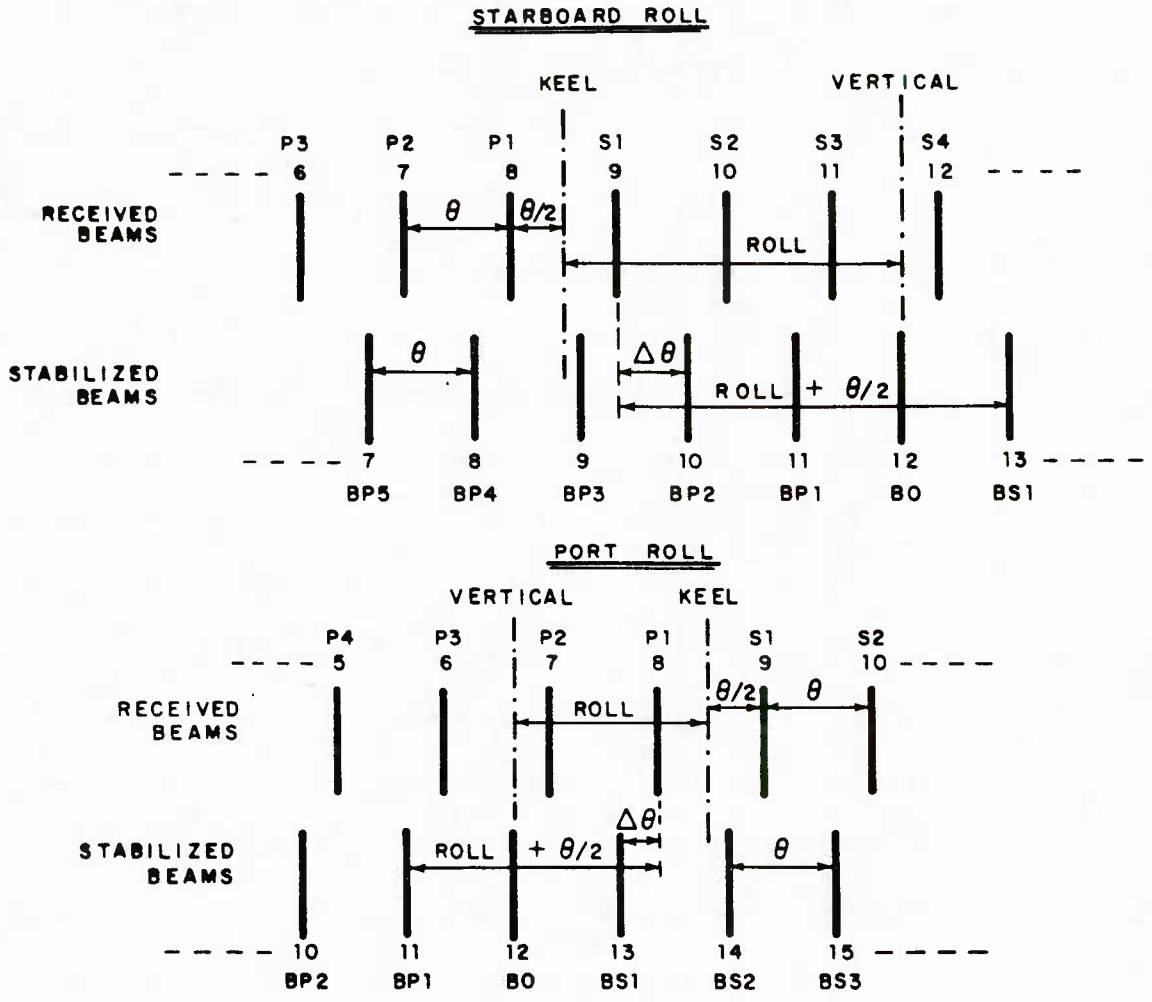

Figure A.6 *Roll-compensation diagram.*

this corresponds to four additional beams on either side of vertical, allowing for roll angles of 4 x 2-2/3 = 10-2/3 degrees to port or starboard. Greater roll angles can be accommodated by adding more beams to the stabilized array. The terms entering in the roll-compensation algorithm are defined as follows:

θ	= nominal beam spacing (2 2/3 degrees)
roll	= ship's roll angle measured by the vertical reference gyroscope
B(I), I = 1, 16	= amplitudes of received beams
SB(J), J = 1, 2M+15	= interpolated amplitudes of stabilized beams
M	= number of additional beams on either of vertical in the stabilized array (M = 4 in Fig. A.6)

Referring to Figure A.6, the offset between a given received beam and its stabilized counterpart is expressed as an integer number of beam spacings:

$$N = integer\left(\left[roll + \theta/2\right]/\theta\right),$$

plus a fractional remainder:

$$\Delta\theta = \left[roll + \theta/2\right] - N\theta$$

Depending on the direction of roll, received beams are shifted right or left relative to the stabilized array. The offset in the stabilized beams indexing is determined accordingly.

A starboard roll corresponds to an index offset of K = M - N in the stablized array. The stabilized beams are then calculated by linear interpolation:

$$SB(K+I) = B(I)\left[\frac{\theta - \Delta\theta}{\theta}\right] + B(I+1)\left[\frac{\Delta\theta}{\theta}\right], \quad I = 1, 15$$

$$SB(J) = 0, \quad J = 1, K; \quad K \neq 0$$

$$SB(J) = 0, \quad J = K+16, 2M+15; \quad K \neq 2M-1$$

Likewise for a port roll, the index offset is $K = M + N$ and the linear interpolation yields:

$$SB(K+I) = B(I)\left[\frac{\Delta\theta}{\theta}\right] + B(I+1)\left[\frac{\theta - \Delta\theta}{\theta}\right], \quad I = 1, 15$$

$$SB(J) = 0, \quad J = 1, K; \quad K \neq 0$$

$$SB(J) = 0, \quad J = K+16, 2M+15; \quad K \neq 2M-1$$

A.4 ACKNOWLEDGMENTS

Funding from the Office of Naval Research (Contract No. N00014-79-C-0472) for the development of the Sea Beam acoustic data acquisition system and for subsequent post-processing of the recorded data is gratefully acknowledged. R. C. Tyce initiated the Sea Beam acoustic backscattering experiment at MPL and F. V. Pavlicek greatly contributed to the development of the data acquisition system. This report was edited by E. Ford and J. Griffith did the art work.

A.5 REFERENCES

C. de Moustier and M.C. Kleinrock, Bathymetric artifacts in Sea Beam data: How to recognize them, what causes them, *JGR,* (in press) .

H. K. Farr, Multibeam bathymetric sonar: Sea Beam and Hydrochart, *Marine Geodesy, 4,* 77-93, 1980.

V. Renard and J. P. Allenou, SEA BEAM multi-beam echo-sounding in "Jean Charcot". Description, evaluation and first results, *International Hydrographic Review, LVI(1),* 35-67, Monaco, 1979.

ONR/MPL GENERAL DISTRIBUTION LIST

Chief of Naval Research
Department of the Navy
Arlington, Virginia 22217
Code 12, 122(2), 102C
111, 112, 113,
1122PO, 425-AC, 460

ONRDET
NSTL Station
Bay St. Louis, Mississippi 39529
Code 112, 1121, 1122CS, 422CB,
1122PO, 1125GG

Director
Office of Naval Research
Branch Office
1030 East Green Street
Pasadena, California 91101

Commander
Naval Sea Systems Command
Washington, D. C. 20362
Code 63, 63R, 63R-23

Defense Advanced Res. Proj. Agency
TTO - Tactical Technology Office
1400 Wilson Boulevard
Arlington, Virginia 22209
Atten: CDR Kirk Evans

Commander
Naval Air Systems Command
Washington, D. C. 20361
Code 370

Commander
Naval Ship Res. & Dev. Center
Bethesda, Maryland 20084

Director
Strategic Systems Proj. Ofc. (PM-1)
Department of the Navy
Washington, D. C. 20361
Code NSP-2023

Commander
Naval Surface Combat Systems Center
White Oak
Silver Spring, Maryland 20910

Commanding Officer
Civil Engineering Laboratory
Naval Construction Battalion Center
Port Hueneme, California 93043
Code L40, L42

Director of Research
U.S. Naval Research Laboratory
Washington, D. C. 20375
Code 2620, 2627, 5000, 5100, 5800

Commanding Officer
Naval Ocean Research and
Development Activity (NORDA)
NSTL Station
Bay. St. Louis, Mississippi 39529
Code 100, 110, 300, 330,
340, 350, 360, 500

Commander
U.S. Naval Oceanographic Office
NSTL Station
Bay St. Louis, Mississippi 39522
Bill Jobst

Commander
Submarine Development Group ONE
Fleet Post Office
San Diego, California 92152

Commander
Naval Wafare Systems Command
Washington, D. C. 20360
Code PME-124, 320A

Commanding Officer
U.S. Naval Air Development Center
Attention: Jim Howard
Warminister, Pennsylvania 18974

Executive Secretary, Naval Studies
Board
National Academy of Sciences
2101 Constitution Avenue, N.W.
Washington, D.C. 20418

Commander
Naval Ocean Systems Center
San Diego, California 92152
Code 00, 01, 16, 94, 531
5301, 71, 72

Commanding Officer
Naval Underwater Systems Center
Newport, Rhode Island 20844
John D'Albora

Officer in Charge
Naval Underwater Systems Center
New London Laboratory
New London, Connecticut 06320
Code 900, 905, 910, 930, 960

Assistant Secretary of the Navy
(Research Engineering & Systems)
Department of the Navy
Washington, D. C. 20350

Commanding Officer
Naval Coastal Systems Laboratory
Panama City, Florida 32401

Director
Defense Documentation Center
(TIMA), Cameron Station
5010 Duke Street
Alexandria, Virginia 22314

Institute for Defense Analyses
400 Army-Navy Drive
Arlington, Virginia 22202

Chief Scientist
Navy Underwater Sound Reference Div.
U.S. Naval Research Laboratory
P.O. Box 8337
Orlando, Florida 32806

Supreme Allied Commander
U.S. Atlantic Fleet
ASW Research Center, APO
New York, New York 09019
Via: ONR 100 M, CNO OP092D1,
Secretariat of Military,
Information Control, Committee

Director
College of Engineering
Department of Ocean Engineering
Florida Atlantic University
Boca Raton, Florida 33431

Director
Applied Research Laboratory
Pennsylvania State University
P.O. Box 30
State College, Pennsylvania 16802

Director
Lamont-Doherty Geological Observatory
Torrey Cliff
Palisades, New York 10964

Director
The Univ. of Texas at Austin
Applied Research Laboratory
P.O. Box 8029
Austin, Texas 78712

Director
Woods Hole Oceanographic Institution
Woods Hole, Massachusetts 02543

National Science Foundation
Washington, D. C. 20550

STOIAC
Battelle Columbus Laboratories
505 King Avenue
Columbus, Ohio 43201

National Oceanic & Atmospheric
Administration
Ocean Engineering Office
6001 Executive Boulevard
Rockville, Maryland 20852

Superintendent
U.S. Naval Postgraduate School
Monterey, California 93940

Director
Institute of Marine Science
University of Alaska
Fairbanks, Alaska 99701

Director
Applied Physics Laboratory
Johns Hopkins University
Johns Hopkins Road
Laurel, Maryland 20810
Atten: J. R. Austin

Director
Marine Research Laboratories
c/o Marine Studies Center
University of Wisconsin
Madison, Wisconsin 53706

Director
Applied Physics Laboratory
University of Washington
1013 East 40th Street
Seattle, Washington 98105

Director
Inst. of Ocean Science Engineering
Catholic University of America
Washington, D.C. 20017

Office of Naval Research
Resident Representative
c/o Univ. of California, San Diego
La Jolla, California 92093

University of California, San Diego
Marine Physical Laboratory Branch Office
La Jolla, California 92093

December 1985